



저작자표시-비영리-변경금지 2.0 대한민국

이용자는 아래의 조건을 따르는 경우에 한하여 자유롭게

- 이 저작물을 복제, 배포, 전송, 전시, 공연 및 방송할 수 있습니다.

다음과 같은 조건을 따라야 합니다:



저작자표시. 귀하는 원 저작자를 표시하여야 합니다.



비영리. 귀하는 이 저작물을 영리 목적으로 이용할 수 없습니다.



변경금지. 귀하는 이 저작물을 개작, 변형 또는 가공할 수 없습니다.

- 귀하는, 이 저작물의 재이용이나 배포의 경우, 이 저작물에 적용된 이용허락조건을 명확하게 나타내어야 합니다.
- 저작권자로부터 별도의 허가를 받으면 이러한 조건들은 적용되지 않습니다.

저작권법에 따른 이용자의 권리와 책임은 위의 내용에 의하여 영향을 받지 않습니다.

이것은 [이용허락규약\(Legal Code\)](#)을 이해하기 쉽게 요약한 것입니다.

[Disclaimer](#)



공학박사학위논문

**Synthesis, Properties and Applications of
Indolo[3,2-b]indole-Based Organic Semiconductors**

인돌로[3,2-b]인돌을 기반으로 한 유기반도체의 합성, 특성 및
응용에 대한 연구

2016년 8월

서울대학교 대학원

재료공학부

조 일 훈

**Synthesis, Properties and Applications of
Indolo[3,2-b]indole-Based Organic Semiconductors**

A THESIS SUBMITTED IN PARTIAL FULFILLMENT OF
THE REQUIREMENTS FOR THE DEGREE OF
DOCTOR OF PHILOSOPHY
IN ENGINEERING AT THE GRADUATE SCHOOL OF
SEOUL NATIONAL UNIVERSITY

AUGUST 2016

By
Illhun Cho

Supervisor
Prof. Soo Young Park

**Synthesis, Properties and Applications of
Indolo[3,2-b]indole-Based Organic Semiconductors**

인돌로[3,2-b]인돌을 기반으로 한 유기반도체의 합성, 특성 및¹
응용에 대한 연구

지도 교수 박 수 영
이 논문을 공학박사 학위논문으로 제출함

2016년 6월

서울대학교 대학원
재료공학부
조일훈
조일훈의 공학박사 학위논문을 인준함

2016년 6월

위 원장 _____ (인)

부위원장 _____ (인)

위 원 _____ (인)

위 원 _____ (인)

위 원 _____ (인)

Abstract

Synthesis, Properties and Applications of Indolo[3,2-b]indole-Based Organic Semiconductors

Illhun Cho

Department of Materials Science and Engineering
The Graduate School
Seoul National University

Organic semiconductors have been attracting significant attention as a potential alternative to the prevalent silicon-based semiconductor by the virtue of chemical versatility, good mechanical property, large area and low cost fabrication, flexibility, and so on. Aiming at the realistic device performance, a wide range of π -conjugated molecules have been developed and investigated. In particular, heteroatom-containing fused aromatic molecules (heteroacenes) have been explored as a structurally and an electronically fascinating molecular platform based on their unique electronic characteristics originating from the incorporated heteroatoms, rigid and extended π -conjugation, excellent oxidative stability, and tight molecular stacking. Among various types of heteroacenes, pyrrole-containing ones have been intensively investigated owing to their low redox potential, strong electron donating nature and feasibility for molecular structure modification. However, pyrrole-fused heteroacenes which ensure

the superb device performance is still rather limited for few molecular structures. Among various types of pyrrole-fused heteroacenes, I have focused particular attention on indolo[3,2-b]indole (IDID) unit which comprises two inner pyrrole rings and two outer benzene rings fused all together, as a promising π -conjugated backbone structure for high performance organic semiconductor. IDID allows symmetrical structural derivatization in (*N,N*)-, (2,7)-, and (3,8-) positions affording diverse opportunities to control their π -conjugation length and solubility with high flexibility, and their fused two pyrrole rings give rise to strong electron donating nature. Despite such promising perspective of IDID core, its organic semiconductor applications have seldom been explored so far. In this regard, this dissertation describes following two main topics; i) rational molecular design of IDID-based π -conjugated molecule to realize high performance organic semiconductor, ii) chemical structure modification of IDID core unit for the development of advanced and versatile core structure.

Firstly, in order to verify the high potential of the IDID core as an organic semiconductor backbone structure, and also to propose molecular design strategy for the high-performance and versatile processable IDID-based semiconductor, a series of IDID derivatives comprising the core unit of *N,N*-dihexyl-IDID with different aromatic and aliphatic substituents at 2- and 7-position were designed and synthesized. Among others, 4H4TIDID (with 2- and 7-substituents of 5-hexyl-2,2'-bithiophene moiety) with excellent solubility (> 20 weight% in chloroform), showed the highest field-effect hole mobility of $0.97 \text{ cm}^2 \text{ V}^{-1} \text{ s}^{-1}$ in vacuum deposited (VD) organic field-effect

transistor (OFET) device and $0.18 \text{ cm}^2 \text{ V}^{-1} \text{ s}^{-1}$ in spin-coated OFET device, respectively, and also both devices identically showed the two-dimensional (2D) molecular orientation favorable for the high transistor mobility.

Besides apparent advantages of pyrrole-fused structure such as facile solubility control and structural derivatization, IDID core is characterized by stronger electron donating nature than those of others. In this regard, to examine the possible bipolar carrier injection and transport, intramolecular charge transfer (ICT)-type IDID derivatives, which comprise IDID as an electron donor (D) and dicyanovinyl (DCV) as an electron acceptor (A) with A- π -D- π -A type architecture were designed and synthesized. It was found that the compensated ICT interaction between IDID and DCV of 2TIDID-DCV derivatives (with thiophene π -spacer) and their efficient electronic interaction in the three-dimensional lamellar π -stacking structure gave rise to the dramatically reduced energy band-gap as well as excellent film morphology. Consequently, I could successfully demonstrate that 2H2TIDID-DCV exhibited highly balanced ambipolar charge transport with hole and electron mobilities of $0.08 \text{ cm}^2 \text{ V}^{-1} \text{ s}^{-1}$ and $0.09 \text{ cm}^2 \text{ V}^{-1} \text{ s}^{-1}$, respectively, in VD OFET devices. The spin-coated OFET devices using OD2TIDID-DCV, for which hexyl side chains of 2H2TIDID-DCV were replaced by 2-octyldodecyl, also exhibited ambipolar charge transporting nature (mobility of $9.67 \times 10^{-2} \text{ cm}^2 \text{ V}^{-1} \text{ s}^{-1}$ for hole, and $3.43 \times 10^{-3} \text{ cm}^2 \text{ V}^{-1} \text{ s}^{-1}$ for electron).

Meanwhile, in the course of my investigation, I observed typical molecular

interaction tendency of pyrrole-fused heteroacenes from the IDID derivatives, i.e., slipped-herringbone packing structure and distorted π -plane which are regarded as demerit for the ensuring high mobility. Not only to solve these kinds of drawbacks, but also to provide effective strategy for the crystal engineering, I tried to tune the molecular interaction motif of indolo[3,2-b]indole (IDID) derivatives through incorporating the fluorine (F) atom into the IDID core. It was found that the substitution of F atom at 3- and 8-position of IDID core gave rise to extended and planar π -conjugated backbone structure, strong Coulombic force toward π - π stacking, and dense one-dimensional crystal growing for their derivatives. As a consequence, 4H4TIDIDF for which IDID core of 4H4TIDID was replaced by fluorinated IDID, exhibited excellent p-type field-effect mobility of $1.88 \text{ cm}^2 \text{ V}^{-1} \text{ s}^{-1}$ in single crystal (SC) OFET device with packing motif of slipped π -stack.

In addition, I could successfully demonstrate that 4H4TIDIDF exhibited as a high-performance crystalline hole transporting material (HTM) for perovskite solar cells (PSCs). A planar π -conjugated backbone linked with a flexible alkyl chain of 4H4TIDIDF enabled a tight molecular stacked arrangement as well as versatile processing, leading to a higher hole mobility than that of p,p-Spiro-OMeTAD in sandwich-type devices. The photoluminescence quenching in perovskite/4H4TIDIDF interface was also more effective as compared to that at the perovskite/p,p-Spiro-OMeTAD. As a consequence, the PSC device fabricated using 4H4TIDIDF showed a superior performance as compared to p,p-Spiro-OMeTAD, exhibiting a best PCE of

19%. Thus, this remarkable result demonstrated fluorinated IDID core-based materials as a new class of HTM for highly efficient PSCs.

Lastly, to elaborate characteristics of fluorinated IDID core as a donor building block for ICT-type molecules, ICT-type low bandgap small molecules were designed and synthesized by altering electron donors (IDID and fluorinated IDID) and electron acceptors (octylcyanoacetate (OCA) and 3-ethylrhodanine (Rho)), for the solution processed bulk-heterojunction organic solar cells (BHJ-OSCs). It was found that the fluorinated IDID derivatives exhibited lower highest occupied molecular orbital (HOMO) energies than those of non-fluorinated counter molecules (ca. 0.1 eV, each), resulting in the higher open circuit voltage (V_{oc} , by ~ 0.1 eV) for the BHJ-OSC devices. Moreover, strong π - π interaction of fluorinated IDID derivatives gave rise to stable micro-structure with edge-on lamellar packing in their blended films (with [6,6]-phenyl-C₆₁-butyric acid methyl ester (PC₆₁BM)) as well as in their neat films. Consequently, the BHJ-OSC devices using fluorinated IDID derivatives with 3-ethylrhodanine and octylcyanoacetate exhibited enhanced device performance than those of non-fluorinated IDID-based devices with a best PCE of 3.90% for OD4TIDIDF-Rho, and 3.07% for HD4TIDIDF-OCA.

Keyword: indolo[3,2-b]indole, heteroacene, charge transport, hole-transporting, ambipolar, organic electronics, organic semiconductor, organic field-effect transistor, organic solar cell, perovskite solar cell.

Student Number: 2008-20687

Contents

Abstract	i
Contents	vii
List of Tables	xii
List of Schemes	xiii
List of Figures	xiv
Chapter 1. Introduction.....	1
1.1. Organic Electronics	1
1.2. Organic Semiconductors	2
1.2.1. Organic Field-Effect Transistor	3
1.2.2. Organic Solar Cell (Organic Photovoltaics).....	9
1.3. Factors Influencing Charge Carrier Transport.....	14
1.3.1. Theoretical Aspect	15
1.3.2. Molecular Packing	19
1.4. Small Molecule Organic Semiconductors.....	22
1.4.1. Acene and Their Derivatives	22
1.4.2. Heteroatom-Containing Fused Aromatics	25
1.5. Research Objective and Contents of Thesis	29

1.6. References	31
-----------------------	----

Chapter 2. Design, Synthesis, and Versatile Processing of Indolo[3,2-b]indole-based π -Conjugated Molecules for High-Performance Organic Field-Effect Transistor.....39

2.1. Introduction	39
2.2. Experimental	42
2.3. Results and Discussion	53
2.3.1 Design and Synthesis	53
2.3.2. Theoretical, Optical, and Electrochemical Properties	55
2.3.3. VD OFET Characteristics	61
2.3.4. Structural Analyses	65
2.3.5. Solution-Processed OFET Characteristics.....	72
2.4. Conclusion	75
2.5. Reference	76

Chapter 3. Dicyanovinyl-Substituted Indolo[3,2-b]indole Derivatives: Low Band-Gap π -Conjugated Molecules for Single-Component Ambipolar Organic Field-Effect Transistor80

3.1. Introduction	80
3.2. Experimental	83

3.3. Results and Discussion	99
3.3.1 Design and Synthesis	99
3.3.2. Theoretical, Optical, and Electrochemical Properties	100
3.3.3. OFET Characteristics	107
3.3.4. Structural Analyses	115
3.4. Conclusion	118
3.5. Reference	119

**Chapter 4. Crystal Engineering of Indolo[3,2-b]indole Derivatives for
High Performance Single-Crystal Organic Field-Effect
Transistor: Exploring Fluorination Effect on Structural and
Electrical Characteristics**122

4.1. Introduction	122
4.2. Experimental	125
4.3. Results and Discussion	136
4.3.1. Design and Synthesis	136
4.3.2. Single Crystal Packing and Analysis	137
4.3.3. Charge Distribution and Impact on Crystal packing.....	141
4.3.4. Single Crystal Device.....	144
4.4. Conclusion	153

4.5. Reference	154
----------------------	-----

Chapter 5. Fluorinated Indolo[3,2-b]indole-Based Crystalline Hole Transporting Material for Highly Efficient Perovskite Solar Cells.....157

5.1. Introduction	157
5.2. Experimental	161
5.3. Results and Discussion	165
5.3.1. Optical and Electrochemical Properties	165
5.3.2. Charge Transport Property	168
5.3.3. Perovskite Solar Cell Device Characteristics	171
5.4. Conclusion	175
5.5. Reference	176

Chapter 6. Fluorinated Indolo[3,2-b]indole-Based Low Band-gap Small Molecules for High-Performance Organic Solar Cells.....180

6.1. Introduction	180
6.2. Experimental	183
6.3. Results and Discussion	193
6.3.1. Design and Synthesis	193
6.3.2. Optical, Electrochemical, and Thermal Properties	194

6.3.3. BHJ-OSC Characteristics	201
6.3.4. Film Structure.....	205
6.4. Conclusion	208
6.5. Reference	209
Abstract in Korean	213
List of Publications	220
List of Presentations	223
List of Patents	227

List of Tables

Table 2-1. Optical and electrochemical properties of IDID derivatives	60
Table 2-2. Field-effect transistor characteristics of IDID derivatives.....	64
Table 2-3. Crystal data and structure refinement for 2H2TIDID.	70
Table 2-4. Summary of correlation result between 2D-GIXD and DFT calculation....	71
Table 3-1. Optical and electrochemical properties of IDID-DCV derivatives.....	106
Table 3-2. OFET device characteristics.....	114
Table 4-1. Crystal data and structure refinement for 2H2TIDIDF.	140
Table 4-2. Crystal data and structure refinement for 4H4TIDIDF.	148
Table 6-1. Optical, electrochemical and thermal properties of IDID derivatives.....	200
Table 6-2. Optimized BHJOSC device performance of IDID derivatives	204

List of Schemes

Scheme 2-1. Synthetic route for IDID derivatives and their chemical structures.	50
Scheme 3-1. a) Synthesis route for IDID-DCV derivatives and their chemical structure;	
b) Chemical structure of IDID reference derivatives.	89
Scheme 3-2. a) Synthesis route for 5,10-dihexyl-5,10-dihydroindolo[3,2-b]indole (2HIDID), and b) OD2TIDID-DCV.....	96
Scheme 4-1. a) Molecular structures of target materials; b) Synthetic routes for 2H2TIDIDF and 4H4TIDIDF	135
Scheme 6-1. Synthetic route for IDID derivatives and their chemical structures.	192

List of Figures

Figure 1-1. Types of OFETs. (a) Bottom-gate top-contact, (b) bottom-gate bottom-contact, (c) top-gate bottom-contact, (d) top-gate top-contact.....	7
Figure 1-2. Illustration of operating regimes of field-effect transistor and their current-voltage characteristics. (a) linear regime, (b) start of saturation regime at pinch-off, (d) saturation regime. ^[20]	8
Figure 1-3. Representative current-voltage characteristics of field-effect transistor. (a) Output characteristics, (b) and (c) transfer characteristics in the liner and saturation regime, respectively. ^[20]	8
Figure 1-4. Schematic illustration of bulk-heterojunction solar cell. ^[37]	12
Figure 1-5. General mechanism for power conversion process from incident light to electricity. ^[37]	13
Figure 1-6. Current-voltage curves of an organic solar cell (dashed line: dark, solid line: illuminated). ^[33]	13
Figure 1-7. Evolution of transfer integrals for tetracene dimer (as a function of (a) along the long axis, (b) along the short axis, and (c) intermolecular distance), and (d) schematic diagram of reorganization energy of neutral state (1, $\lambda_{rel}^{(1)}$) and charged state (2, $\lambda_{rel}^{(2)}$). ^[27]	18
Figure 1-8. Schematic image of four kinds of packing motifs and the preferential charge transport pathways. (a) Herringbone packing, (b) slipped	

herringbone packing, (c) 1-dimentional π -stacking, and (d) 2-dimensional π -stacking.....	21
Figure 1-9. Chemical structure of PAHs and their derivatives.....	24
Figure 1-10. (a and b) Packing structure of 2,9-C ₁₀ -DNTT elucidated by single crystal crystallography, and (c) definitions of intermolecular interaction motif and interaction of BTBT-based derivatives. ^[75]	28
Figure 2-1. Optical and theoretical characteristics of IDID derivatives. (a) solution absorption spectra; (b) film absorption spectra; (c) calculated frontier molecular orbitals.....	58
Figure 2-2. Cyclic voltammograms (CVs) of IDID derivatives. (a) solution samples were prepared 5 X 10 ⁻³ M solution in methylene chloride; (b) film samples were prepared on ITO patterned glass by drop-casting method (Inset: CV of ferrocene).	59
Figure 2-3. Transfer curves and output curves of VD OFETs base on IDID derivatives, respectively. (a), (e) for 2H2TIDID; (b), (f) for 4H2TIDID; (c), (g) for 2H4TIDID; (d), (h) for 4H4TIDID.....	63
Figure 2-4. Mobility evolution diagram for 4H4TIDID OFET device in ambient condition (temperature of 15 °C and relative humidity of 28%).	63
Figure 2-5. Single crystal structure of 2H2TIDID.....	67
Figure 2-6. 2D-GIXD patterns of vacuum deposited samples ((a) 2H2TIDID; (b) 2H4TIDID; (c) 4H2TIDID; (d) 4H4TIDID), and schematic diagram of	

4H4TIDID supramolecular structure ((e), The in-plane molecular orientation in this figure is an illustration of hypothetically constructed slipped herringbone stacking based on the SC-XRD result of 2H2TIDID).

..... 68

Figure 2-7. 2D-GIXD diffraction images of IDID derivatives VD films and corresponds q_z line-cut profiles. (a) 2H2TIDID; (b) 2H4TIDID; (c) 4H2TIDID; (d) 4H4TIDID..... 69

Figure 2-8. Transfer curve (a) and output curve (b) of 4H4TIDID spin-coated OFET device, and 2D-GIXD patterns of 4H4TIDID vacuum deposited film (c) and spin-casted film (d)..... 74

Figure 2-9. Atomic force microscope height images of 4H4TIDID on OFET devices. (a) T_{sub} 50°C VD device; (b): T_{sub} 90°C VD device; (c) Spin-coated device.

..... 74

Figure 3-1. Plot of calculated energy levels for IDID-DCV derivatives and IDID reference derivatives, and their molecular orbital contour (DFT/B3LYP-6-31G d p, the alkyl chains were replaced by methyl in calculation). 104

Figure 3-2. Absorption spectra of IDID-DCV derivatives for solution state (a) and film state (b), and each solution state absorption spectra with correspondent reference (c)..... 105

Figure 3-3. Cyclic voltammograms of IDID-DCV derivatives in solution state (a) and film state (b). 105

Figure 3-4. AFM surface topologies (height images, 5 $\mu\text{m} \times 5 \mu\text{m}$) of 2H2TIDID-DCV (a and b) and 2H4TIDID-DCV (c and d) VD thin films under different T_{sub} ((a and c) RT; (b and d) 70 °C). 110

Figure 3-5. OFET devices characteristics. (a to f) Representative OFET device characteristics of 2H2TIDID-DCV ((a and c) transfer curves of T_{sub} 120 °C device, (b and d) output curves T_{sub} 120 °C device, and (e and f) temperature dependent mobility for p- and n-channel operation, respectively. (white stars represent average value)); (g and j) Spin-coated OFET device characteristics of OD2TIDID-DCV (annealing temperature is 150 °C, (g and i) transfer curves and (h and j) output curves for p- and n-channel operation, respectively). 111

Figure 3-6. The transfer curves of 2H2TIDID-DCV OFET devices for p- and n-channel operation with different T_{sub} , respectively ((a and b) T_{sub} RT, (c and d) T_{sub} 50°C, (e and f) T_{sub} 70°C, (g and h) T_{sub} 100°C, (i and j) T_{sub} 120°C, (k and l) T_{sub} 140°C). 112

Figure 3-7. AFM surface topologies (height images, 5 $\mu\text{m} \times 5 \mu\text{m}$) of 2H2TIDID-DCV VD thin films under different T_{sub} ((a) RT; (b) 50 °C; (c) 70 °C; (d) 100°C; (e) 120 °C; (f) 140 °C), and OD2TIDID-DCV spin-coated film ((i)), annealed at 150 °C 113

Figure 3-8. (a) Out-of-plane XRD pattern of 2H2TIDID-DCV VD films under

different T_{sub} ; (b) Powder XRD pattern of 2H2TIDID-DCV powder; (c) 2D-GIXD diffraction pattern image of 2H2TIDID-DCV VD films ($T_{\text{sub}} = 140^{\circ}\text{C}$); (d and e) Horizontal and vertical line profile of (c), respectively; (f) 2D-GIXD diffraction pattern image of OD2TIDID-DCV film; (g and h) Horizontal and vertical line profile of (e), respectively; (i) Calculated molecular size of 2H2TIDID-DCV; (j) Schematic diagram of 2H2TIDID-DCV packing structure.....	117
Figure 4-1. Crystal structures of 2H2TIDIDF (a to c) and 2H2TIDID (d to f). (For the clear identification, hydrogen atoms of the molecules are expelled in images on b, c, d, e, and f).....	139
Figure 4-2. Electrostatic potential maps; (a) 2H2TIDID, (b) 2H2TIDIDF $_{\alpha}$ -conformer, (c) 2H2TIDIDF $_{\beta}$ -conformer, (d) 2H2TIDIDF-dimer $_{\alpha}$ -conformer, (e) 2H2TIDIDF-dimer $_{\beta}$ -conformer.....	143
Figure 4-3. Single Crystal Structure and electrostatic potential map of 4H4TIDIDF.	147
Figure 4-4. Optical microscope (OM) image of 4H4TIDIDF dip-coating device (a), and atomic force microscope (AFM) height image of 4H4TIDIDF micro-crystals (b).....	151
Figure 4-5. (a) Molecular packing structure of 4H4TIDIDF for SC device, (b) out-of-plane XRD of 4H4TIDIDF SC device (up) and simulated powder XRD from single crystal analysis data of 4H4TIDID (b)	152

Figure 5-1. (a) Molecular structure of 4H4TIDIDF. (b) UV-vis absorption spectra of 4H4TIDIDF in solution (tetrahydrofuran, 1×10^{-5} M) and film state.....	160
Figure 5-2. Out-of-plane XRD of 4H4TIDIDF and p,p-Spiro-OMeTAD.....	167
Figure 5-3. Cyclic voltammograms (CVs) of 4H4TIDIDF and p,p-Spiro-OMeTAD. Film samples were prepared on ITO patterned glass by drop-casting method (Inset: CV of ferrocene).....	167
Figure 5-4. Photoelectron spectrum of the mixed perovskite film on a fused silica substrate	167
Figure 5-5. (a) The space-charge-limited-current (SCLC) of hole-only devices with the configuration of indium tin oxide (ITO)/poly(3,4-ethylenedioxythiophene)-polystyrene sulfonate (PEDOT:PSS)/p,p-Spiro-OMeTAD or 4H4TIDIDF/ Au. (b) PL emission spectra of perovskite/PMMA, perovskite/p,p-Spiro-OMeTAD, and perovskite/4H4TIDIDF film under excitation at 670 nm.....	170
Figure 5-6. (a) Cross-sectional scanning electron microscopy (SEM) image of the device including FTO/ bl-TiO ₂ /mp-TiO ₂ / perovskite/4H4TIDIDF/Au. (b) The schematic energy diagram of the corresponding device.....	173
Figure 5-7. (a, b) Current density-voltage (<i>J-V</i>) curves of the best device (FTO/ bl-TiO ₂ /mp-TiO ₂ / perovskite/IDIDF/Au, a) is average curve), (c) The steady-state photocurrent and efficiency of the corresponding device at the maximum power point (0.88 V). (d) The corresponding external quantum	

efficiency (EQE) spectra. (e) The comparison of <i>J-V</i> curves of the devices fabricated using IDIDF and commercial pp-Spiro. Li-bis(trifluoromethanesulfonyl)imide (Li-TFSI) and 4- <i>tert</i> -butylpyridine (<i>t</i> BP) as additives are used in this work.	174
Figure 6-1. (a) UV-vis absorption spectra of IDID derivatives in solution. (b) Normalized absorption spectra of IDID derivatives in solution and film state.....	197
Figure 6-2. Cyclic voltammograms of IDID derivatives in film state: (a) OCA derivatives, and (b) Rho derivatives.....	198
Figure 6-3. Differential scanning calorimetry thermograms of IDID derivatives: (a) HD4TIDID-OCA, (b) HD4TIDIDF-OCA, (c) HD4TIDID-Rho, and (d) HD4TIDIDF-Rho	199
Figure 6-4. Differential scanning calorimetry thermograms of IDID derivatives: (a) HD4TIDID-OCA, (b) HD4TIDIDF-OCA, (c) HD4TIDID-Rho, and (d) HD4TIDIDF-.....	203
Figure 6-5. IPCE spectra of IDID derivatives:PC ₆₁ BM BHJ devices.....	203
Figure 6-6. 2D-GIXD patterns of IDID-derivatives neat films and IDID-derivatives/PCBM blend films; (a) HD4TIDID-OCA neat, (b) HD4TIDID-OCA/PCBM blend, (c) HD4TIDIDF-OCA neat, (d) HD4TIDIDF-OCA/PCBM blend, (e) HD4TIDID-Rho neat, (f) HD4TIDID-Rho/PCBM blend, (g) OD4TIDIDF-Rho neat, (h) OD4TIDIDF-OCA/PCBM blend.	207

Chapter 1. Introduction

1.1. Organic Electronics

Since the pioneering discovery of conducting polyacetylene by Sirakawa, MacDiarmid, and Heeger in 1977,^[1] π -conjugated molecules have drawn significant interest as an alternative of prevalent silicone-based semiconductor owing to their potential applications to various next-generation light weight, large-area, and flexible electronic devices including organic light emitting diodes (OLEDs),^[2,3] organic field-effect transistors (OFETs),^[4-6] organic photovoltaics (OPVs),^[7,8] and radio frequency identification (RFID).^[9,10]

The most intriguing advantage of organic semiconductors compared to inorganic counterpart lies in their chemical versatility and feasibility in controlling intrinsic characteristics, such as photophysical, thermal, mechanical, electronic and electrical properties. In this sense, π -conjugated materials have been considered as a fascinating research field providing a chance to overcome limitation of inorganic semiconductors and giving a chance to create various new concepts.^[11,12] Therefore, during the last two decades intensive research efforts have been paid in both academia and industry, and thus, magnificent advances have been made both in the electrical performance and theoretical fundamentals.^[12-14] In case of OLEDs consisting of organic

electroluminescent layer and multiple charge transporting layers, big industrial market has already been established, and other applications are also rapidly catching up their inorganic counterpart in terms of device performances. For instance, field-effect hole and electron mobility of organic semiconductors have overcome those of amorphous silicon (i.e., over $\sim 40 \text{ cm}^2 \text{ V}^{-1} \text{ s}^{-1}$ for p-type and over $\sim 10 \text{ cm}^2 \text{ V}^{-1} \text{ s}^{-1}$ for n-type)^[15,16], and power conversion efficiency of OPVs are exceeding 10%,^[17,18] recently. It is no doubt that, these dramatic achievements of organic semiconductors have been attributed to a dedication not only for developing novel organic semiconductor materials, but also device optimization in view of device physics and practical fabrication method.^[19-22] However, in terms of fundamental research side, there still remains interesting but ambiguous phenomena that has not been fully understood yet, and wide variety of sensational concepts are being developed constantly.^[23-26] Furthermore, there are still rooms for improvement in the device performance as well as stability. Therefore, to realize practical organic electronics, constant dedications are demanded in both development of novel materials and understanding of their unique phenomena.

1.2. Organic Semiconductors

In General, π -conjugated molecules and polymers for use in electronic devices are

called organic semiconductor. All of organic electronic devices which employ organic semiconductors as an active layer for the device operation have common interest and issues, i.e., charge carrier transport properties.^[27] Although, each types of devices are constructed with different architectures and are operated by different mechanism, their device performance are crucially dependent on charge carrier (hole and/or electron) mobility of active organic semiconductors; especially for OFETs and OPVs. Therefore, in developing novel organic semiconductor materials, appropriate evaluation of electrical characteristics is most important and essential. Charge carrier mobility can be extracted from various methods, for instance, time-of-flight (TOF),^(28,29) space-charge-limited current (SCLC),⁽³⁰⁾ and field-effect transistor (FET) measurement.⁽³¹⁾ Among others, FET technique, which is typically used for inorganic semiconductors, is most widely used because it can provide electrical characteristics in various parameter, such as field-effect mobility, current on-off ratio, and threshold voltages. Therefore, OFETs is considered as the most powerful device architecture for understanding electrical characteristics of π -conjugated system.

1.2.1. Organic Field-Effect Transistor

OFETs consist of following components; gate electrode, insulating gate dielectric, organic semiconductor, and electrodes (source and drain). According to the

configuration of components, OFETs can be categorized into four different types (see **Figure 1-1**): the top-gate bottom-contact (a), the top-gate top-contact (b), the bottom-gate bottom-contact (c), and bottom-gate top-contact (d). Normally, it is known that device configurations of which gate and contact are located at different side, e.g., (a) and (d) exhibit better performances than others owing to better condition of contact between the organic semiconductor and the electrodes.^[32]

In principle, in case of p-type OFETs, very small current flow is observed at the zero gate voltage (this state is called off-state). When a negative voltage is applied in gate electrode, opposite charges are accumulated at the interface between organic semiconductor and gate dielectric. Then, if the Fermi level of source (and drain) electrode is close to the HOMO level of the organic semiconductor, hole charge carriers are injected from the source electrode and transport takes place to the drain electrode (this state is called on-state). When source-drain voltage (V_{ds}) is smaller than actual gate voltage (gate voltage (V_g) – threshold voltage (V_{th})), the current flow between source and drain (I_{ds}) is proportionally increased with the increasing of V_{ds} , (this regime is called linear regime, **Figure 1-2 a**). When V_{ds} reaches the potential equal to $V_g - V_{th}$, the channel is pinched off (**Figure 1-2 b**). With further increase in V_{ds} , I_{ds} gradually becomes saturated (this regime is called saturation regime, **Figure 1-2 c**). Likewise, n-type OFETs are operated by applying the positive gate voltage, and injection of electron charge carriers through the LUMO level of the organic semiconductor.^[13]

The $I-V$ characteristics of OFET device in both regimes can be described by the gradual channel approximation. By the analytical assumption, the I_{ds} could be expressed as follows;

$$I_{ds}dx = W\mu C_i(V_g - V_{th} - V(x))dV$$

Where, W is the channel width, μ is the charge mobility, C_i is the capacitance per unit area of the gate dielectric, and x is the given position along the channel. By integration of the current increment from $x = 0$ to channel length (L) (from $V(x) = 0$ to V_{ds}), the gradual channel expression for the I_{ds} can be derived as,

$$I_{ds} = \frac{W}{L}\mu C_i \left[(V_g - V_{th})V_d - \frac{1}{2}V_{ds}^2 \right]$$

In the linear regime, this can be simplified to,

$$I_{ds,lin.} = \frac{W}{L}\mu_{lin.}C_i(V_g - V_{th})V_{ds}$$

Meanwhile, in the saturation regime, the current cannot increase and saturate, attributed to pinch-off. By substituting V_{ds} with $V_g - V_{th}$, the saturation current can be obtained. Therefore, I_{ds} for the saturation regime can be simplified to,

$$I_{ds,sat.} = \frac{W}{2L}\mu_{sat.}C_i(V_g - V_{th})^2$$

From these equations, the field-effect mobility in both regimes can be extracted. In linear regime, because the drain current is directly proportional to gate voltage, the field-effect mobility can be derived as,

$$\mu_{lin.} = \frac{\partial I_{ds}}{\partial V_g} \cdot \frac{L}{WC_i V_{ds}}$$

Meanwhile, in saturation regime, the square root of the saturation current is directly proportional to the gate voltage. Therefore, the field-effect mobility can be derived as,

$$\mu_{sat.}(V_g) = \frac{\partial I_{ds,sat.}}{\partial V_g} \cdot \frac{L}{WC_i} \cdot \frac{1}{V_g - V_{th}}$$

Figure 1-3 shows typical output (I_{ds} versus V_{ds} for different constant V_g) and transfer (I_{ds} versus V_g at constant V_{ds}) characteristics of OFET. From the output curve, the linear and the saturation regime can be determined at given V_g , and from the transfer curve, mobility which is proportional to gradient of square root of I_{ds} , and V_{th} which is extrapolated linear fit to zero, can be extracted as mentioned above. The on/off current ratio, threshold voltage, and subthreshold swing which is an exponential behavior of the current as a function of voltage below V_{th} also can be extracted from transfer characteristics; the off current state and the on current can be defined by lowest and saturated I_{ds} , respectively, the V_{th} can be determined exploration of linear region of the $\sqrt{I_d}$ vs. V_g plot, and subthreshold swing can be extracted by $S = dV_g/d(\log I_d)$.

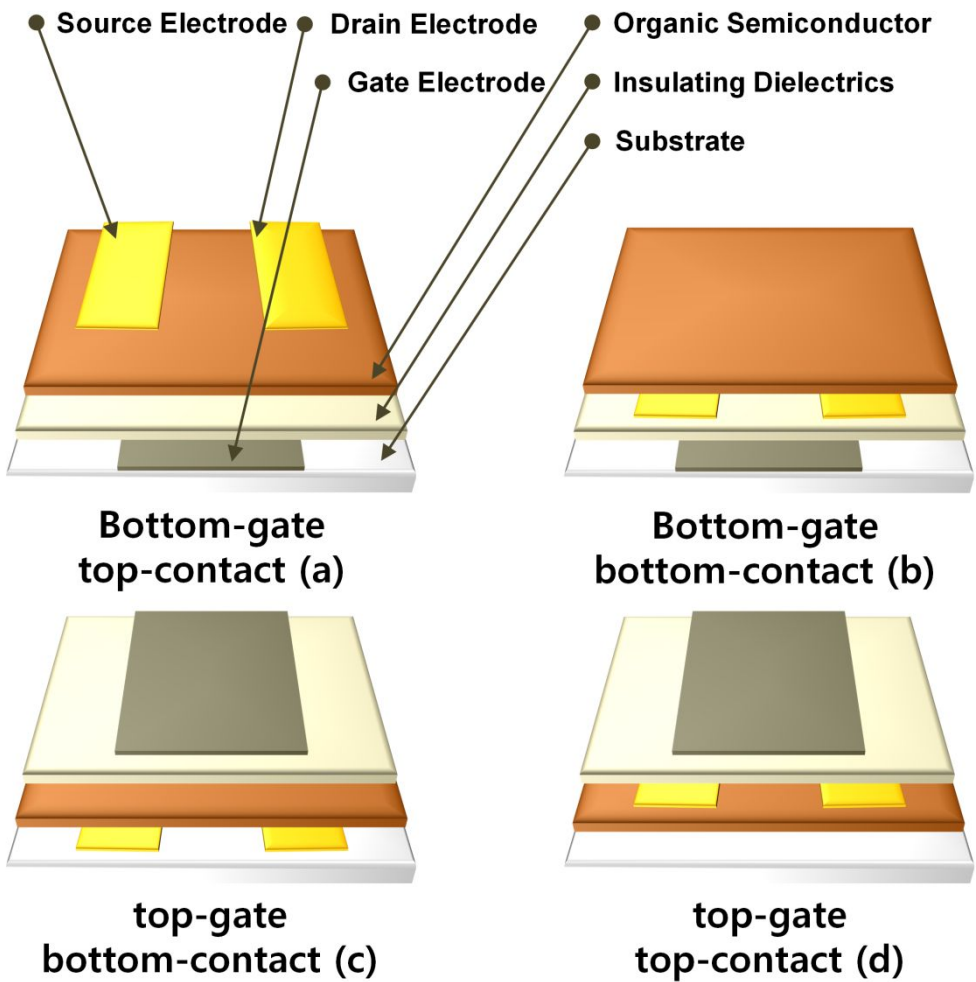


Figure 1-1. Types of OFETs. (a) Bottom-gate top-contact, (b) bottom-gate bottom-contact, (c) top-gate bottom-contact, (d) top-gate top-contact.

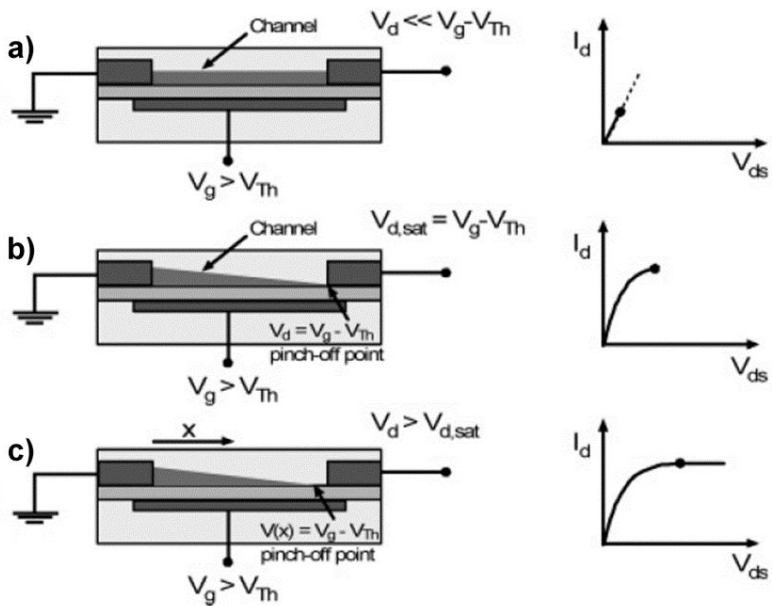


Figure 1-2. Illustration of operating regimes of field-effect transistor and their current-voltage characteristics. (a) linear regime, (b) start of saturation regime at pinch-off, (d) saturation regime.^[20]

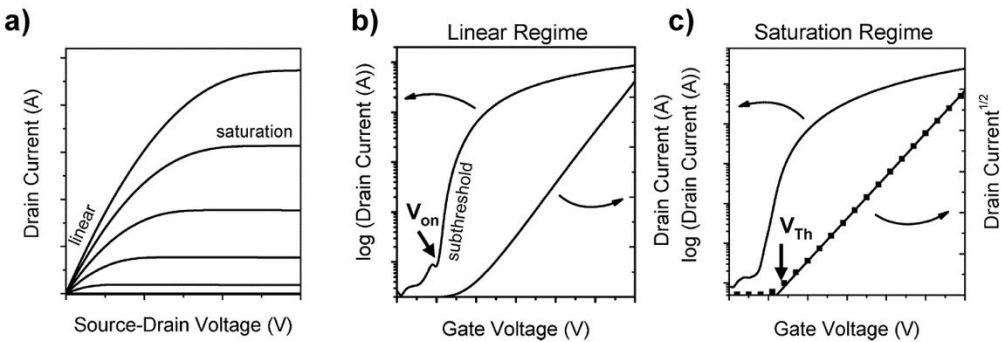


Figure 1-3. Representative current-voltage characteristics of field-effect transistor. (a) Output characteristics, (b) and (c) transfer characteristics in the liner and saturation regime, respectively.^[20]

1.2.2. Organic Solar Cell (Organic Photovoltaics)

Organic solar cell of which photoactive layers consist of π -conjugated organic semiconductor has been intensively investigated during last two decades,^[33,34] and among various types, solution-processed bulk heterojunction organic solar cells (BHJ-OSCs) comprising p-type (donor) and n-type (acceptor) semiconductors with mixed bicontinuous phase, have been drawing interest as a promising technology for the next generation of renewable energy-conversion.^[35,36] Typically, BHJ-OSCs consist of following components as multi-layered structure; indium tin oxide (ITO) on transparent substrate, poly(3,4-ethylenedioxythiophene)-polystyrene sulfonate (PEDOT-PSS) as a hole extraction and transporting layer, bulk heterojunction-type photoactive layer, and aluminum (Al) electrode (**Figure 1-4**).^[37] Power conversion from the incident light to electricity is proceeding through the following steps.^[37] First, light absorption is followed by the formation of bound electron-hole exciton pair. Subsequently, exciton migration and dissociation happen at donor-acceptor interface. When exciton pairs reach donor-acceptor interface following processes are occurring in sequence; i) exciton pairs are changed to encounter pairs, ii) electron transfer within the encounter pair gives rise to the geminate electron-hole pair, iii) charge separation is occurred by the built-in potential in the interface region between p-type and n-type semiconductors. Lastly, separated electron hole charges are transported to the each

electrode (**Figure 1-5**). The device performance of organic solar cells is represented by power conversion efficiency (PCE) which is determined by following formula;

$$\eta_e = \frac{V_{oc} * I_{sc} * FF}{P_{in}}$$

Where, V_{oc} is open circuit voltage, I_{sc} is short circuit current, FF is fill factor, P_{in} is incident light power density. The V_{oc} is the maximum voltage of the device and is determined by following equation;

$$V_{oc} = \left| E_{LUMO \text{ of electron acceptor}} + E_{HOMO \text{ of electron donor}} + \frac{K_B}{e\{\ln(n_e n_h |N_c^2)\}} \right|$$

Where, n_e and n_h are electron and hole density, respectively, and N_c is the corresponding density of state near the LUMO of electron acceptor and HOMO of electron donor. However, it should be note that charge transfer (CT) state between the donor and acceptor is also considered as one of the crucial components to determine the V_{oc} of the BHJ-OSCs.^[38-40] The I_{sc} is the current flow which there is no external field applied. The I_{sc} is determined by collected charge carriers followed by the photoinduced charge generation and charge carrier transport to both electrode, and is described as follow,^[33]

$$I_{sc} = ne\mu E$$

Where, n is the density of generated charge carrier, e is the elementary charge, μ is the mobility, and E is the electric field. Therefore, to comprehend I_{sc} for given device, molar extinction coefficient, recombination rate, and charge carrier mobility of

photoactive material at given film state should be considered. The FF is the ratio between multiplies current maximum power point (I_{mmp}) by voltage maximum power point (V_{mmp}) and multiplies J_{sc} by V_{oc} as below,

$$FF = \frac{I_{mmp} * V_{mmp}}{I_{sc} * V_{oc}}$$

This means that FF is determined by the competition between sweep-out of the photogenerated charge carriers and their recombination to the ground state before charge carrier extraction to each electrode (see **Figure 1-6**).

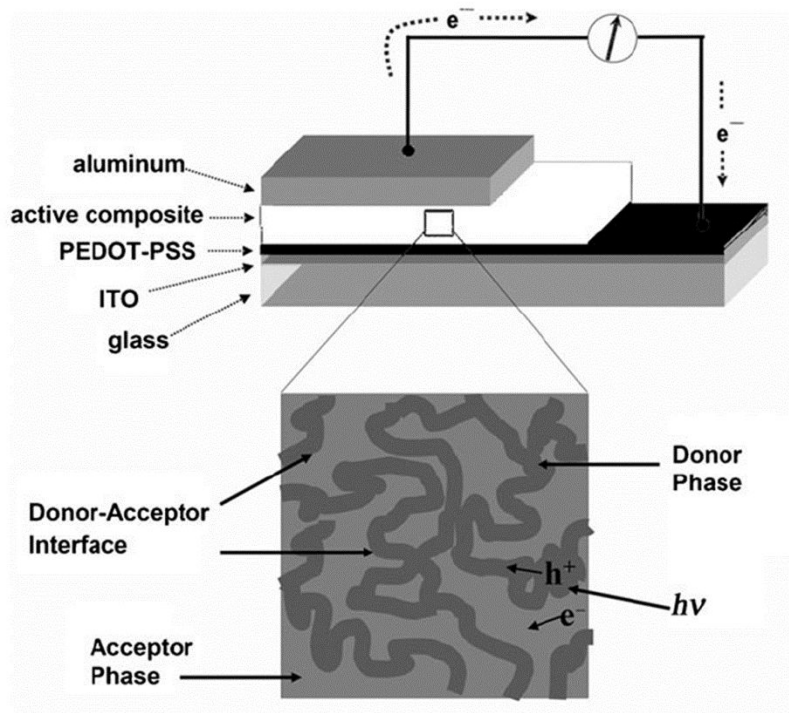


Figure 1-4. Schematic illustration of bulk-heterojunction solar cell. ^[37]

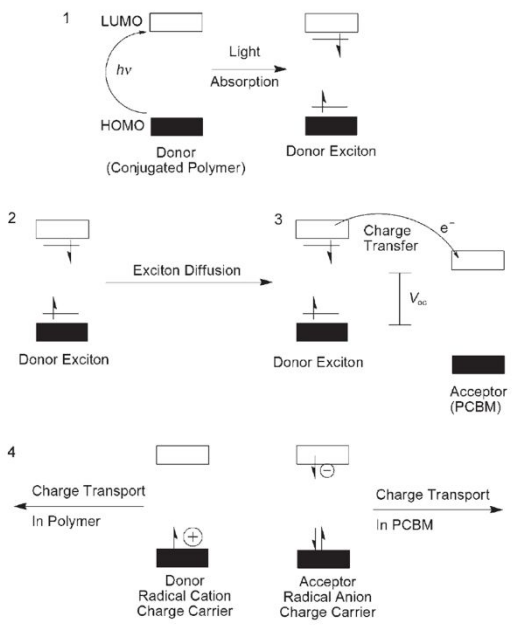


Figure 1-5. General mechanism for power conversion process from incident light to electricity.^[37]

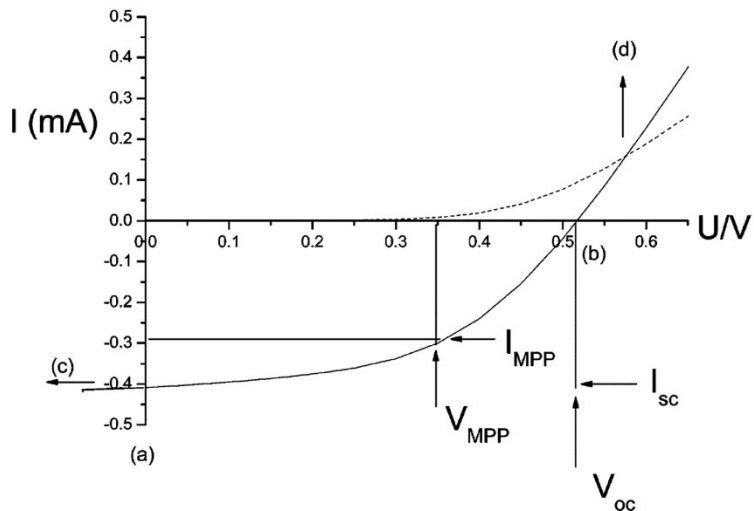


Figure 1-6. Current-voltage curves of an organic solar cell (dashed line: dark, solid line: illuminated).^[33]

1.3. Factors Influencing Charge Carrier Transport

Organic semiconductor materials can be divided into two types; π -conjugated small molecules and polymers. Although, both types of semiconductors have their own merits for being used as organic semiconductor, π -conjugated small molecules have been intensively investigated in terms of in-depth structure-property correlation between molecular structure and electrical properties, owing to their clearly resolved molecule and crystal structure, easy purification, no batch to batch variation, and feasibly controllable molecular structure;^[41] i.e., most importantly, clearly defined chemical structure and intermolecular interaction motif facilitates comprehending electrical characteristics which are directly related to electronical characters of π -conjugated molecules. Therefore, tremendous research efforts have been paid not only to develop high performance organic semiconductor material, but also to understand various physical phenomena in device operation.^[32,42] As a consequence, factors influencing electrical properties and rational molecular design ensuring high device performance were comprehensively explored.^[12,14] Furthermore, new molecular system and advanced concepts are actively investigated these days.

1.3.1. Theoretical Aspect

In assuming that there is absence any chemical and physical defects, charge transport property of organic semiconductor is sensitively affected by electron-phonon interactions and electronic interactions. The origin of electronic and electron-phonon interactions can be comprehended by tight-binding approximation which can be expressed by electronic Hemiltonian as,^[27]

$$H_e = \sum_m \epsilon_m a_m^+ a_m + \sum_{mn} t_{mn} a_m^+ a_n$$

Where, a_m^+ and a_m are the creation and annihilation operator for an electron on lattice site m , respectively, ϵ_m is the electron site energy, and t_{mn} is the transfer integral. The site energy and the transfer integral are defined by as follows;

$$\epsilon_m = \langle \varphi_m(r - R_m) | H_e | \varphi_m(r - R_m) \rangle$$

$$t_{mn} = \langle \phi_m(r - R_m) | H_e | \phi_n(r - R_n) \rangle$$

Where, vector R_m is the position of the site m . Because weak van der Waals interaction is the driving force for constructing solid state organic semiconductor, charge carrier transport in organic systems can be appropriately explained by hopping mechanism at least at room temperature.^[24,43] According to the semi-classical electron transfer theory and extension theory, two key parameters are crucially affected in determining inherent charge carrier mobility; transfer integral and reorganization

energy.^[27] According to the equation for charge transfer rate (k_{et}),^[44]

$$k_{et} = \left(\frac{4\pi^2}{h}\right)t^2(4\pi\lambda RT)^{-0.5}e^{\frac{-\lambda}{4RT}}$$

where, k_{et} is the charge transfer rate, h is Planck constant, t is the transfer integral, λ is the internal reorganization energy, R is the distance between molecular centers, and T is temperature. For the efficient charge carrier transport between molecules in hoping process, high transfer integral and low reorganization energy are required at given molecular system. In case of transfer integral, as shown in **Figure 1-7 a to c**, it is directly related to the electronic coupling which is critically dependent on wavefunction overlap between neighboring molecules. Therefore, various factors influencing solid state intermolecular electronic coupling, for instance, molecular packing structure, intermolecular interaction motif, and π - π distance and their degree of orbital overlap are very important in controlling the charge transport process. On the other hand, internal reorganization energy is affected by the molecular deformation associated with charge transport; although external contribution which is related with surrounding media also exists, it is normally neglected in theoretical calculation.^[27] As shown in **Figure 1-7 d**, the potential energy surface for neutral state and charged state of organic molecules is normally different. This energy difference is originated from molecular geometry difference of both states and should be small to ensure high charge carrier mobility; therefore, degree of intermolecular coupling in their deformation, rigidity of π -conjugated backbone, and conjugation length are largely contributing to

the value of internal reorganization energy.

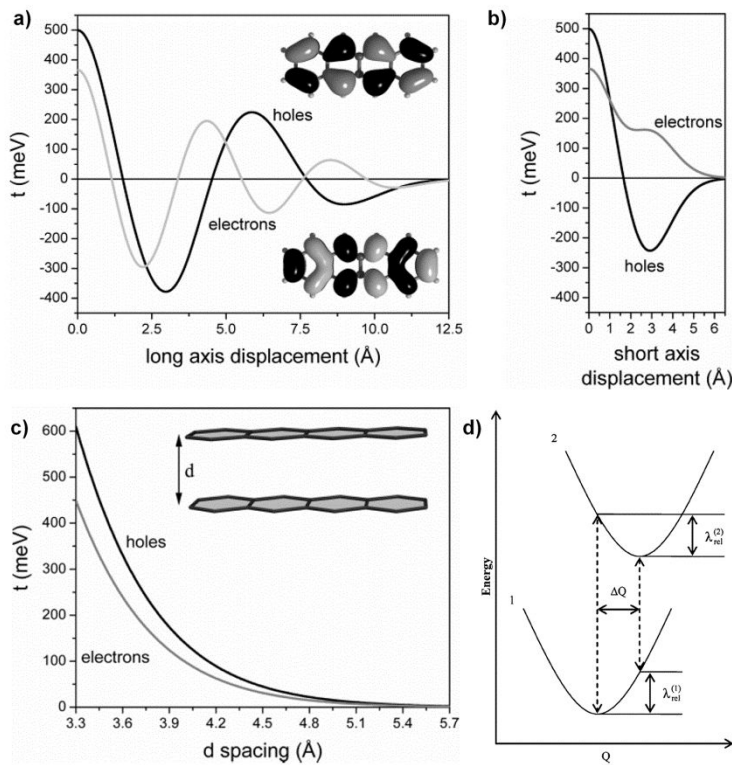


Figure 1-7. Evolution of transfer integrals for tetracene dimer (as a function of (a) along the long axis, (b) along the short axis, and (c) intermolecular distance), and (d) schematic diagram of reorganization energy of neutral state (1, $\lambda_{rel}^{(1)}$) and charged state (2, $\lambda_{rel}^{(2)}$).^[27]

1.3.2. Molecular Packing

As mentioned in the previous section of **Theoretical aspect**, in π -conjugated systems, free charge carriers flow through the overlapping π -orbitals of neighboring molecules. Therefore, solid state electronic structure and charge carrier mobility are determined not only by the chemical structure of the molecule but also by the intermolecular stacking structure. Currently, there are four kinds of stacking structures as shown in **Figure 1-8**;^[45-47] herringbone packing, slipped herringbone packing, 1-dimentional π -stacking, and 2-dimensional π -stacking. Herringbone packing is normally constructed by edge-to-face interaction between neighboring molecules based on tendency for minimizing electrostatic repulsion, and charge carrier propagation could be occurred A and/or B directions (see **Figure 1-8 a**). Generally, polycyclic aromatic hydrocarbones (PAHs) consisting of, for instance, anthracene, tetracene, and pentacene, exhibited herringbone structure, and a family of benzothieno[3,2-b]benzothiophene (BTBT) which is one of the most famous material group as a p-type semiconductor also exhibited herringbone packing motif.^[48-51] Slipped π -stacking, also called cofacial herringbone packing, has face-to-face interaction motif as well as edge-to-face interaction motif. Therefore, transport direction could be formed in diverse way. This slipped π -stacking motif can be derived and observed by small chemical deviation from molecules having herringbone packing motif, such as α -dihexyl-6T and halogenated

PAHs.^[52] In case of 1-dimentional π -stacking, there is preferential propagation direction for molecular stacking, and therefore the direction of π -stacking should be the same direction for the charge carrier transport, resulting in the anisotropic electrical property. On the other hand, 2-dimensional π -stacking, also called brick-wall type, exhibits most strong face-to-face interaction, however, in order to reduce the electrostatic repulsion, there is a displacement along the molecular (long and/or short) axis. This packing structure facilitates 2-dimensional charge carrier transport, and theoretically, most efficient charge carrier transport can be expected owing to the highest value of transfer integral with 2-dimensional transport way.^[53,54] However, it should be noted that most of high charge carrier mobility ($> 10 \text{ cm}^2 \text{ V}^{-1} \text{ s}^{-1}$) have been so far observed for molecules with herringbone packing motifs, such as pentacene, rubrene, and BTBT.^[50,55,56] Even though there are little inconsistency between theoretical modeling and experimental results, it is crucial that solid state electronic structure engineering toward maximizing transfer integral is necessary to afford high carrier mobility in organic semiconductors.

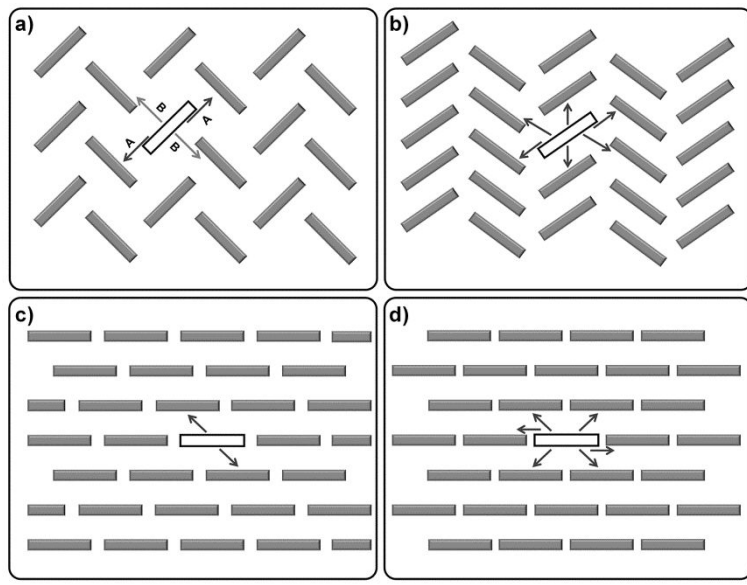


Figure 1-8. Schematic image of four kinds of packing motifs and the preferential charge transport pathways. (a) Herringbone packing, (b) slipped herringbone packing, (c) 1-dimentional π -stacking, and (d) 2-dimentional π -stacking.

1.4. Small Molecule Organic Semiconductors

As mentioned in **Chapter 1.3**, small molecule organic semiconductors have been intensively studied because they facilitate in-depth structure-property correlation. In terms of charge carrier mobility, promising π -conjugated building block for the high performance organic semiconductor is conceptually envisioned to be linear fused acene rings with extended π -conjugated structure. However, large size PAHs, such as pentacene and hexacene, showed severe problems; poor photostability and insufficient solubility in conventional organic solvents. As a successful approach to solve these problems and to improve electrical property, various molecular design strategies were established through chemical structure modification; e.g., functional group substitution on appropriate position, molecular conformation altering, and incorporation of heteroatom in conjugated backbone.

1.4.1. Acene and Their Derivatives

Acenes, a class of PAHs, have attracted attention as a promising organic semiconductor due to their excellent opto-electronic properties. As an active layer of OFETs, anthracene and tetracene exhibited mobility of $0.02\text{ cm}^2\text{ V}^{-1}\text{ s}^{-1}$ and $2.4\text{ cm}^2\text{ V}^{-1}\text{ s}^{-1}$ in single crystal devices, respectively.^[48,49] On the other hand, pentacene single

crystal devices achieved mobility of $15\text{-}40 \text{ cm}^2 \text{ V}^{-1} \text{ s}^{-1}$ through the device optimization.^[50] As shown in **Figure 1-9 a**, these kinds of PAHs exhibited typical herringbone packing motif irrespective of the fused-ring size,^[57-59] On the other hand, electrical characteristics consistently behaved according to theoretical aspect; i.e., charge carrier mobility was enhanced by extension of aromatic backbone attributed to increasing transfer integral and decreasing reorganization energy.^[60] However, as mentioned before, PAHs with large number of fused structure (over five rings) suffered from photooxidation and poor solubility.^[61-62] As an effective solution to these problems, various chemical structure modifications have been conducted. Representatively, Anthony group reported in-depth structure-property correlations of pentacene derivatives with high charge carrier mobility by the chemical structure modification; e.g., incorporating bulky substituents, replacing phenyl rings with thiophene rings, and introducing halogen atom into peripheries (**Figure 1-9 b**).^[63-67] It was noted that, besides enhancement of photostability and solubility, trialkylsilylacetylene substitution at 9- and 10-positon of pentacene gave rise to molecular packing structure alteration, and size of bulky substituents also affected their packing motif alteration. In another case, Bao group and Zhu group reported chlorinated polyaromatic hydrocarbons (PAHs) (5,11-dichlorotetracene and 6,13-dichloropentacene, respectively) which exhibited π -stacking motif with impressive hole mobility ($1.6 \text{ cm}^2 \text{ V}^{-1} \text{ s}^{-1}$ and $9 \text{ cm}^2 \text{ V}^{-1} \text{ s}^{-1}$, respectively) (**Figure 1-9 c**).^[68,69]

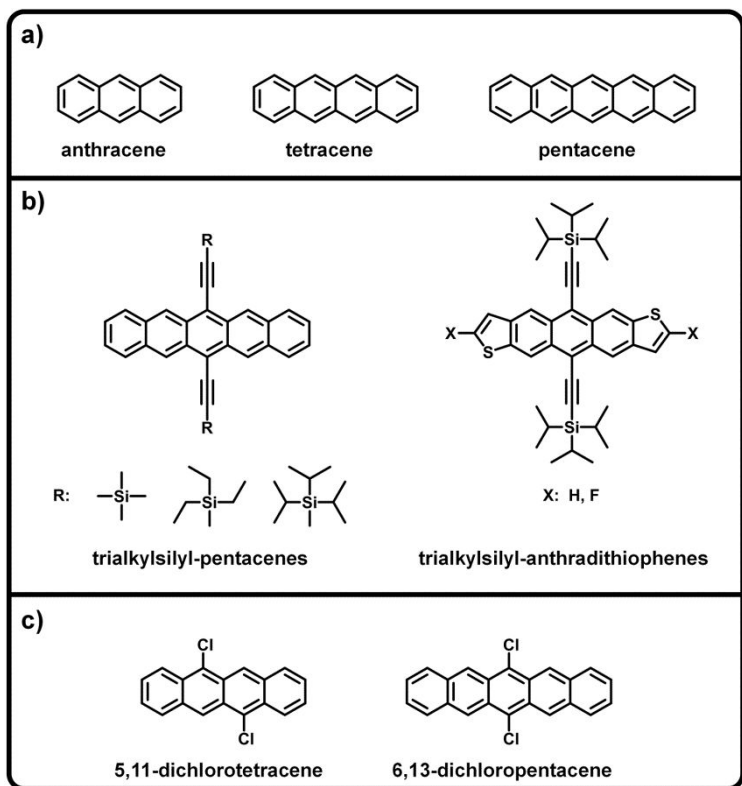


Figure 1-9. Chemical structure of PAHs and their derivatives.

1.4.2. Heteroatom-Containing Fused Aromatics

Heteroatom-containing fused aromatic molecules, of which one or more carbon atoms in fused-backbone are replaced by heteroatoms, also called as heteroacenes, have been explored as another important class of fused π -conjugated molecular system for organic semiconductors. Heteroacenes are considered as a structurally and an electronically fascinating molecular platform based on their rigid backbone, excellent oxidative stability, and tight molecular stacking nature.^[54] Among various types of heteroacenes, chalcogen atom, especially sulfur (S), and nitrogen (N) atom containing-heteroacenes are most intensively investigated until now. As for the sulfur-containing heteroacenes, diverse chemical structures, for instance, oligo-thiophene and thienoacenes, have been extensively investigated since the late 1990s.^[70-72] However, only few thiophene-based molecules afforded comparable mobility to those of amorphous silicon. Among others, thienoacenes of which molecular structure was designed from combination of pentacene and oligothiophene to result in ladder-type thiophene-containing molecules had drawn great interest as a promising organic semiconductor owing to their intriguing advantage of inducing intermolecular secondary interactions, such as S···S, S···H, and S··· π ; which facilitate charge carrier transport as well as changing the packing motif. Because thienoacenes typically exhibit p-channel operation, electronic structure of HOMO for a given molecule plays a key

role to determine its electrical property; i.e., the larger electron density of S atoms in the HOMO and their strong secondary interaction can serve efficient overlap between the HOMO of neighboring molecules in solid state.^[73] As a most successful design for organic semiconductor, among various kinds of thienoacenes, BTBT derivatives which were first reported as an organic semiconductor by Takimiya group, had attracted tremendous interest owing to their high enough solubility to enable solution process and superior charge carrier mobility. The first BTBT derivative for application in OFET, 2,7-diphenyl-BTBT, was reported to have hole mobility of $2.0 \text{ cm}^2 \text{ V}^{-1} \text{ s}^{-1}$ ^[74] after which various BTBT derivatives were reported with mobilities of $0.6 \sim 8 \text{ cm}^2 \text{ V}^{-1} \text{ s}^{-1}$.^[75] Furthermore, its versatile processability facilitated various fabrication methods and conditions (e.g. vacuum deposition, spin-coating, oriented crystallization, inkjet printing, off-centered spin-coating, and so on), to achieve the extreme mobility of $43 \text{ cm}^2 \text{ V}^{-1} \text{ s}^{-1}$.^[76-78] As shown in **Figure 1-10**, most of BTBT derivatives exhibited 2-dimensional lamellar structure with herringbone packing motif. In this herringbone nature, large intermolecular orbital overlap and isotropic two-dimensional (2D) electronic structure originating from edge-to-edge and edge-to-face molecular interactions facilitate efficient charge carrier transport.

Meanwhile, nitrogen-containing heteroacenes also received attentions owing to their low redox potential and capability of secondary bonding interaction ($\text{N-H}\cdots\pi$).^[79] Among various nitrogen-containing heteroacenes, pyrrole-fused heteroacenes, such as carbazole and indolocarbazole, have been intensively investigated as a p-type building

block for the organic semiconductor.^[80-85] In case of pyrrole-fused heteroacenes, besides high antioxidative property, their solubility is easily controllable by the S_N2 reaction at their *N*-position. Moreover, lone pair electrons of *sp*2 hybridized nitrogen atom give rise to electron-sufficiency, and direct electrophilic aromatic substitution reaction at para-position of the *N* atom; of course, para-phenylene type conjugation extension is also possible through the chemical modification during core synthesis, and thus facile electronic structure engineering by molecular structure modulation is possible. Attributed to such synthetic versatility, pyrrole-fused heteroacenes were derived to various types of organic semiconductors, and were adopted for various kinds of organic electronic applications, such as OLEDs, OFETs, and OPVs.^[80-85] Among them, as for the OFET applications, indolocarbazole(ICZ) consisting of two pyrrole rings and three benzene rings and are alternatively fused, have been most intensively investigated. Owing to their linearly fused pentacene like framework and N-H $\cdots\pi$ interaction, non-substituted ICZ single-crystal OFET device exhibited p-type mobility of $1.0 \text{ cm}^2 \text{ V}^{-1} \text{ s}^{-1}$, and those of their derivatives of which chemical structure was altered through *N*-substitution, fused structure extension, and/or further functionalization, exhibited mobilities of $0.01 \sim 1 \text{ cm}^2 \text{ V}^{-1} \text{ s}^{-1}$.^[84-87] Although intensive research efforts have been paid, however, charge carrier mobility of ICZ derivatives are rather lower than those of other high performance ones, especially chalcogenophene-fused derivatives, and also improvement of OFET performance is somewhat stagnant by now.

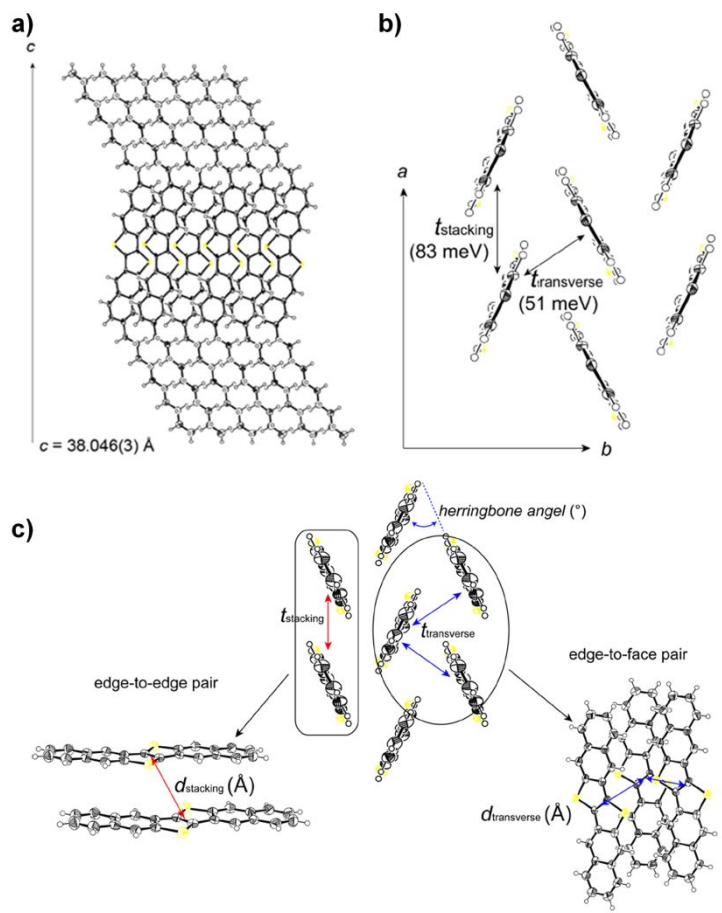


Figure 1-10. (a and b) Packing structure of 2,9-C₁₀-DNTT elucidated by single crystal crystallography, and (c) definitions of intermolecular interaction motif and interaction of BTBT-based derivatives.^[75]

1.5. Research Objective and Contents of Thesis

As mentioned in **Chapter 1.4.2**, heteroacenes have been extensively explored as a structurally and an electronically fascinating molecular platform for applications in organic electronics. As one of the most promising heteroacenes backbone structure, fused pyrrole-containing ones have been intensively investigated based on their strong electron donating nature and controllable π -conjugated system with high flexibility. However, there are still rooms for not only development of novel pyrrole-fused heteroacene core, but also a rational design of chemical structure to develop high performance organic semiconductors. In this respect, among others, I have focused my attention on indolo[3,2-b]indole (IDID) backbone structure, which comprises two inner pyrrole rings and two outer benzene rings fused linearly all together as a promising π -conjugated backbone structure for high performance organic semiconductor. Although the first report of IDID core had been reported in 1911, identified as Golubew's diiminotolane,^[88] only recently it started to receive attention as a backbone structure of organic semiconductor. IDID allows symmetrical structural derivatization in (N,N -, (2,7-), and (3,8-) positions affording diverse opportunities to control their π -conjugation and solubility with high flexibility, with strong electron donating nature attributed to the fused two pyrrole rings. In the fast few years, several IDID-based organic semiconductors have been reported for optoelectronic applications, such as

OFETs, OLEDs, and OSCs.^[89-91] Despite such promising perspective of IDID core, however, systematic study of IDID-based organic semiconductors has seldom been explored so far.

In this thesis, I will provide an elaboration of the IDID core as promising organic semiconductor backbone using newly designed and synthesized family of IDID-based organic semiconductors and their applications in organic electronics, and also propose molecular design strategy to realize high-performance organic semiconductor.

In *Chapter 2*, rational design and versatile processing of IDID-based organic semiconductors will be presented for high-performance OFETs applications.

In *Chapter 3*, intramolecular charge transfer (ICT)-type IDID derivatives consisting of IDID as an electron donor and dicyanovinyl as an electron acceptor with A- π -D- π -A type architecture will be presented for single component ambipoar OFETs applications.

In *Chapter 4*, fluorinated IDID derivatives will be introduced for the purpose of crystal engineering to realize high-performance single crystal (SC) OFETs applications.

In *Chapter 5*, fluorinated IDID derivative as a high-performance crystalline hole transporting material for perovskite solar cells, will be discussed.

In *Chapter 6*, in order to elucidate fluorination effect on properties of IDID derivatives, ICT-type fluorinated IDID derivatives and their BHJ-OSCs applications will be presented.

1.6. References

- [1] C. K. Chiang, C. R. Fincher, Y. W. Park, A. J. Heeger, H. Shirakawa, E. J. Louis, S. C. Gau, A. G. MacDiarmid, *Phys. Rev. Lett.* **1977**, *29*, 1098.
- [2] J. H. Burroighes, D. D. C. Bradley, A. R. Brown, R. N. Marks, K. Mackay, R. H. Friend, P. L. Burns, A. B. Holmes, *Nature* **1990**, *347*, 539.
- [3] A. Kraft, A. C. Grimsdale, A. B. Holmes, *Angew. Chem. Int. Ed.* **1998**, *37*, 402.
- [4] G. Horowitz, *Adv. Mater.* **1998**, *10*, 365.
- [5] Z. Bao, J. A. Rogers, H. E. Kats, *J. Mater. Chem.* **1999**, *9*, 1895.
- [6] H. E. Kats, Z. Bao, S. L. Gilats, *Acc. Chem. Res.* **2001**, *34*, 359.
- [7] C. J. Brabec, N. S. Sariciftci, J. C. Hummelen, *Adv. Funct. Mater.* **2001**, *11*, 15.
- [8] K. M. Coakley, M. D. McGehee, *Chem. Mater.* **2004**, *16*, 4533.
- [9] A. R. Brown, A. Pomp, C. M. Hart, D. M. Deleeuw, *Science* **1995**, *270*, 972.
- [10] B. Crone, A. Dodabalapur, Y. Y. Lin, R. W Filas, Z. Bao, A. LaDuca, R. Sarpeshkar, H. E. Katz, W. Li, *Nature* **2000**, *403*, 521.
- [11] A. R. Murphy, J. M. J. Fréchet, *Chem. Rev.* **2007**, *107*, 1066.
- [12] C. Wang, H. Dong, W. Hu, Y. Liu, D. Zhu, *Chem. Rev.* **2012**, *112*, 2008.
- [13] Y. Shirota, H. Kageyama, *Chem. Rev.* **2007**, *107*, 953.

- [14] H. Dong, X. Fu, J. Liu, Z. Wang, W. Hu, *Adv. Mater.* **2013**, *25*, 6158
- [15] O. D. Jurchescu, M. Popinciuc, B. J. van Wees, T. T. M. Palstra, *Adv. Mater.* **2007**, *19*, 688
- [16] M. Yamagishi, J. Takeya, Y. Tominari, Y. Nakazawa, T. Kuroda, S. Ikehata, M. Uno, T. Nishikawa, T. Kawase, *Appl. Phys. Lett.* **2009**, *90*, 182117
- [17] H. Li, B. C. K. Tee, J. J. Cha, Y. Cui, J.W. Chung, S. Y. Lee, Z. Bao, *J. AM. Chem. Soc.* **2012**, *134*, 2760.
- [18] D.-H. Dou, Y.-Q. Zheng, Z.-F. Yao, Z.-A Yu, T. Lei, X. Shen, X.-Y Luo, J. Sun, S.-D. Zhang, Y.-F Ding, G. Han, Y. Yi, J.-Y. Wang, J. Pei, *J. Am. Chem. Soc.* **2015**, *137*, 15947.
- [19] M. Mas-Torrent, C. Rovira, *Chem. Soc. Rev.* **2008**, *37*, 827.
- [20] J. Zaumseil, H. Sirringhaus, *Chem. Rev.* **2007**, *107*, 1296.
- [21] H. Minemawari, T. Yamada, H. Matsui, J. Tsutsumi, S. Haas, R. Chiba, R. Kumai, T. Hasegawa, *Nature*. **2011**, *475*, 364.
- [22] Y. Yuan, G. Giri, A. L. Ayzner, A. P. Zoumbel, S. C. B. Mannsfeld, J. Chen, D. Nordlund, M. F. Toney, J. Huang, Z. Bao, *Nat. Commun.* **2014**, *5*, 3005.
- [23] W. P. Su, J. R. Schrieffer, A. J. Heeger, *J. Phys. Rev. Lett.* **1979**, *42*, 1698.
- [24] J.-L. Brédas, G. B. Street, *Acc. Chem. Res.* **1985**, *18*, 309.
- [25] J.-L. Brédas, D. Beljonne, V. Coropceanu, J. Cornil, *Chem. Rev.* **2004**, *104*, 4971.
- [26] L. L. Chua, J. Zaumseil, J. F. Chang, E. C. W. Ou, P. K. H. Ho, H. Sirringhaus,

- R. H Friend, *Nature* **2005**, *434*, 194
- [27] V. Coropceanu, J. Cornil, D. A DaSilva Filho,k Y. Olivier, R. Silbey, J.-L. Brédas, *Chem. Rev.* **2007**, *107*, 926.
- [28] R. G. Kepler, *Phys. Rev.* **1960**, *119*, 1226.
- [29] O. H. Leblanc, *J. Chem. Phys.* **1960**, *33*, 626.
- [30] Y. Chen, A.R. Hosseini, M. H. Wong, G. G. Malliaras, *Chem Phys. Chem.* **2004**, *5*, 16.
- [31] A. Tsumura, H. Koezuka, T. Ando, *Appl. Phys. Lett.* **1986**, *49*, 1210.
- [32] C. A. Di, Y. Q. Liu, G. Yu, D. B. Zhu, *Acc. Chem. Res.* **2009**, *42*, 1573.
- [33] S. Gunes, H. Neugebauer, N. S. Sariciftci, *Chem. Rev.* **2007**, *107*, 1324.
- [34] A. J. Heeger, *Adv. Mater.* **2014**, *26*, 10.
- [35] Y. Yu, J. Gao, J. C. Hummelen, F. Wudl, A. J. Heegre, *Science* **1995**, *270*, 1789.
- [36] L. Dou, J. You, Z. Hong, Z. Xu, G. Li, R. A. Street, Y. Yang, *Adv. Mater.* **2013**, *26*, 6642.
- [37] B. C. Thompson, J. M. J. Fréchet, *Angew. Chem. Int. Ed.* **2008**, *47*, 58
- [38] S. R Cowan, C. H. Lee. A. J. Heeger et al. *Chem. Phys. Lett.* **1993**, *213*, 389.
- [39] X. Y. Zhu, *J. Phys. Chem. Lett.* **2014**, *5*, 2283.
- [40] M. Scharber, D. Muhlbacher, M. Koppe, P. Denk, C. Waldauf, A. J. Hegger, C. Brabec, *Adv. Mater.* **2006**, *18*, 789.
- [41] R. Li, W. Hu, Y. Liu, D. Zhu, *Acc. Chem. Res.* **2010**, *43*, 529.

- [42] M. Mas-Torrent, C. Rovira, *Chem. Soc. Rev.* **2008**, *37*, 827.
- [43] A. J. Heeger, S. Kivelson, J. R. Schrieffer, W. P. Su, *Rev. Mod. Phys.* **1988**, *60*, 78.
- [44] V. Balzani, A. Juris, M. Venturi, *Chem. Rev.* **1996**, *96*, 759.
- [45] F. Wurthner, R. Schmidt, *ChemPhysChem* **2006**, *7*, 793
- [46] C. Wang, H. Dong, H. Li, H. Zhao, Q. Meng, W. Hu, *Cryst. Growth Des.* **2010**, *10*, 4155.
- [47] H. Dong, C. Wang, W. Hu, *Chem. Commun.* **2010**, *46*, 5211.
- [48] A. N. Aleshin, J. Y. Lee, S. W. Chu, J. S. Kim, Y. W. Park, *Appl. Phys. Lett.* **2004**, *84*, 5383
- [49] C. Reese, W.-J. Chung, M. Ling, M. Roberts, Z. Bao, *Appl. Phys. Lett.* **2006**, *89*, 202108.
- [50] O. D. Jurchescu, M. Popinciuc, B. J. van Wees, T. T. M. Palstra, *Adv. Mater.* **2007**, *19*, 688.
- [51] K. Takimiya, I. Osaka, T. Mori, M. Nakano, *Acc. Chem. Res.* **2014**, *47*, 1493.
- [52] A. J. Lovinger, H. E. Katz, A. Dodabalapur, *Chem. Mater.* **1998**, *10*, 3275.
- [53] L. Wang, G. Nan, X. Yang, Q. Peng, Q. Li, Z. Shuai, *Chem. Soc. Rev.* **2010**, *39*, 423
- [54] J. E. Anthony, *Chem. Rev.* **2006**, *106*, 5028
- [55] M. Yamagishi, J. Takeya, Y. Tominari, Y. Nakazawa, T. Kuroda, S. Ikehata, M. Uno, T. Nishikawa, T. Kawase, *Appl. Phys. Lett.* **2009**, *90*, 182117

- [56] Y. Yuan, G. Giri, A. L. Ayzner, A. P. Zombelt, S. C. B. Mannsfeld, J. Chen, D. Nordlund, M. F. Toney, J. Huang, Z. Bao, *Nat. Commun.* **2014**, *5*, 3005.
- [57] C. P. Brock, J. D. Dunitz, *Acta Cryst. C* **1990**, *46*, 795.
- [58] D. Holmes, S. Kumaraswamy, A. J. Matzger, K. P. C. Vollhardt, *Chem. Euro. J.* **1999**, *5*, 3399.
- [59] C. C. Mattheus, A. B. Dros, J. Baas, A. Meetsma, J. L. D. Boer, T. T. M. Palstra, *Acta Cryst. C* **2001**, *57*, 939.
- [60] M. Watanabe, Y. J. Chang, W.-W. Liu, T.-H. Chao, K. Goto, M. IslamMd, C.-H Yuan Y.-T Tao, T. Shinmyozu, T. J. Chow, *Nat. Chem.* **2012**, *4*, 574.
- [61] K. Ito, T. Suzuki, Y. Sakamoto, D. Kudota, Y. Inoue, F. Sato, S. Tokito, *Angew. Chem. Int. Ed.* **2003**, *42*, 1159
- [62] H. Klauk, U. Zschieschang, R. T. Weitz, H. Meng, F. Sun, G. Nunes, D. E. Keys, C. R. Fincher, Z. Xiang, *Adv. Mater.* **2007**, *19*, 3882.
- [63] J. E. Anthony, J. S. Brooks, D. L. Eaton, S. R. Parkin, *J. Am. Chem. Soc.* **2001**, *123*, 9482
- [64] M. M. Payne, S. R. Parkin, J. E. Anthony, C.-C. Kuo, T. N. Jackson, *J. Am. Chem. Soc.* **2005**, *127*, 4986
- [65] J. E. Anthony, D. L. Eaton, S. R. Parkin, *Org. Lett.* **2002**, *4*, 15
- [66] C. D. Sheraw, T. N. Jackson, D. L. Eaton, J. E. Anthony, *Adv. Mater.* **2003**, *15*, 2009
- [67] S. Subramanian, S. K. Park, S. R. Parkin, V. Podzorov, T. N. Jackson, J. E.

Anthony, *J. Am. Chem. Soc.* **2008**, *130*, 2706.

- [68] H. Moon, R. Zeis, E.-J. Borkent, C. Besnard, A. J. Lovinger, T. Siegrist, C. Kloc, Z. Bao, *J. Am. Chem. Soc.* **2004**, *126*, 15322.
- [69] M. Wang, J. Li, G. Zhao, Q. Wu, Y. Huang, W. Hu, X. Gao, H. Li, D. Zhu, *Adv. Mater.* **2013**, *25*, 2229.
- [70] G. Horowiz, F. Garnier, A. Yassar, R. Hajlaoui, F. Kouki, *Adv. Mater.* **1996**, *8*, 52.
- [71] J. G. Laquindanum, H. E. Katz, A. J. Lovinger, A. Dodavalapur, *Adv. Mater.* **1997**, *9*, 36.
- [72] X.-C Li, G. Sirringhaus, F. Garnier, A. B. Holmes, S. C. Moratti, N. Feeder, W. Clegg, S. J. Teat, R. H. Friend, *J. Am. Chem. Soc.* **1998**, *120*, 2206.
- [73] K Takimiya, S. Shinamura, I. Osaka, E. Miyazaki, *Adv. Mater.* **2011**, *23*, 4347
- [74] K. Takimiya, H. Ebata, K. Sakamoto, T. Izawa, T. Otsubo, Y. Kunugi, *J. Am. Chem. Soc.* **2006**, *128*, 12604.
- [75] K. Takimiya, I. Osaka, T. Mori, M. Nakano, *Acc. Chem. Res.* **2014**, *47*, 1493.
- [76] H. Minemawari, T. Yamada, H. Matsui, J. Tsutsumi, S. Haas, R. Chiba, R. Kumai, T. Hasegawa, *Nature*. **2011**, *475*, 364.
- [77] J. Soeda, Y. Hirose, M. Yamagishi, A. Nakao, T. Uemura, K. Nakayama, M. Uno, Y. Nakazawa, K. Takimiya, J. Takeya, *Adv. Mater.* **2011**, *23*, 3309.
- [78] Y. Yuan, G. Giri, A. L. Ayzner, A. P. Zombeck, S. C. B. Mannsfeld, J. Chen, D. Nordlund, M. F. Toney, J. Huang, Z. Bao, *Nat. Commun.* **2014**, *5*, 3005.

- [79] H. Zhao, L. Jiang, H. Dong, H. Li, W. Hu, B. S. Ong, *ChemPhysChem* **2009**, *10*, 2345.
- [80] T. V. Pho, J. D. Yuen, J. A. Kurzman, B. G. Smith, M. Miao, W. T. Walker, R. Seshadri, F. Wudl, *J. Am. Chem. Soc.* **2012**, *134*, 18185.
- [81] Y. Wu, Y. Li, S. Gardner, B. S. Ong, *J. Am. Chem.* **2005**, *127*, 614.
- [82] J. F. Morin, N. Drolet, Y. Tao, M. Leclerc, *Chem. Mater.* **2004**, *16*, 4619.
- [83] N. Drolet, J. F. Morin, N. Leclerc, S. Wakim, Y. Tao, M. Leclerc, *Adv. Funct. Mater.* **2005**, *15*, 1671.
- [84] H. Jiang, H. Zhao, K. K. Zhang, X. Chen, C. Kloc, W. Hu, *Adv. Mater.* **2012**, *23*, 5075.
- [85] P. L. T. Boudreault, S. Wakim, N. Blouin, M. Simard, C. Tessier, Y. Tao, M. Leclerc, *J. Am. Chem. Soc.* **2007**, *129*, 9125.
- [86] P. L. T. Boudreault, S. Wakim, M. L. Tang, Y. Tao, Z. Bao, M. Leclerc, *J. Mater. Chem.* **2009**, *19*, 2921.
- [87] G. Zhao, H. Dong, H. Zhao, L. Jiang, X. Zhang, J. Tan, Q. Meng, W. Hu, *J. Mater. Chem.* **2012**, *22*, 4409.
- [88] A. Janiga, D. T. Cryko, *Chem. Asian J.* **2014**, *9*, 3036
- [89] Y. Y. Lai, J. M. Yeh, C. E. Tsai, Y. J. Cheng, *Eur. J. Org. Chem.* **2013**, *23*, 5076.
- [90] Z. R. Owczarczyk, W. A. Braunecker, A. Garcia, R. Larsen, A. M. Nardes, N. Kopidakis, D. S. Ginley, D. C. Olson, *Macromolecules* **2013**, *46*, 1350.

[91] L. Qiu, C. Yu, N. Zhao, W. Chen, Y. Guo, X. Wan, R. Yang, Y. Liu, *Chem. Commun.* **2012**, *48*, 12225.

Chapter 2.

Design, Synthesis, and Versatile Processing of Indolo[3,2-b]indole-based π -Conjugated Molecules for High-Performance Organic Field-Effect Transistor

2.1. Introduction

Since the first organic field-effect transistor (OFET) was reported by Tsumura in 1986,^[1] organic semiconductors have been attracting significant attention as a potential alternative to the prevalent silicon-based semiconductor by virtue of large area and low cost fabrication, good mechanical property, flexibility, and so on.^[2-4] To achieve high-performance OFET, a wide range of organic π -conjugated molecules have been designed and synthesized.^[5,6] In particular, heteroatom-containing fused aromatic molecules (heteroacenes) have been explored as a structurally and an electronically fascinating molecular platform based on their rigid and extended π -conjugation, excellent oxidative stability, and tight molecular stacking.^[7,8]

Among various types of heteroacenes, fused thiophene- and fused pyrrole-containing ones have been extensively investigated for their molecular structural variation (e.g. number of rings in polyacene analogue, position of incorporated heteroatom, and

additional functional group substitution). As for the fused thiophene-containing heteroacenes, remarkable progress has already been made to the optimized high performance organic semiconductor.^[9] Representatively, Takimiya group reported a family of benzothieno[3,2-b]benzothiophene (BTBT) derivatives with mobilities of $0.6\sim8\text{ cm}^2\text{ V}^{-1}\text{ s}^{-1}$.^[10,11] Even C_n-BTBT ($n=5\sim14$, alkylated BTBT) which is designed for solution-processable OFET, also exhibited comparable mobilities with those of highly π -extended BTBT derivatives, attributed to large intermolecular overlap and isotropic two-dimensional (2D) electronic structure in solid state. Furthermore, its versatile processability facilitated employing various fabrication methods and conditions (e.g. vacuum deposition, spin-coating, oriented crystallization, inkjet printing, off-centered spin-coating, and so on), to achieve the extreme mobility of $43\text{ cm}^2\text{ V}^{-1}\text{ s}^{-1}$.^[12-14] Meanwhile, fused pyrrole-containing heteroacenes (e.g. indole, carbazole, indoloindole, and indolocarbazole) also received attention owing to their low redox potential, controllable solubility, and feasibility for molecular structure modification.^[15-20] Among others, indolocarbazole and its derivatives have been most extensively investigated owing to their coplanar pentacene-like structure; representatively, Leclerc group and Hu group reported families of indolo[3,2-b]carbazole (IC) derivatives with mobilities of $10^{-3}\sim1\text{ cm}^2\text{ V}^{-1}\text{ s}^{-1}$.^[19-22] However, report of versatile processable IC derivatives which exhibit high charge carrier mobility are still rare, and also, the improvement of OFET performance is somewhat stagnant by now. This is most probably due to the limited solubility of IC backbone consisting of

five fused aromatic rings, which barely improves even after introducing substituent groups. Therefore, I have been more interested with rather smaller size pyrrole-fused heteroacenes and their derivatives which should show balanced mobility and versatile processibility.

In this respect, I have focused interest on indolo[3,2-b]indole (IDID) backbone, which comprises two inner pyrrole rings and two outer benzene rings fused all together to give centro-symmetrical conjugated backbone. IDID thus allows symmetrical structural derivatization in (*N,N*)-, (2,7)-, and (3,8-) positions affording diverse opportunities to control their π -conjugation and solubility with higher flexibility than the case of pentacene and heptacene analogues (e.g. indolocarbazole, and heptazole). Despite such promising perspective of IDID core, its optoelectronic application has seldom been explored so far.^[23-25] In case of OFET application, only one paper on vacuum-deposited (VD) device was reported with underivatized IDID core which showed rather low mobility value of ca. $1.0 \times 10^{-3} \text{ cm}^2 \text{ V}^{-1} \text{ s}^{-1}$.^[25] I thus believe it is worthwhile to tailor molecular structures of IDID with an aim to realize high-performance and versatile processable organic semiconductors *via* precise comprehension of structure-property relationship. I herein report four newly synthesized IDID derivatives, 2H2TIDID, 4H2TIDID, 2H4TIDID, and 4H4TIDID, of which aromatic and aliphatic substituents were delicately designed. Among these new class of organic semiconductors, 4H4TIDID exhibited excellent p-type field-effect

mobility of $0.97 \text{ cm}^2 \text{ V}^{-1} \text{ s}^{-1}$ from VD-OFET device. Moreover, spin-coated device also exhibited high mobility value (up to $0.18 \text{ cm}^2 \text{ V}^{-1} \text{ s}^{-1}$) interestingly without any post-annealing procedures, manifesting a great potential of IDID derivatives for practical flexible electronics applications.

2.2. Experimental

Synthesis

Synthesis route to four IDID derivatives, 2H2TIDID, 4H2TIDID, 2H4TIDID, and 4H4TIDID is shown in Scheme 2-1. Unless otherwise stated, all reagents were purchased at Sigma Aldrich, TCI, and Alfa Aeasar.

Synthesis of 4-bromo-1-iodo-2-nitrobenzene (**2**).

A mixed solution of water (38 mL) and H_2SO_4 (35 mL) was added dropwise to the solution of 4-bromo-2-nitroaniline (10.851 g, 50 mmol) in acetic acid (35 mL) at 0°C . Afterwards, a solution of NaNO_2 (3.795 g, 55 mmol, in 15 mL H_2O) was added dropwise and stirred for an hour. After then, a solution of KI (9.96 g, 60 mmol, in 15 mL H_2O) was drop wisely added and the reaction mixture was gently refluxed at 60°C . After 3 hours later, reaction vessel was cooled down to 0°C again, and methylene chloride was added to dissolve all precipitates. The reaction mixture was poured into saturated NaHCO_3 aqueous solution (400 mL) in ice bath. The organic phase was

separated and washed with brine and saturated $\text{Na}_2\text{S}_2\text{O}_3$ aqueous solution (500 mL) sequentially. The combined organic phase was dried with MgSO_4 and concentrated under reduced pressure. The crude product was purified by recrystallized from ethanol to afford compound **2** as an orange powder (14.56, 77.1%). $^1\text{H-NMR}$ (300 MHz, CDCl_3 , δ): 7.99 (s, 1H), 7.90 (d, $J = 8.4$ Hz, 1H), 7.41 (dd, $J = 8.2$ Hz, $J = 1.5$ Hz, 1H)

Synthesis of (4-bromo-2-nitro-phenylethynyl)-trimethyl-silane (**3**).

A mixed solution of 4-bromo-1-iodo-2-nitrobenzene (compound **2**, 5 g, 15.248 mmol), bis(triphenylphosphine)palladium(II) dichloride (0.535 g, 0.762 mmol), copper(I) iodide (0.29 g, 1.525 mmol), and tetrahydrofuran (40 mL) was purged with argon (Ar) gas. After then, trimethylsilylacetylene (1.5 g, 15.248 mmol) and triethylamine (10 mL) was added, and mixed solution was stirred at room temperature. After 3 hours, the reaction mixture was filtered through a silica plug and concentrated under reduced pressure. The concentrated filtrate was purified by column chromatography (ethyl acetate/n-hexane 1:9, v/v) to afford compound **3** as brown oil (4.12 g, 90.6%). $^1\text{H-NMR}$ (300 MHz, CDCl_3 , δ): 8.16 (d, $J = 1.62$ Hz, 1H), 7.69 (dd, $J = 8.22$ Hz, $J = 1.68$ Hz, 1H), 7.52 (d, $J = 8.28$ Hz, 1H), 0.27 (s, 9H)

Synthesis of 4-bromo-1-ethynyl-2-nitrobenzene (**4**).

A mixed solution of (4-bromo-2-nitro-phenylethynyl)-trimethyl-silane (compound **3**, 3.77 g, 15.642 mmol), K_2CO_3 (1.922 g, 13.906 mmol), methanol (40 mL), and MC (80 mL) was stirred at room temperature. After 10 hours, the reaction mixture was poured into water (300 mL), and extracted with methylene chloride. The combined organic

phase was dried with MgSO₄ and concentrated under reduced pressure. The crude product was purified by flash column chromatography (ethyl acetate/n-hexane 1:3, v/v) to afford compound **4** as a brown powder (2.79 g, 97.6%). ¹H-NMR (300 MHz, CDCl₃, δ): 8.20 (d, J = 1.2 Hz, 1H), 7.73 (dd, J = 8.34 Hz, J = 1.23 Hz, 1H), 7.57 (d, J = 8.28 Hz, 1H), 3.57 (s, 1H)

Synthesis of 4,4'-dibromo-2,2'-dinitrotolane (**5**).

5 was synthesized from **4** by the same synthetic procedure used for **3** with 4-bromo-1-ethynyl-2-nitrobenzene (**4**, 3.02 g, 13.361 mmol), 4-bromo-1-iodo-2-nitrobenzene (**2**, 4.382 g, 13.361 mmol), bis(triphenylphosphine)palladium(II) dichloride (0.469 g, 0.668 mmol), copper(I) iodide (0.25 g, 1.336 mmol), tetrahydrofuran (60 mL), and triethylamine (12 mL) were used. Flash column chromatography (chloroform, CHCl₃) and recrystallization (CHCl₃) were exerted to afford the compound **5** as a brown solid (3.43 g, 60.3%). ¹H-NMR (300 MHz, CDCl₃, δ): 8.31 (d, J = 1.74 Hz, 2H), 7.81 (dd, J = 8.31 Hz, J = 1.83 Hz, 2H), 7.69 (d, J = 8.28 Hz, 2H)

Synthesis of 4,4'-dibromo-2,2'-dinitrobenzil (**6**)

A mixed solution of potassium permanganate (2.815 g, 17.816 mmol), Adogen 464 (catalytic amount), water (60 mL), methylene chloride (80 mL), and acetic acid (3 mL) was purged with Ar gas. After then, 4,4'-dibromo-2,2'-dinitrotolane (**5**, 2.53 g 5.938 mmol) was added and gently refluxed for 5 hours, cooled, and decolorized (using NaHSO₃), sequentially. The combined organic phase was dried with MgSO₄ and filtered through a silica plug. The yellow filtrate was concentrated under reduced

pressure, and the resulting solid was washed with methanol to afford compound **6** as a yellow crystalline solid (2.45 g, 91%). ¹H-NMR (300 MHz, CDCl₃, δ): 8.41 (d, J = 1.71 Hz, 2H), 8.03 (dd, J = 8.1 Hz, J = 1.74 Hz, 2H), 7.54 (d, J = 8.1 Hz, 2H)

Synthesis of 2,7-dibromo-5,10-dihydroindolo[3,2-b]indole (**7**).

The filtrate of stannous chloride (24.7 g, 124.375 mmol), acetic acid (60 mL), and 1 N HCl (24 mL) mixed solution was added to a solution of 4,4'-dibromo-2,2'-dinitrobenzil (**6**, 2.811 g, 6.218 mmol) in warm acetic acid (50 mL). The reaction mixture was gently refluxed for 5 hours at 80°C. The resulting precipitates were filtered, and filtered out was washed with acetic acid, 1 N HCl, water, and ethanol. The crude product was purified by flash column chromatography (ethyl acetate) and washing (chloroform) to afford the compound **7** as a gray solid (1.24 g, 55.5%). ¹H-NMR (300 MHz, Acetone-*d*₆, δ): 10.51 (s, 2H), 7.74 (d, J = 8.37 Hz, 2H), 7.73 (d, J = 1.56 Hz, 2H), 7.25 (dd, J = 8.49 Hz, J = 1.59 Hz, 2H)

Synthesis of 2,7-dibromo-5,10-dihexyl-5,10-dihydroindolo[3,2-b]indole (**8**).

A round-bottom flask, equipped with a magnetic stirrer bar and reflux condenser was baked under reduced pressure and backfilled with Ar. After then, 2,7-dibromo-5,10-dihydroindolo[3,2-b]indole (**7**, 1.5 g, 4.120 mmol), anhydrous tetrahydrofuran (40 mL), and NaH (0.39 g, 16.482 mmol) were added to the baked reaction vessel. After 10 minutes at room temperature, 2.72 g (16.482 mmol) of 1-bromohexane was added to the reaction mixture. After stirring for 10 minutes, the reaction mixture was gently refluxed for 48 hours. Then, the reaction mixture was poured into brine (300 mL), and

extracted with methylene chloride. The combined organic phase was dried with MgSO₄ and concentrated under reduced pressure. The crude product was purified by flash column chromatography (ethyl acetate/n-hexane 1:4, v/v) and subsequently by recrystallization (ethyl acetate) to afford compound **8** as white crystalline solid (1.65 g, 75%). ¹H-NMR (300 MHz, CDCl₃, δ): 7.66 (d, J = 8.43 Hz, 2H), 7.58 (d, J = 1.56 Hz, 2H), 7.28 (dd, J = 8.37 Hz, J = 1.65 Hz, 2H), 4.42 (t, J = 7.17 Hz, 4H), 1.92 (m, J = 7.23Hz, 4H), 1.39~1.23 (m, 12H), 0.84 (t, J = 7.08 Hz, 6H)

Synthesis of **2H2TIDID**

A mixed solution of 2,7-dibromo-*N,N*-dihexyl-IDID (0.500 g, 0.965 mmol), 2-(tributylstanny)thiophene (0.756 g, 2.026 mmol), and toluene (30 mL) was purged with an argon (Ar) gas, and tetrakis(triphenylphosphine)palladium(0) (0.110 g, 0.096 mmol) was added. The reaction mixture was gently refluxed at 110 °C with stirring under an Ar atmosphere. After 24 hours, the reaction mixture was quenched with distilled water (300 mL) and extracted with methylene chloride (300 mL). The combined organic phase was dried with MgSO₄ and concentrated under reduced pressure. The crude product was purified by flash column chromatography (ethyl acetate/n-hexane 1:1, v/v) and subsequently by recrystallization (ethyl acetate) to afford **2H2TIDID** as yellow crystal (0.332 g, 63.5 %) ¹H-NMR (500 MHz, THF-*d*8, δ): 7.846(d, *J* = 8.5 Hz, 2H), 7.765(S, 2H), 7.433(d, *J* = 9.5 Hz, 2H), 7.414(d, *J* = 3.5 Hz, 2H), 7.317(d, *J* = 4.5 Hz, 2H), 7.072(d, *J* = 7 Hz, 2H), 4.584(t, *J* = 7 Hz, 4H), 1.992(m, *J* = 7.5 Hz, 4H), 1.460(m, *J* = 7.5 Hz, 4H), 1.356(m, *J* = 8.5, 4H), 1.288(m, *J* = 7.5 Hz,

4H), 0.847(t, $J = 7$ Hz, 6H), ^{13}C NMR (500MHz, Tetrahydrofuran-d8, δ): 147.22, 142.42, 129.51, 128.82, 127.84, 124.73, 123.22, 118.93, 117.94, 115.09, 107.94, 45.91, 32.73, 31.37, 27.77, 23.59, 14.48, HRMS(FAB, m/z): Calcd. for $\text{C}_{34}\text{H}_{38}\text{N}_2\text{S}_2$: 538.25, found: 538.2483, Elem. Anal. Calcd. For $\text{C}_{34}\text{H}_{38}\text{N}_2\text{S}_2$: C 75.79, H 7.11, N 5.20, S 11.90; found: C 75.70, H 6.99, N 5.30, S 11.80.

Synthesis of **4H2TIDID**

A mixed solution of 2,7-dibromo-*N,N*-dihexyl-IDID (1.400 g 2.629 mmol), 5-hexylthiophene-2-boronic acid pinacol ester (1.586 g, 5.391 mmol), and tetrahydrofuran (80 mL), was purged with Ar gas, and tetrakis(triphenylphosphine)palladium(0) (0.304 g, 0.263 mmol) was added. The reaction mixture was gently refluxed at 80 °C with stirring under an Ar atmosphere. After 24 hours, the reaction mixture was quenched with distilled water (300 mL), neutralized (1 N HCl), and extracted with methylene chloride. The combined organic phase was dried with MgSO_4 and concentrated under reduced pressure. The crude product was purified by flash column chromatography (chloroform/n-hexane 1:2, v/v) and subsequently by recrystallization (ethyl acetate) to afford **4H2TIDID** as yellow crystal (1.321 g, 70.9%) ^1H -NMR (500 MHz, THF-d8, δ): 7.806(d, $J = 8$ Hz, 2H), 7.682(S, 2H), 7.370(d, $J = 8$ Hz, 2H), 7.199(d, $J = 3.5$ Hz, 2H), 6.764(d, $J = 3.5$ Hz, 2H), 4.599(t, $J = 6.5$ Hz, 4H), 2.840(t, $J = 7.5$ Hz, 4H), 1.980(m, $J = 7.5$ Hz, 4H), 1.727(m, 4H), 1.484~1.259(m, 24H), 0.917(t, $J = 7$ Hz, 6H), 0.849(t, $J = 7$ Hz, 6H). ^{13}C NMR (500MHz, Tetrahydrofuran-d8, δ): 145.17, 144.68, 142.40, 129.82, 127.73,

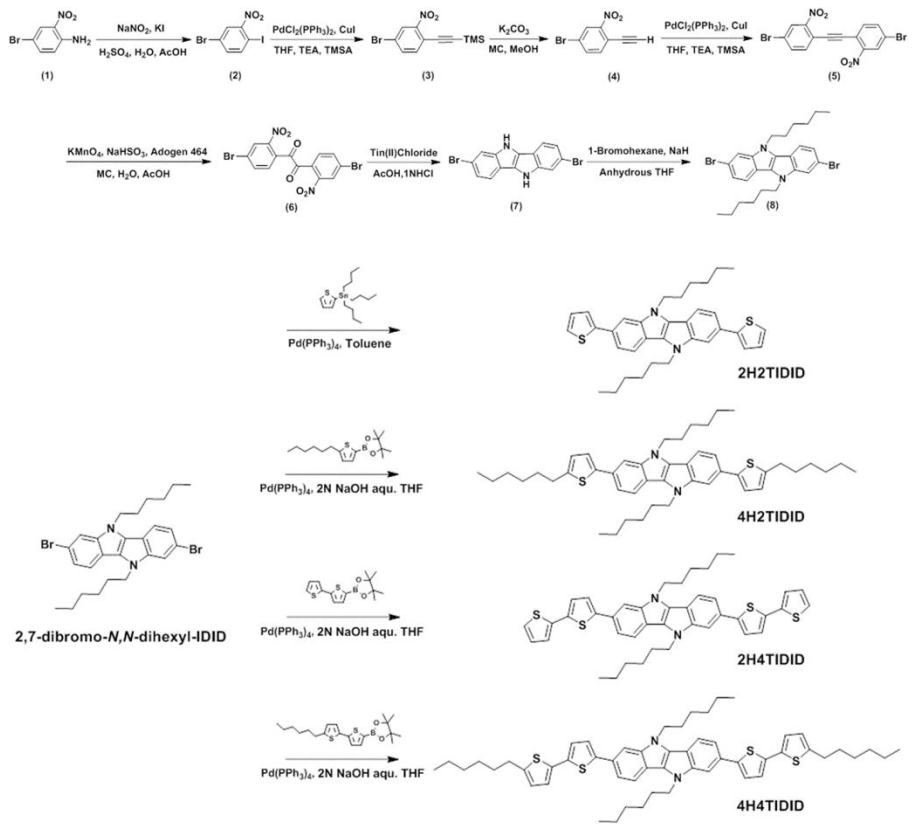
126.03, 122.72, 118.78, 117.55, 114.85, 107.43, 45.89, 32.87, 32.75, 31.37, 31.18, 29, 27.77, 23.65, 23.59, 14.57, 14.49. HRMS(FAB, m/z): Calcd. for C₄₆H₆₂N₂S₂: 706.44, found: 706.4359. Elel. Anal. Calcd. For C₄₆H₆₂N₂S₂: C 78.13, H 8.84, N 3.96, S 9.07; found: C 78.06, H 8.88, N 4.00, S 9.12.

Synthesis of **2H4TIDID**

2H4TIDID was synthesized by the same synthetic procedure as **4H2TIDID**, using 2,7-dibromo-*N,N*-dihexyl-IDID (1.400 g 2.629 mmol), 2,2'-bithiophene-5-boronic acid pinacol ester (1.575 g, 5.391 mmol), tetrakis(triphenylphosphine)palladium(0) (0.304 g, 0.263 mmol), tetrahydrofuran (100 mL), and 2 N NaOH aqueous solution (40 mL). The crude product was purified by flash column chromatography (chloroform) and subsequently by recrystallization (THF) to afford **2H4TIDID** as yellow crystal (1.272 g, 68.7%) ¹H-NMR (500 MHz, Tetrahydrofuran-d8, δ): 7.867(d, *J* = 8 Hz, 2H), 7.784(s, 2H), 7.452(d, *J* = 8 Hz, 2H), 7.375(d, *J* = 4 Hz, 2H), 7.377(d, *J* = 5 Hz, 2H), 7.251(d, *J* = 3.5 Hz, 2H), 7.215(d, *J* = 4 Hz, 2H), 7.031(t, *J* = 5 Hz, 2H), 4.607(t, *J* = 7 Hz, 4H), 2.004(m, *J* = 7.5 Hz, 4H), 1.470(m, *J* = 7.5, 4H), 1.394-1.254(m, 8H), 0.856(t, *J* = 7.5 Hz, 6H). ¹³C NMR (500MHz, THF-*d*8, δ): 129.09, 128.78, 128.11, 126.97, 125.57, 125.19, 124.19, 123.96, 122.11, 119.08, 117.59, 107.68, 105.81, 45.93, 32.77, 31.40, 21.76, 14.51, 12.69. HRMS(FAB, m/z): Calcd. for C₄₂H₄₂N₂S₄: 702.22, found: 702.2252. Elel. Anal. Calcd. for C₄₂H₄₂N₂S₄: C 71.75, H 6.02, N 3.98, S 18.24; found: C 71.49, H 6.00, N 4.05, S 18.43.

Synthesis of **4H4TIDID**

4H4TIDID was synthesized by the same synthetic procedure as **4H2TIDID**, using 2,7-dibromo-*N,N*-dihexyl-IDID (1.400 g 2.629 mmol), 5'-hexyl-2,2'-bithiophene-5-boronic acid pinacol ester (2.029 g, 5.391 mmol), tetrakis(triphenylphosphine)palladium(0) (0.304 g, 0.263 mmol), tetrahydrofuran (80 mL), and 2 N NaOH aqueous solution (40 mL). The crude product was purified by flash column chromatography (chloroform /n-hexane 1/4 v/v) and subsequently by recrystallization (ethyl acetate) to afford **4H4TIDID** as yellow crystal (1.694 g, 73.7%).
¹H-NMR (500 MHz, THF-*d*8, δ): 7.860(d, *J* = 8 Hz, 2H), 7.761(s, 2H), 7.433(d, *J* = 8 Hz, 2H), 7.339(d, *J* = 3.5 Hz, 2H), 7.117(d, *J* = 4 Hz, 2H), 7.041(d, *J* = 3.5 Hz, 2H), 6.729(d, *J* = 3.5 Hz, 2H), 4.590(t, *J* = 7 Hz, 4H), 2.819(t, *J* = 7.5 Hz, 4H), 1.997(m, *J* = 7.5 Hz, 4H), 1.706(m, *J* = 8Hz, 4H), 1.495-1.267(m, 24H), 0.913(t, *J* = 6 Hz, 6H), 0.855(t, *J* = 7 Hz, 6H). ¹³C NMR (500MHz, Tetrahydrofuran-*d*8, δ): 145.79, 145.48, 142.47, 137.23, 136.32, 129.15, 128.04, 125.96, 124.82, 123.83, 119.02, 117.54, 115.06, 107.57, 45.92, 32.75, 32.72, 31.38, 31.01, 29.83, 27.77, 23.63, 23.60, 14.56, 14.50.
HRMS(FAB, m/z): Calcd. for C₅₄H₆₆N₂S₄: 870.41, found: 870.4113. Elel. Anal. Calcd. for C₅₄H₆₆N₂S₄:: C 74.43, H 7.63, N 3.21, S 14..72; found: C 74.30, H 7.52, N 3.26, S 14.89.



Scheme 2-1. Synthetic route for IDID derivatives and their chemical structures.

Characterization:

Chemical structures were fully identified by ^1H NMR and ^{13}C NMR (Bruker, Advance-300 and Advance-500), GC-Mass (JEOL, JMS-700), and elemental analysis (CE Instrument, EA1110). UV-vis spectra were recorded on a SHIMADZU UV-1650PC. HOMO levels of organic materials were obtained from the cyclic voltammetry measurements. Cyclic voltammetry measurements were performed using a 273A (Princeton Applied Research) with a one-compartment platinum working electrode, a platinum wire counter-electrode, and a quasi Ag^+/Ag electrode as a reference. Measurements were performed in a 0.5 mM methylene chloride solution with 0.1 M tetrabutylammonium tetrafluoroborate as supporting electrolyte, and acetonitrile with 0.1 M tetrabutylammonium tetrafluoroborate for film as a supporting electrolyte, at a scan rate of 50 mV/s. Each oxidation potential was calibrated using ferrocene as a reference. LUMO levels were evaluated with the HOMO level and the optical band-gap, which was obtained from the edge of the film absorption spectra. Single-crystal structure analysis was carried out with a SMART-APEX II ULTRA (Bruker). Two-dimensional grazing incidence X-ray diffraction (2-D GIXD) was done at the 3C Beam-line of Pohang Acceleration Laboratory. Film surface topologies were obtained by a Bruker Nanoscope III multimode SPM with tapping mode using TREST cantilever. Density functional theory (DFT) calculations were performed using Gaussian 09 package with the basis set of B3LYP, 6-31G d, p. The I - V characteristics of all devices were measured using a Keithley 4200 SCS.

Device fabrication and measurement:

As a OFET substrate, SiO₂/Si wafer (p-doped 300 nm) was rinsed with acetone and isopropyl alcohol, respectively, for 10 minute in an ultrasonicator, followed by 15 minute UV (360 nm) O₃ treatment.

For the thermally evaporated vacuum deposited polycrystalline OFET device fabrication, octadecyltrichlorosilane (ODTS) was treated as self-assembled monolayer (SAM) on the prepared substrate, to reduce charge trap sites as well as to enlarge domain size. ODTS was treated in vapor phase in a vacuum oven; then the substrates were passed into nitrogen filled glove box. Organic semiconductor active layers of ~30 nm thickness were thermally deposited with deposition rate of 0.1 - 0.2 Å s⁻¹ at different substrate temperatures (T_{sub} ; room temperature, 50, 70, and 90 °C), under a vacuum of 7×10^{-7} Torr. As source and drain electrodes, 50 nm thick Au was thermally deposited with deposition rate of 0.2 - 0.3 Å s⁻¹.

For the spin-coated OFET device fabrication, the same substrate preparation procedure as VD device was performed, and ODTS was treated also. Four IDID derivatives were dissolved in chloroform (0.2~0.3 wt%), and spin-coated at 1500~3000 rpm for 1 minute at ambient condition; then the substrates were passed into nitrogen filled glove box. Source and drain electrode were thermally deposited at same condition as VD device fabrication.

The $I-V$ characteristics of all the OFETs were measured in a nitrogen-filled glove box, using a Keithley 4200 SCS instrument connected to a probe station. All OFET characteristics were obtained from the transfer curve in the saturated regime. For the charge carrier mobility calculations, we checked the channel width and length of the individual devices using an optical microscope.

2.3. Results and Discussion

2.3.1 Design and Synthesis

For the efficient π -conjugation extension of IDID core while keeping its linear aromatic backbone structure, four different IDID derivatives shown in **Scheme 2-1** were designed and synthesized. 2,7-Dibromo-*N,N*-dihexyl-IDID as a common intermediate compound was synthesized by alkylation of 2,7-dibromo-5,10-dihydro-IDID (compound 7 in **Scheme 2-1**). Although the synthesis route to 2,7-dibromo-5,10-dihydro-IDID was previously reported by Cheng group (7 steps with 4.5% overall yield),^[23] I could develop my own route for the more efficient core synthesis, on the basis of selective reactivity of Sonogashira coupling reaction (6 steps with 20.7% overall yield, **Scheme 2-1**).^[26] For two *N*-positions of 2,7-dibromo-5,10-dihydro-IDID, relatively short linear alkyl (n-hexyl) group was adopted to provide solubility for

final materials, which minimized spatial interruption for the efficient intermolecular stacking interaction. To satisfy the conditions for developing high-performing and versatile processable organic semiconductors based on 2,7-dibromo-*N,N*-dihexyl-IDID (**Scheme 2-1**), two most intriguing functionalities were introduced i.e. thiophene and additional aliphatic side chains (different from *N*-hexyl unit), to simultaneously enhance charge carrier transport and solution processability. Beside the solubility enhancement effect, this long-axis parallel aliphatic units at 5-position of substituted thiophenes, additionally give rise to intermolecular van der Waals interaction, which would render a favorable stacking structure for electronics applications, *vide infra*. By systematically modulating these two structural motifs, I have designed and synthesized series of four IDID derivatives, 2H2TIDID, 4H2TIDID, 2H4TIDID, and 4H4TIDID, by Stille coupling and Suzuki-Miyaura coupling methods. These newly synthesized molecules were carefully characterized by ^1H NMR, ^{13}C NMR, elemental analysis (EA), and mass analysis. Detailed synthetic procedures are described in **Scheme 2-1**,

Experimental Section.

IDID derivatives were crystallized in different types of crystal habit (hexagonal for 2H2TIDID, acicular for 2H4TIDID, and fibrous for 4H2TIDID and 4H4TIDID) from both final purification process (by recrystallization method) and single-crystal growth (by solution crystallization method). Noteworthily, those crystalline solids exhibited superior solubility in common organic solvents. Following order of increasing solubility was observed in chloroform solvent: 2H4TIDID (2 wt.%) < 2H2TIDID (10

wt.%) < 4H4TIDID (> 20 wt.%) < 4H2TIDID (> 40 wt.%). As was expected from our molecular design rationale, additional aliphatic side chains gave rise to the versatile processability with high enough solubility. Different crystal habits are considered to originate from different molecular stacking as will be discussed later.

2.3.2. Theoretical, Optical, and Electrochemical Properties

To investigate basic electronic characteristics of the four IDID derivatives, evaluation of their optical and electrochemical properties were carried out by UV-Vis absorption and cyclic voltammetry (CV) studies, as summarized in **Table 2-1**. UV-Vis spectra of the solution state samples (**Figure 2-1a**) reveal that the lowest energy transition, corresponding to the $\pi-\pi^*$ transition with strong oscillator strength for all derivatives, is clearly red shifted for the molecules with larger number of thiophene units. The density functional theory (DFT) calculation results (Gaussian 09 package, basis set: B3LYP-6-31G d p (**Figure 2-1c**) are also consistent with experimental results; electron density of the frontier molecular orbitals are delocalized over the entire aromatic backbone including the thiophene units to give smaller band gap.^[27] When changed from solution to solid state, absorption spectra of $\pi-\pi^*$ transition bands of all the IDID derivatives showed 50-60 nm bathochromic shifts with clearly resolved vibronic peaks (**Figure 2-1b**). Such stacking-induced vibronic progression is attributed to the formation of highly

ordered crystalline structures, which should be based on the back-bone planarization and tight stacking in the solid state.^[20]

The highest occupied molecular orbital (HOMO) energies in solution states of four IDID derivatives were evaluated from the first oxidation onset of solution CV (around -4.9 eV in methylene chloride solution for all derivatives, see **Figure 2-2**). The DFT calculation results suggest that gas phases of the four IDID derivatives render similar HOMO values insignificantly different from each other as experimentally obtained ones do (see **Table 2-1**). However, it is noted that, according to the limitation of the B3LYP functional, calculated HOMO levels were over-estimated by ~0.3 eV. In the solid state, however, HOMO levels of all compounds were stabilized in their solid states as shown in the Table 2-1. It is noteworthy that the HOMO levels of IDID derivatives comprising longer π -conjugated backbone with four thiophene groups were more stabilized (i.e., 2H4TIDID: 0.35 eV, and 4H4TIDID: 0.34 eV) than others comprising shorter π -conjugated backbone with two thiophene groups (i.e., 2H2TIDID: 0.11 eV, and 4H2TIDID: 0.16 eV). It is speculated that the chemical linkage between or to the thiophene groups are subjected to the planarization in the solid state giving rise to the larger stabilization in the case of the compounds with larger number of thiophene rings. Because of large proportion of pyrrole rings in fused-backbone, IDID derivatives exhibit slightly high lying HOMO energy level than those of other fused pyrrole-containing heteroacene organic semiconductors (e.g. those of five ring fused IC-derivatives vary from 5.3 eV to 5.6 eV)^[20, 21]. It should be importantly noted that

such higher HOMO levels of IDID derivatives would better match the work function of a gold electrode (5.1 eV).

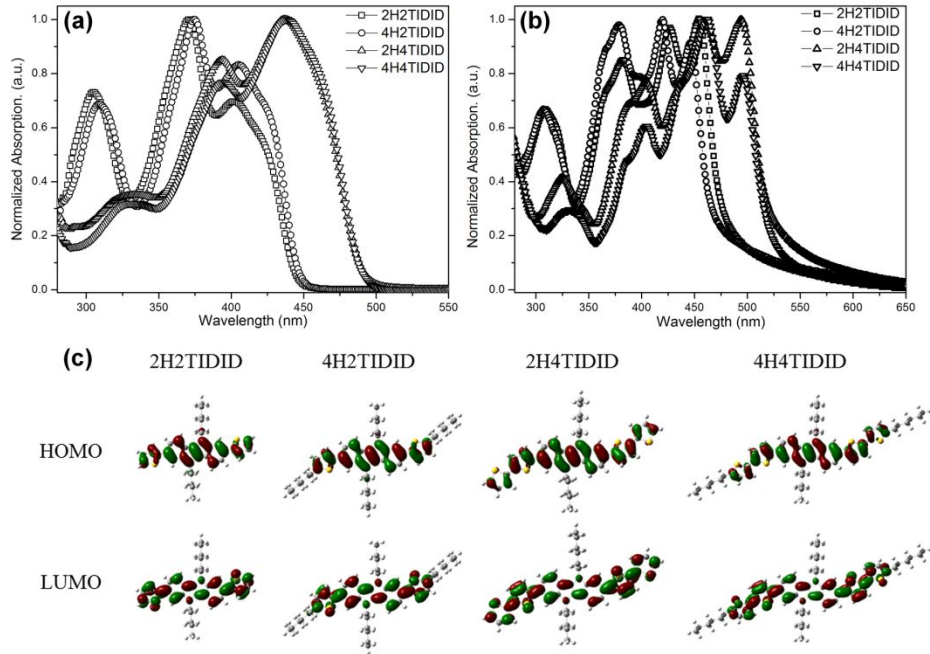


Figure 2-1. Optical and theoretical characteristics of IDID derivatives. (a) solution absorption spectra; (b) film absorption spectra; (c) calculated frontier molecular orbitals.

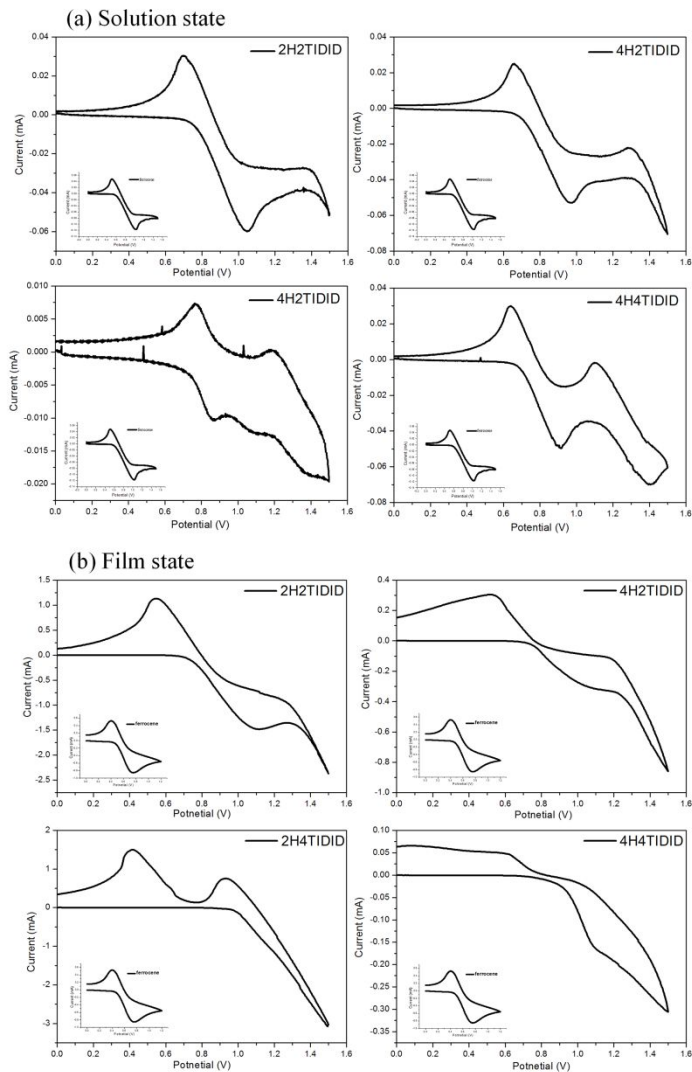


Figure 2-2. Cyclic voltammograms (CVs) of IDID derivatives. (a) solution samples were prepared 5×10^{-3} M solution in methylene chloride; (b) film samples were prepared on ITO patterned glass by drop-casting method (Inset: CV of ferrocene).

Table 2-1. Optical and electrochemical properties of IDID derivatives.

Compound	Abs. _{sol.} [nm] ^{a)}	Abs. _{film} [nm] ^{b)}	HOMO _{cal/sol/film} [eV] ^{c)}	LUMO _{film} [eV] ^{d)}	E _g [eV] ^{e)}
2H2TIDID	305, 371, 401	382, 426, 454	-4.6/-4.95/- 5.06	-2.46	2.6
4H2TIDID	308, 373, 404	378, 420, 446	-4.5/-4.90/- 5.06	-2.46	2.6
2H4TIDID	331, 393, 436	404, 460, 494	-4.6/-4.95/- 5.30	-2.90	2.4
4H4TIDID	332, 395, 439	405, 462, 496	-4.5/-4.90/- 5.24	-2.84	2.4

^{a)} Solution absorption measured in THF with concentration of 1×10^{-5} M; ^{b)} Film absorption measured with spin-coated sample prepared by using 0.5 wt% chloroform solution; ^{c)} Experimental value of HOMO energy level was determined by cyclic voltammetry. Solution sample was prepared 5×10^{-3} M solution in methylene chloride and film sample was prepared on ITO patterned glass by drop-casting method; ^{d)} LUMO = HOMO - E_g; ^{e)} band gaps were estimated from the optical band in film state.

2.3.3. VD OFET Characteristics

To evaluate the charge transporting characteristics of newly synthesized IDID derivatives, I fabricated and examined bottom-gate top-contact (BGTC) VD polycrystalline OFETs devices. All devices were fabricated using the octadecyltrichlorosilane (ODTS) treated SiO_2/Si substrates and their performance was optimized by altering substrate temperature (T_{sub}) during VD process, see **Figure 2-3** and **Table 2-2**. As we expected, the number of thiophene and alkyl substitution indeed gave rise to the significant control of transistor mobility. While IDID derivatives containing two thiophene rings, 2H2TIDID and 4H2TIDID, exhibited average mobility values of $3.0 \times 10^{-2} \text{ cm}^2 \text{ V}^{-1} \text{ s}^{-1}$ and $2.9 \times 10^{-2} \text{ cm}^2 \text{ V}^{-1} \text{ s}^{-1}$, respectively; those containing two bithiophene rings, 2H4TIDID and 4H4TIDID, showed one order of magnitude higher values ($2.7 \times 10^{-1} \text{ cm}^2 \text{ V}^{-1} \text{ s}^{-1}$ and $8.2 \times 10^{-1} \text{ cm}^2 \text{ V}^{-1} \text{ s}^{-1}$, respectively). Moreover, it was also noted that IDID derivatives with additional long-axis parallel alkyl units showed higher mobility values compared to those without parallel alkyl units; i.e. 4H2TIDID and 4H4TIDID exhibited two-fold and three-fold higher hole mobility than those of 2H2TIDID and 2H4TIDID in terms of the highest mobility values, respectively.^[28] It is noteworthy that aliphatic side chains along long-axis direction do not hamper charge carrier transport, while providing largely increased solubility and mobility. The latter is due to the beneficial structural organization for

OFET performance as will be discussed below. Among these IDID derivatives, 4H4TIDID exhibited the highest hole mobility of $9.7 \times 10^{-1} \text{ cm}^2 \text{ V}^{-1} \text{ s}^{-1}$, with threshold voltage of -12V and on/off ratio of 1.6×10^5 . Furthermore, the 4H4TIDID OFET device exhibited moderately stable performance in ambient condition (temperature of 15°C and relative humidity of 28%). We could observe only slight decrease (5.7%) of the field-effect mobility over 24 hours, see **Figure 2-4**.

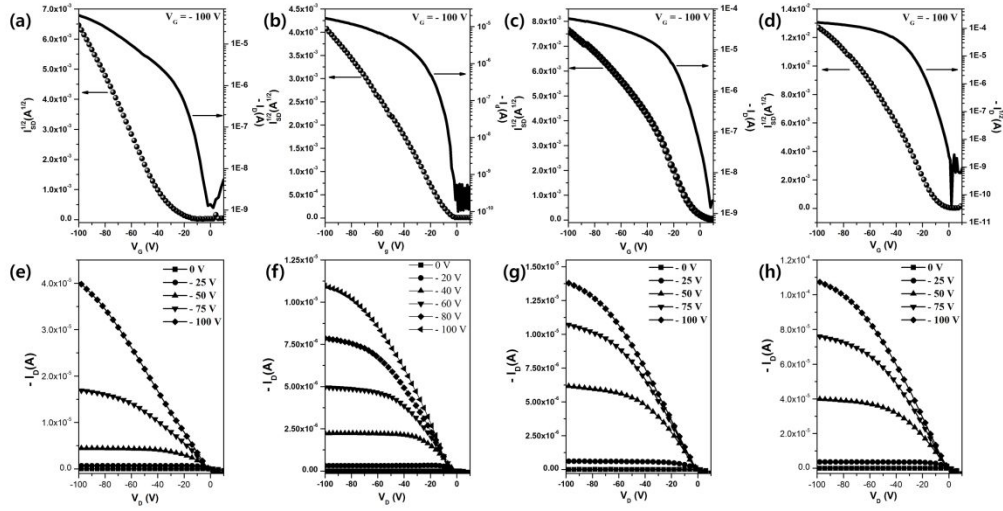


Figure 2-3. Transfer curves and output curves of VD OFETs base on IDID derivatives, respectively. (a), (e) for 2H2TIDID; (b), (f) for 4H2TIDID; (c), (g) for 2H4TIDID; (d), (h) for 4H4TIDID.

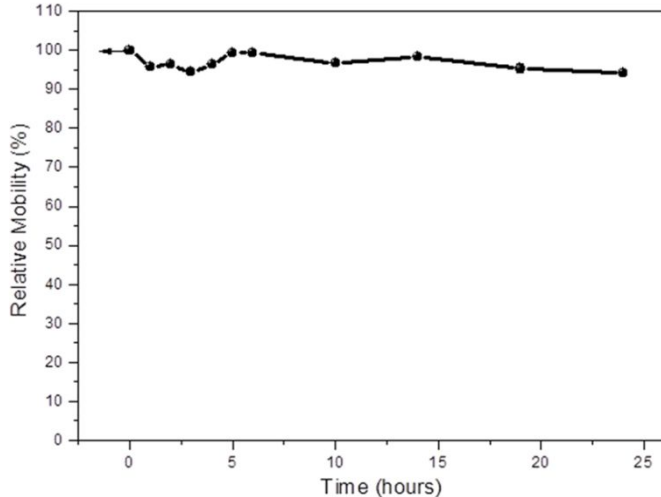


Figure 2-4. Mobility evolution diagram for 4H4TIDID OFET device in ambient condition (temperature of 15 °C and relative humidity of 28%).

Table 2-2. Field-effect transistor characteristics of IDID derivatives.

Compound	$T_{\text{sub}}^{\text{a)}$	$\mu_h [\text{cm}^2\text{V}^{-1}\text{s}^{-1}]^{\text{b)}$	$V_{\text{th}} [\text{V}]^{\text{c)}$	on/off
2H2TIDID	rt	$5.2 \times 10^{-3} / 5.2 \times 10^{-3}$	- 4 ± 3	$\sim 10^3$
	50 °C	$1.4 \times 10^{-2} / 1.8 \times 10^{-2}$	- 5 ± 6	$\sim 10^4$
	70 °C	$3.0 \times 10^{-2} / 3.2 \times 10^{-2}$	- 11 ± 2	$\sim 10^4$
	90 °C	$1.4 \times 10^{-3} / 1.6 \times 10^{-3}$	- 6 ± 5	$\sim 10^4$
4H2TIDID	rt	$2.1 \times 10^{-2} / 3.4 \times 10^{-2}$	- 4 ± 5	$\sim 10^4$
	50 °C	$2.9 \times 10^{-2} / 5.1 \times 10^{-2}$	- 5 ± 2	$\sim 10^5$
	70 °C	$1.8 \times 10^{-2} / 2.6 \times 10^{-2}$	- 2 ± 3	$\sim 10^5$
	90 °C	$6.0 \times 10^{-3} / 9.5 \times 10^{-3}$	- 7 ± 5	$\sim 10^3$
2H4TIDID	rt	$3.1 \times 10^{-2} / 5.2 \times 10^{-2}$	- 10 ± 5	$\sim 10^4$
	50 °C	$2.7 \times 10^{-1} / 3.4 \times 10^{-1}$	- 10 ± 5	$\sim 10^5$
	70 °C	$1.9 \times 10^{-1} / 2.3 \times 10^{-1}$	- 15 ± 3	$\sim 10^5$
	90 °C	$1.6 \times 10^{-1} / 3.4 \times 10^{-1}$	- 12 ± 3	$\sim 10^5$
4H4TIDID	rt	$5.0 \times 10^{-2} / 6.5 \times 10^{-2}$	- 13 ± 3	$\sim 10^6$
	50 °C	$8.2 \times 10^{-1} / 9.7 \times 10^{-1}$	- 12 ± 5	$\sim 10^5$
	70 °C	$7.2 \times 10^{-1} / 8.9 \times 10^{-1}$	- 11 ± 5	$\sim 10^4$
	90 °C	$2.8 \times 10^{-1} / 3.7 \times 10^{-1}$	- 12 ± 5	$\sim 10^5$
4H4TIDID ^{d)}	rt	$1.2 \times 10^{-1} / 1.8 \times 10^{-1}$	- 10 ± 3	$\sim 10^5$

^{a)} Substrate temperature in vacuum deposition; ^{b)} Field-effect transistor mobility, average / maximum (average values are calculated with 10 devices); ^{c)} Threshold voltage; ^{d)} Solution-processed device.

2.3.4. Structural Analyses

Since the molecular packing structures including the geometry of interacting structural motifs are crucial for comprehending charge transport properties of given solid states, we tried to investigate molecular arrangements of the IDID derivatives *via* single-crystal X-ray diffraction (SC-XRD) and 2D grazing incidence X-ray diffraction (2D-GIXD) analyses. 2H2TIDID was found to show herringbone-type stacking similar to other fused pyrrole-containing organic semiconductors like IC^[15, 19, 20, 22] (see **Figure 2-5 and Table 2-3** for SC-XRD of 2H2TIDID). Unfortunately, however, SC-XRD of the other three compounds could not be conducted due to the insufficient size of the single crystals. In this regard, I tried to correlate chemical structures of IDID derivatives with their packing structures by analyzing 2D-GIXD patterns of VD films. As shown in **Figure 2-6**, 2D-GIXD result of 2H2TIDID exhibits indistinct Bragg spots and radial hollow patterns, most likely due to the conformation induced polymorphic characteristic. By increasing the number of thiophene substitution, meanwhile, the Bragg spots of 2H4TIDID becomes much clear and distinctive, as is normally observed for the three-dimensionally ordered polycrystalline film. On the other hand, diffraction patterns of IDID derivatives containing additional two aliphatic chains, i.e. 4H2TIDID and 4H4TIDID, exhibit strong and distinct Bragg rods (q_{xy} of 0.568, 1.1385, 1.258, 1.371, 1.548, and 1.733 Å⁻¹ for 4H2TIDID, q_{xy} of 0.550, 1.111, 1.265, 1.515, 1.637,

and 1.860 \AA^{-1} for 4H4TIDID); clearly revealing lack of restriction on the q_z -component by forming 2D crystalline layers.^[29-32] By correlating molecular lengths (along molecular long axis direction, by optimized geometry) and d_{00l} -spacing values extracted from q_z line-cut profile of 2D-GIXD, I could deduce that all the IDID molecules are obliquely oriented toward out-of-plane direction (see **Figure 2-7, Table 2-4**, and **Figure 2-6 e** for hypothetical molecular orientation). Although I could not extract actual in-plane stacking geometry from this 2D-GIXD pattern, I wanted to illustrate the most probable stacking geometry (**Figure 2-6 e**) using the SC-XRD structure of 2H2TIDID which showed slipped herringbone stacking. When additional long-axis alkyl chains are introduced, most intriguingly, in-plane 2D intermolecular interactions are engendered as evidenced by the Bragg rods in case of 4H2TIDID and 4H4TIDID (**Figure 2-6**).^[29-32] Such dramatic structural deviation in the latter indeed reflects huge enhancement in OFET performance, suggesting advantages of 2D intermolecular interaction network.

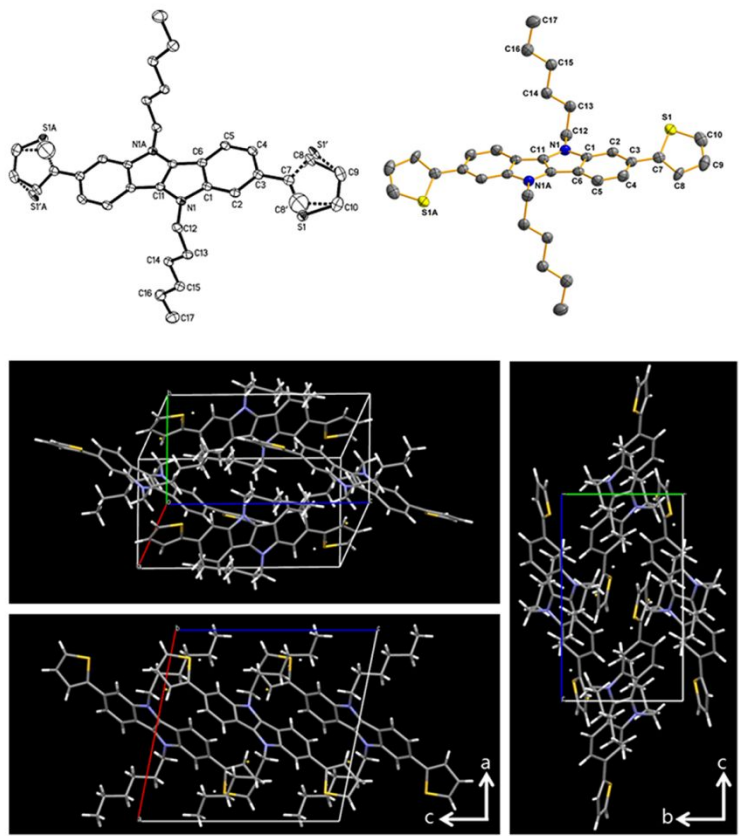


Figure 2-5. Single crystal structure of 2H2TIDID.

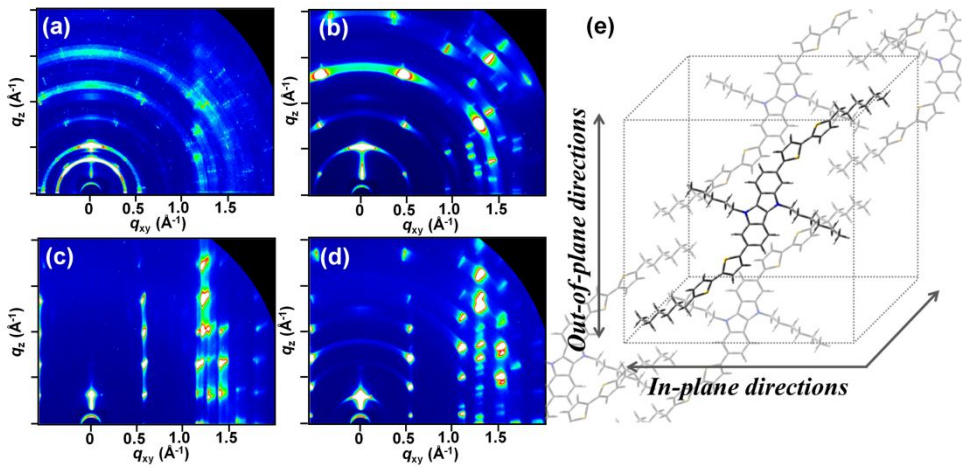


Figure 2-6. 2D-GIXD patterns of vacuum deposited samples ((a) 2H2TIDID; (b) 2H4TIDID; (c) 4H2TIDID; (d) 4H4TIDID), and schematic diagram of 4H4TIDID supramolecular structure ((e), The in-plane molecular orientation in this figure is an illustration of hypothetically constructed slipped herringbone stacking based on the SC-XRD result of 2H2TIDID).

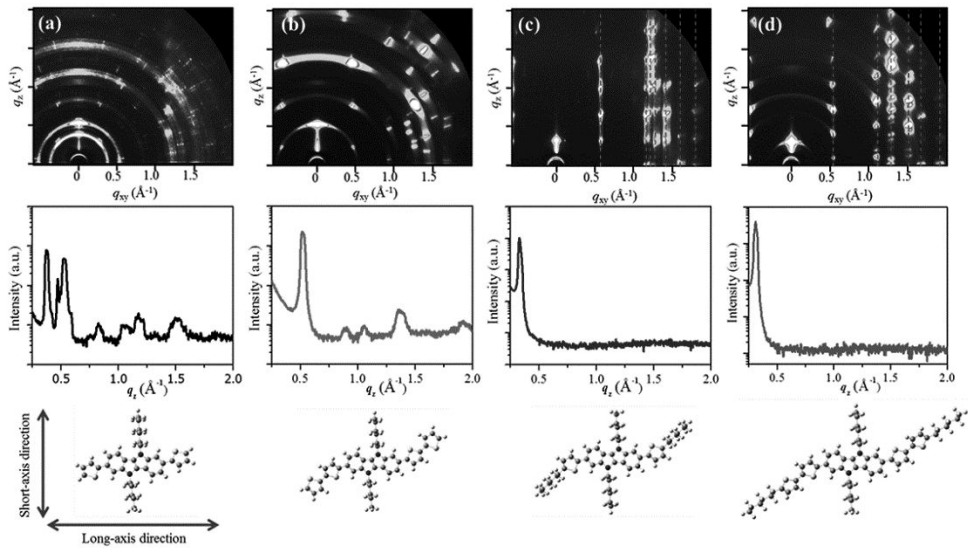


Figure 2-7. 2D-GIXD diffraction images of IDID derivatives VD films and corresponds q_z line-cut profiles. (a) 2H2TIDID; (b) 2H4TIDID; (c) 4H2TIDID; (d) 4H4TIDID.

Table 2-3. Crystal data and structure refinement for 2H2TIDID.

Empirical formula	C17 H19 N S
Formula weight	269.39
Temperature	173(2) K
Wavelength	0.71073 Å
Crystal system	Monoclinic
Space group	P2(1)/c
Unit cell dimensions	a = 13.4671(4) Å b = 7.9608(2) Å c = 13.9086(4) Å
Volume	1462.44(7) Å ³
Z	2
Density (calculated)	0.612 Mg/m ³
Absorption coefficient	0.104 mm ⁻¹
F(000)	288
Crystal size	0.42 x 0.32 x 0.20 mm ³
Theta range for data collection	1.54 to 26.00°.
Index ranges	-16<=h<=16, -9<=k<=8, -17<=l<=17
Reflections collected	12173
Independent reflections	2876 [R(int) = 0.0459]
Completeness to theta = 26.00°	99.9 %
Absorption correction	Multi-scan
Max. and min. transmission	0.9799 and 0.9574
Refinement method	Full-matrix least-squares on F ²
Data / restraints / parameters	2876 / 0 / 172
Goodness-of-fit on F ²	1.050
Final R indices [I>2sigma(I)]	R1 = 0.0865, wR2 = 0.2730
R indices (all data)	R1 = 0.0961, wR2 = 0.2857
Largest diff. peak and hole	1.396 and -0.787 e.Å ⁻³

Table 2-4. Summary of correlation result between 2D-GIXD and DFT calculation.

	2H2TIDID	2H4TIDID	4H2TIDID	4H4TIDID
q_z (\AA^{-1}) value/ d -spacing (\AA)	0.3720/16.9	0.5180/12.1	0.3291/19.1	0.3069/20.5
Molecular long-axis length (\AA) ^(a)	18.1 (18.3)	25.8 (16.4)	30.8 (18.4)	38.8 (18.3)
Tilt angle ($^\circ$) ^(b)	69.0	27.9	38.3	31.9

^(a) Molecular length was extracted from geometry optimization result from DFT calculation. Parenthesis values are length for short-axis direction of conjugated back-bone. ^(b) Tilt angle was calculated from d -spacing value and correspond molecular long-axis length

2.3.5. Solution-Processed OFET Characteristics

Consistent with my molecular design rationale, 4H4TIDID exhibits superior solubility in conventional organic solvents (e.g. > 20 wt.% for chloroform). Based on such remarkable solubility and excellent field-effect mobility of 4H4TIDID, I wanted to fabricate solution-processed OFET device, see **Experimental Section** for detailed procedures. Spin-coated OFET devices based on 4H4TIDID exhibited noteworthy device performance (e.g. mobility value up to $1.8 \times 10^{-1} \text{ cm}^2 \text{ V}^{-1} \text{ s}^{-1}$), see **Figure 2-8** and **Table 2-2**. While showing similar threshold voltage as well as on/off ratio, it should be mentioned that the mobility value of spin-coated devices are somewhat lower compared to that of VD device. This can be rationalized by topographic characteristics, as shown in **Figure 2-9**. Even though 4H4TIDID exhibits noteworthy solubility as well as facile solution processability, significant increase in pinhole density is observed, which must have caused an underestimation of extracted mobility. This can be also comprehended by comparing device characteristic between spin-coated and VD device ($T_{\text{sub}} = 90 \text{ }^\circ\text{C}$), which show similar topological characters and comparable mobility values. This reasonably high performance from spin-coated device can be rationalized from 2D-GIXD result. The 2D-GIXD diffraction pattern of spin-coated device shows exactly the same diffraction pattern of the VD sample (**Figure 2-8 c and d**). From these results, it is deduced that 4H4TIDID molecules

assemble into the exactly same hierarchical structure irrespective of the fabrication methods. It should also be noted that the spin-coated devices do not require any additional post treatment, such as thermal annealing or solvent vapor annealing. This superior assembling nature can be attributed to the well-organized secondary interaction networks; hence, the molecules can readily interact to construct 2D ordered domains during (vacuum-/solution-) deposition procedures.

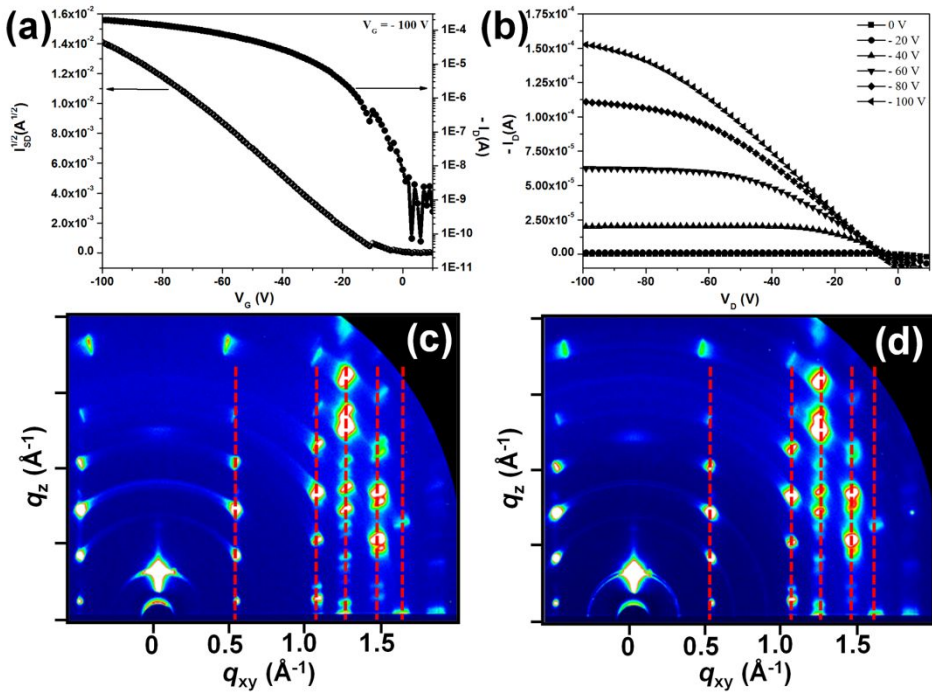


Figure 2-8. Transfer curve (a) and output curve (b) of 4H4TIDID spin-coated OFET device, and 2D-GIXD patterns of 4H4TIDID vacuum deposited film (c) and spin-casted film (d).

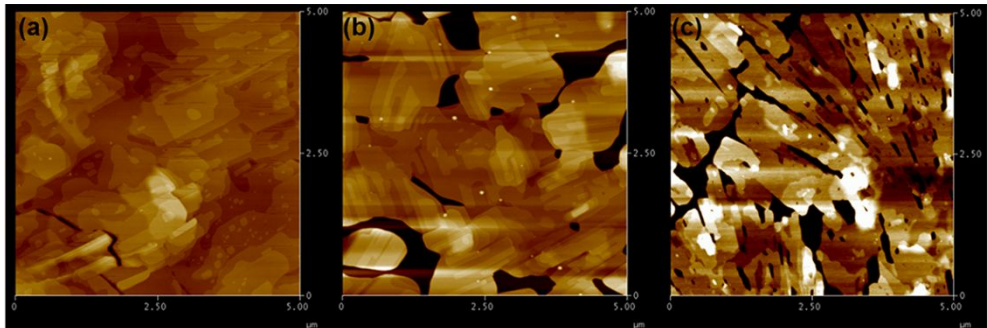


Figure 2-9. Atomic force microscope height images of 4H4TIDID on OFET devices. (a) T_{sub} 50°C VD device; (b): T_{sub} 90°C VD device; (c) Spin-coated device.

2.4. Conclusion

I have designed and synthesized a series of IDID-based semiconducting materials by systematic substitution of aromatic and aliphatic functional units to realize new class of versatile processable p-type organic semiconductors for OFETs applications. Among newly synthesized four IDID derivatives, 4H4TIDID exhibited excellent p-type OFET characteristic with highest hole mobility up to $9.7 \times 10^{-1} \text{ cm}^2 \text{ V}^{-1} \text{ s}^{-1}$ from VD device and $1.8 \times 10^{-1} \text{ cm}^2 \text{ V}^{-1} \text{ s}^{-1}$ from spin-coated device. Based on the systematic structure-property correlation, it was found that the long-axis parallel aliphatic units give rise to the enhancement of solubility as well as charge transport property; the latter is attributed to the two-dimensional surface parallel intermolecular interaction network. In this work, I could successfully demonstrate the high potential of IDID core as an organic semiconductor backbone, and also propose molecular design strategy to realize high-performance and versatile processable IDID semiconductor.

2.5. Reference

- [1] A. Tsumura, H. Koezuka, T. Ando, *Appl. Phys. Lett.* **1986**, *49*, 1210
- [2] Y. Diao, B. C-K. Tee, G. Giri, J. Xu, D. W. Kim, H. A. Recerril, R. M. Stoltenberg, T. H. Lee, G. Xue, S. C. B. Mannsfeld, Z. Bao, *Nat. Mater.* **2013**, *12*, 665
- [3] H. T. Yi, M. M. Payne, J. E. Anthony, V. Podzorov, *Nat. Commun.* **2012**, *3*, 1259
- [4] C. Wang, H. Dong, W. Hu, Y. Liu, D. Zhu, *Chem. Rev.* **2012**, *112*, 2208.
- [5] A. R. Murphy, J. M. J. Fréchet, *Chem. Rev.* **2007**, *107*, 1066.
- [6] V. Coropceanu, J. Cornil, D. A. S. Filho, Y. Olivier, R. Silbey, J. L. Brédas, *Chem. Rev.* **2007**, *107*, 926.
- [7] Q. Meng, H. Dong, W. Hu, D. Zhu, *J. Mater. Chem.* **2011**, *21*, 11708.
- [8] W. Zhang, Y. Liu, G. Yu, *Adv. Mater.* **2014**, *26*, 6898.
- [9] K. Takimiya, S. Shinamura, I. Osaka, E. Miyazaki, *Adv. Mater.* **2011**, *11*, 4347.
- [10] T. Minari, C. Liu, M. Kano, K. Tsukagoshi, *Adv. Mater.* **2012**, *24*, 299.
- [11] G. Schweicher, V. Lemaur, C. Nievel, C. Ruzié, Y. Diao, O. Goto, W. Y. Lee, Y. Kim, J. B. Arlin, J. Karpinska, A. R. Kennedy, S. R. Parkin, Y. Olivier, S. C. B. Mannsfeld, J. Cornil, Y. H. Geerts, Z. Bao, *Adv. Mater.* **2015**, *27*, 3066.

- [12] H. Minemawari, T. Yamada, H. Matsui, J. Tsutsumi, S. Haas, R. Chiba, R. Kumai, T. Hasegawa, *Nature*. **2011**, *475*, 364.
- [13] J. Soeda, Y. Hirose, M. Yamagishi, A. Nakao, T. Uemura, K. Nakayama, M. Uno, Y. Nakazawa, K. Takimiya, J. Takeya, *Adv. Mater.* **2011**, *23*, 3309.
- [14] Y. Yuan, G. Giri, A. L. Ayzner, A. P. Zombeck, S. C. B. Mannsfeld, J. Chen, D. Nordlund, M. F. Toney, J. Huang, Z. Bao, *Nat. Commun.* **2014**, *5*, 3005.
- [15] T. V. Pho, J. D. Yuen, J. A. Kurzman, B. G. Smith, M. Miao, W. T. Walker, R. Seshadri, F. Wudl, *J. Am. Chem. Soc.* **2012**, *134*, 18185.
- [16] Y. Wu, Y. Li, S. Gardner, B. S. Ong, *J. Am. Chem.* **2005**, *127*, 614.
- [17] J. F. Morin, N. Drolet, Y. Tao, M. Leclerc, *Chem. Mater.* **2004**, *16*, 4619.
- [18] N. Drolet, J. F. Morin, N. Leclerc, S. Wakim, Y. Tao, M. Leclerc, *Adv. Funct. Mater.* **2005**, *15*, 1671.
- [19] H. Jiang, H. Zhao, K. K. Zhang, X. Chen, C. Kloc, W. Hu, *Adv. Mater.* **2012**, *23*, 5075.
- [20] P. L. T. Boudreault, S. Wakim, N. Blouin, M. Simard, C. Tessier, Y. Tao, M. Leclerc, *J. Am. Chem. Soc.* **2007**, *129*, 9125.
- [21] P. L. T. Boudreault, S. Wakim, M. L. Tang, Y. Tao, Z. Bao, M. Leclerc, *J. Mater. Chem.* **2009**, *19*, 2921.
- [22] G. Zhao, H. Dong, H. Zhao, L. Jiang, X. Zhang, J. Tan, Q. Meng, W. Hu, *J. Mater. Chem.* **2012**, *22*, 4409.

- [23] Y. Y. Lai, J. M. Yeh, C. E. Tsai, Y. J. Cheng. *Eur. J. Org. Chem.* **2013**, 23, 5076.
- [24] Z. R. Owczarczyk, W. A. Braunecker, A. Garcia, R. Larsen, A. M. Nardes, N. Kopidakis, D. S. Ginley, D. C. Olson, *Macromolecules* **2013**, 46, 1350.
- [25] L. Qiu, C. Yu, N. Zhao, W. Chen, Y. Guo, X. Wan, R. Yang, Y. Liu, *Chem. Commun.* **2012**, 48, 12225.
- [26] T. Hundermark, A. F. Littke, S. L. Buchwald, G. C. Fu, *Org. Lett.* **2000**, 2, 1729.
- [27] S. I. Kato, S. Shimizu, H. Taguchi, A. Kobayashi, S. Nakamura, *J. Org. Chem.* **2012**, 77, 3223.
- [28] In case of 4H2TIDID devices, it should be noted that charge transporting layers were partially disconnected during gold electrode depositions, probably by large expansion/contraction ratio by thermal energy; consequently, average mobility value should be underestimated and cannot be compared directly.
- [29] I. Kuzmenko, H. Rapaport, K. Kjaer, J. A. Nielsen, I. Weissbuch, M. Lahav, L. Leiserowitz, *Chem. Rev.* **2001**, 101, 1659.
- [30] Z. Bao, J. Lockion *Organic Field-Effect Transistors*, CRC Press, New York, NY, USA **2007**
- [31] J. Als-Nielsen, D. Jacquemain, K. Kjaer, F. Leveiller, M. Lahav, L. Leiserowitz, *Phys. Rep.* **1994**, 246, 251
- [32] H. Yang, S. H. Kim, L. Yang, S. Y. Yang, C. E. Park, *Adv. Mater.* **2007**, 19,

2868

Chapter 3.

Dicyanovinyl-Substituted Indolo[3,2-b]indole Derivatives: Low Band-Gap π-Conjugated Molecules for Single-Component Ambipolar Organic Field-Effect Transistor

3.1. Introduction

Research interests in the ambipolar organic field-effect transistors (OFETs) have been significantly grown because of their potential application to the complementary circuits like inverters without complicated multi-step deposition process.^[1-2] Especially, single-component ambipolar OFETs simply comprised of a single-layer active channel with symmetric source-drain electrodes, have attracted much attention owing to their expediency in practical device fabrication.^[2-4] Theoretically, many of organic semiconductors are known to transport both types of charge carriers in their solid-state, if and only if charge carriers are efficiently injected.^[2,5] However, majority of reported organic semiconductors exhibited unipolar characteristics, i.e., either hole- or electron-transport only depending on the work function of the electrodes, mainly due to the restriction of high injection barrier for one of the carriers.^[6-8] Therefore, among various crucial issues in realizing single-component ambipolar OFETs, balanced energy level

alignment of the highest occupied molecular orbital (HOMO) and lowest unoccupied molecular orbital (LUMO) of the organic semiconductor relative to the work function of symmetric electrode is most essential for the favorable bipolar injection.^[2, 8-11] In this regard, wide ranges of low band-gap organic materials have been extensively investigated, and some of π -conjugated structures, such as TIPS-pentacenes,^[12-14] diketopyrrolopyrroles,^[15-18] indigos,^[19] isoindigos,^[20] and quinoinal oligothiophenes,^[21-23] have been reported as promising backbone structures for designing high performance ambipolar semiconductor, through appropriate molecular structure engineering.^[24] In spite of such extensive materials research on ambipolar OSCs, molecular structural effect on the operating mechanism of ambipolar OFETs has seldom been explored. In this regard, exploring structure-property correlation based on the comprehensive photophysical, electrochemical, and quantum-chemical calculation studies is essential in developing high performance organic semiconductors.

In Chapter 2, I could demonstrate that indolo[3,2-b]indole (IDID) derivatives are promising p-type organic semiconductors with remarkable hole mobility of $0.97 \text{ cm}^2 \text{ V}^{-1} \text{ s}^{-1}$ and versatile processability.^[25] Besides apparent advantages of pyrrole-fused structure such as facile solubility control and structural derivatization, IDID core is characterized by stronger electron donating nature than those of other reported pyrrole-fused heteroarene cores (e.g., carbazole and indolocarbazole), owing to the larger proportion of five-membered pyrrole units in the backbone. To examine the possible bipolar carrier injection and transport, I herein designed and synthesized intramolecular

charge transfer (ICT)-type IDID derivatives (IDID-DCV derivatives), 2HIDID-DCV, 2H2TIDID-DCV, and 2H4TIDID-DCV, which comprise IDID as an electron donor (D) and dicyanovinyl (DCV) as an electron acceptor (A) with A- π -D- π -A type architecture. Three different π -linking units (none, thiophene, bithiophene) were incorporated to explore different degrees of ICT interaction and π -conjugation, which enabled both molecular structure-property correlation and precise control of electronic characteristics. To elaborate in-depth analysis of structure-property correlation, I also prepared p-type reference molecules, 2HIDID, 2H2TIDID, and 2H4TIDID, with which comprehensive studies were conducted in terms of their theoretical, photophysical, electrochemical, morphological, electrical, and structural characteristics. Among others, 2H2TIDID-DCV (with thiophene π -linker) exhibited dramatically reduced energy band-gap (1.62 eV in solution state) as well as excellent film morphology, which afforded highly balanced ambipolar charge transport with hole and electron mobilities of $0.08 \text{ cm}^2 \text{ V}^{-1} \text{ s}^{-1}$ and $0.09 \text{ cm}^2 \text{ V}^{-1} \text{ s}^{-1}$, respectively, in the vacuum-deposited (VD) OFET devices. Aiming at a solution processable IDID-DCV derivative, OD2TIDID-DCV was also synthesized for which hexyl side chains of 2H2TIDID-DCV were replaced by 2-octyldodecyl group. The spin-coated OFET device of OD2TIDID-DCV also exhibited ambipolar charge transport behavior (mobility of $9.67 \times 10^{-2} \text{ cm}^2 \text{ V}^{-1} \text{ s}^{-1}$ for hole, and $3.43 \times 10^{-3} \text{ cm}^2 \text{ V}^{-1} \text{ s}^{-1}$ for electron). To the best of my knowledge, this is the first report of single-component ambipolar OFET based on pyrrole-fused

heteroacene family even including the widely studied indolocarbazole derivatives.

3.2. Experimental

Synthesis

The final products were synthesized according to the synthetic procedure shown in **Scheme 3-1**. Synthesis of 2,7-dibromo-5,10-dihexyl-5,10-dihydroindolo[3,2-b]indole (2-,7-dibromo-*N,N*-dihexyl-IDID, **1**) was described in **chapter 2**. Unless otherwise stated, all reagents were purchased at Sigma Aldrich, TCI, and Alfa Aeasar.

Synthesis of 5,10-dihexyl-5,10-dihydroindolo[3,2-b]indole-2,7-dicarbaldehyde (**2**).

A 100 mL round bottom flask, equipped with a magnetic stirrer bar, was baked under reduced pressure and backfilled with Ar (for three times). A solution of compound **1** (200 mg, 0.375 mmol) in anhydrous tetrahydrofuran in baked reaction vessel was cool down to -17 °C, afterwards, n-butyllithium (n-BuLi, 1.6 M solution, 0.36 mL, 0.902 mmol) was added slowly. One hour later, dimethylformamide (69 µL, 0.902 mmol) was added to a reaction mixture, and then, reaction vessel was warmed to room temperature. After reaction finished, reaction mixture was quenched with distilled water (200 mL), and organic compounds were extracted with methylene chloride. Combined organic phase was separated and concentrated. Crude product was purified by column chromatography (ethyl acetate (EA)/n-hexane (n-hex); 1:19, v/v) to afford compound **2** as yellow solid. (90 mg, 55.3 %) $^1\text{H-NMR}$ (300 MHz, CDCl_3 , δ): 10.14 (s,

2H), 8.04 (s, 2H), 7.98 (d, J = 8.22 Hz, 2H), 7.74 (d, J = 8.19 Hz, 2H), 4.58 (t, J = 7.14 Hz, 4H), 2.00 (m, J = 7.41 Hz, 4H), 1.44-1.25 (m, 12H), 0.87 (t, J = 7.02 Hz, 6H)

Synthesis of **2HIDID-DCV**.

A mixed solution of **2** (200 mg, 0.462 mmol), malononitrile (67.9 mg, 1.017 mmol), Al₂O₃ (377 mg, 3.698 mmol), and methylene chloride (50 mL) was vigorously stirred for 2 hours at room temperature. After reaction finished, reaction mixture was filtered through celite plug to remove residual Al₂O₃, and filtrate was concentrated under reduced pressure. The crude product was purified by flash column chromatography (THF) and subsequently by recrystallization (ethyl acetate) to afford 2HIDID-DCV as dark purple solid (220 mg, 90.3%). ¹H-NMR (500MHz, Tetrahydrofuran-d8, δ): 8.30 (s, 2H), 8.24 (s, 2H), 8.13 (d, J = 8.5Hz, 2H), 7.86 (d, J = 8.5Hz, 2H), 4.64 (t, J = 7.5Hz, 4H), 2.00 (q, J = 7.5Hz, 4H), 1.43 (q, J = 7.5Hz, 4H), 1.35-1.24 (m, 8H), 0.83 (t, J = 7.5Hz, 6H). ¹³C-NMR (500MHz, Tetrahydrofuran-d8, δ): 161.30, 142.50, 131.37, 127.80, 121.68, 120.41, 117.81, 115.66, 115.08, 115.04, 79.72, 46.40, 32.63, 31.28, 27.77, 23.54, 14.43. HRMS (FAB, m/z) Calcd. for C₃₄H₃₄N₆: 526.28; found: 526.2851. Elel. Anal. Calcd. for C₃₄H₃₄N₆: C 77.54, H 6.51, N 15.96; found: C 77.4905, H 6.5662, N 15.8965.

Synthesis of 5,10-dihexyl-2,7-bis(4,4,5,5-tetramethyl-1,3,2-dioxaborolan-2-yl)-5,10-dihydroindolo[3,2-b]indole (**3**).

A 100 mL round bottom flask, equipped with a magnetic stirrer bar and reflux condenser, was baked under reduced pressure and backfilled with Ar (for three times).

1 (1.00 g, 1.878 mmol), bis(pinacolato)diboron (1.06 g, 4.133 mmol), [1,1'-Bis(diphenylphosphino)ferrocene]-dichloropalladium(II) (345 mg, 0.413 mmol), potassium acetate (1.10 g, 11.271 mmol), and anhydrous dimethylformamide (35mL) were added, then gently refluxed for 24 hours. After reaction finished, reaction mixture was quenched with brine (300 mL), and extracted with methylene chloride. The combined organic phase was dried with MgSO₄ and concentrated under reduced pressure. The crude product was purified by column chromatography (ethyl acetate/n-hex; 1:9, v/v) to afford compound **3** as yellow solid (350 mg, 41%). ¹H-NMR (300 MHz, CDCl₃, δ): 7.93 (s, 2H), 7.84 (d, *J* = 7.86Hz, 2H), 7.62 (d, *J* = 7.86 Hz, 2H), 4.55 (t, *J* = 6.93 Hz, 4H), 1.98 (q, *J* = 6.57 Hz, 4H), 1.39 (s, 24H), 1.29 (m, 12H), 0.86 (t, *J* = 6.72 Hz, 6H)

Synthesis of 5,5'-(5,10-dihexyl-5,10-dihydroindolo[3,2-b]indole-2,7-diyl)bis(thiophene-2-carbaldehyde) (**4**).

3 (205 mg, 0.223 mmol), 5-bromothiophene-2-carbaldehyde (131.3 mg, 0.469 mmol), tetrakis(triphenylphosphine)palladium(0) (37.38 mg, 0.032 mmol), 2N K₂CO₃ aqueous solution (10 mL), and tetrahydrofuran (20 mL) were added into a 100 mL round bottom flask, and the reaction vessel was evacuated and backfilled with Ar. After then, reaction mixture was gently refluxed for 12 hours. After reaction finished, reaction mixture was quenched with 1N HCl aqueous solution (300 mL), and extracted with methylene chloride. The combined organic phase was dried with MgSO₄ and concentrated under reduced pressure. The crude product was purified by flash column

chromatography (ethyl acetate/n-hex; 1:2, v/v) and subsequently by recrystallization (ethyl acetate) to afford compound **4** as red solid (190 mg, 94%) ¹H-NMR (300 MHz, DMSO-d6, δ): 9.91 (s, 2H), 8.13 (s, 2H), 8.07 (d, *J* = 4.05 Hz, 2H), 8.00 (d, *J* = 8.37 Hz, 2H), 7.78 (d, *J* = 3.96 Hz, 2H), 7.58 (d, *J* = 8.40 Hz, 2H), 4.68 (t, *J* = 6.48 Hz, 4H), 1.88 (q, *J* = 6.57 Hz, 4H), 1.23 (m, 12H), 0.81 (t, *J* = 6.57 Hz, 6H)

Synthesis of **2H2TIDID-DCV**.

2H2TIDID-DCV was synthesized by the same synthetic procedure as that for **2HIDID-DCV** by using **4** (166 mg, 0.279 mmol), malononitrile (40.6 mg, 0.615 mmol), Al₂O₃ (0.228 g, 2.535 mmol), and methylene chloride (50 mL). The crude product was purified by flash column chromatography (THF) and subsequently by recrystallization (ethyl acetate) to afford **2H2TIDID-DCV** as dark purple solid (0.189 g, 98%) ¹H-NMR (500MHz, Tetrahydrofuran-d8, δ): 8.23 (s, 2H), 8.01 (d, *J* = 1.5Hz, 2H), 7.98 (d, *J* = 8.5Hz, 2H), 7.86 (d, *J* = 4Hz, 2H), 7.73 (d, *J* = 4Hz, 2H), 7.61 (dd, *J* = 8.5Hz, 1.5Hz, 2H), 4.66 (t, *J* = 7Hz, 4H), 2.00 (q, *J* = 7.5Hz, 4H), 1.45 (q, *J* = 7.5Hz, 4H), 1.38-1.25 (m, 8H), 0.85 (t, *J* = 7.5Hz, 6H). ¹³C-NMR (500MHz, *tetrahydrofuran-d8*, δ): 158.93, 151.96, 142.73, 141.77, 125.19, 119.90, 118.46, 116.19, 115.45, 114.78, 109.18, 45.98, 32.70, 31.35, 27.73, 23.57, 14.46. HRMS (FAB, m/z) Calcd. for C₄₂H₃₈N₆S₂: 690.26; found: 690.2563. Elem. Anal. Calcd. for C₄₂H₃₈N₆S₂: C 73.01, H 5.54, N 12.16, S 9.28; found: C 73.0165, H 5.5255, N 12.1216, S 9.2924..

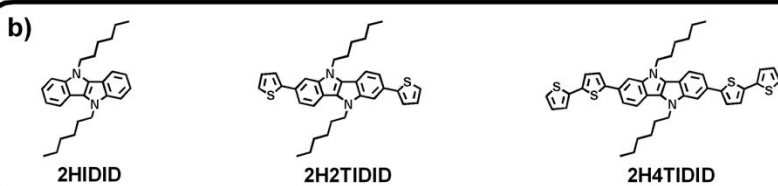
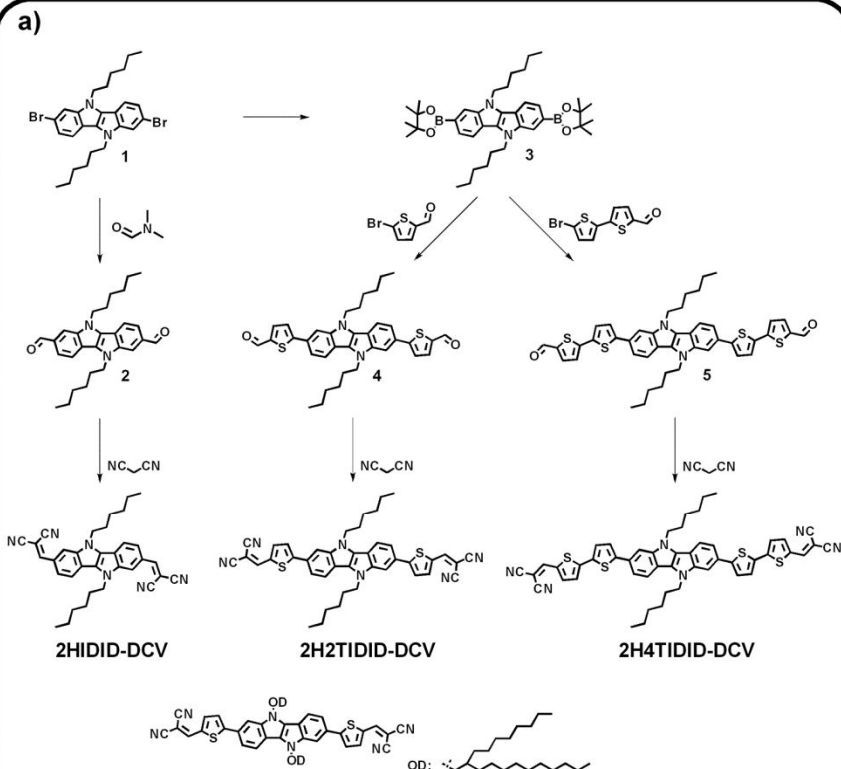
Synthesis of 5',5''-(5,10-dihexyl-5,10-dihydroindolo[3,2-b]indole-2,7-diyl)bis([2,2'-bithiophene]-5-carbaldehyde) (**5**).

Compound **5** was synthesized by the same synthetic procedure as that for compound **4** by using the **3** (170 mg, 0.271 mmole), 5'-bromo-[2,2'-bithiophene]-5-carbaldehyde (135 mg, 0.569 mmol), tetrakis(triphenylphosphine)palladium(0) (32 mg, 0.027 mmol), 2N K₂CO₃ aqueous solution (10 mL), and tetrahydrofuran (20 mL). The crude product was purified by column chromatography (chloroform/ethyl acetate/n-hex; 3:1:6, v/v) and subsequently by recrystallization (ethyl acetate) to afford compound **4** as red solid (162 mg, 78%). ¹H-NMR (300 MHz, Tetrahydrofuran-d8, δ): 9.83 (s, 2H), 7.90 (d, *J* = 8.28 Hz, 2H), 7.83 (s, 2H), 7.79 (d, *J* = 3.9 Hz, 2H), 7.48-7.46 (m, 6H), 7.39 (d, *J* = 3.9 Hz, 2H), 4.61 (t, *J* = 6.9 Hz, 4H), 1.98 (q, *J* = 7.47 Hz, 4H), 1.46-1.25 (m, 12H), 0.49 (t, *J* = 7.08 Hz, 6H)

Synthesis of **2H4TIDID-DCV**.

2H4TIDID-DCV was synthesized by the same synthetic procedure as that for **2HIDID-DCV** by using **5** (162 mg, 0.213 mmol), malononitrile (43 mg, 0.640 mmol), Al₂O₃ (0.228 g, 1.921 mmol), and methylene chloride (60 mL). The crude product was purified by flash column chromatography (tetrahydrofuran) and subsequently by recrystallization (tetrahydrofuran) to afford **2H4TIDID-DCV** as black solid (0.110 g, 60%): ¹H-NMR (500MHz, Tetrahydrofuran-d8, δ): 8.14 (s, 2H), 7.90 (d, *J* = 8.5Hz, 2H), 7.84 (s, 2H), 7.78 (d, *J* = 4Hz, 2H), 7.56 (d, *J* = 3.5Hz, 2H), 7.49 (m, 4H), 7.44 (d, *J* = 4Hz, 2H), 4.61(t, *J* = 7Hz, 4H), 2.03 (m, 4H), 1.48 (q, *J* = 7Hz, 4H), 1.39-1.27 (m, 8H) 0.85 (t, *J* = 7Hz, 6H). HRMS (FAB, m/z) Calcd. for C₅₀H₄₂N₆S₄: 854.24; found: 854.2363. Elem. Anal. Calcd. for C₅₀H₄₂N₆S₄: C 70.23, H 4.95, N 9.83, S 15.0; found:

C 69.8566, H 5.0406, N 9.8086, S 15.0143. (I could not obtain ^{13}C NMR data due to insufficient solubility of 2H4TIDID-DCV for common NMR solvents such as CDCl_3 or Tetrahydrofuran-d8.)



Scheme 3-1. a) Synthesis route for IDID-DCV derivatives and their chemical structure; b) Chemical structure of IDID reference derivatives.

Synthesis route to 2HIDID and OD2TIDID-DCV are shown in Scheme 3-2. Unless otherwise stated, all reagents were purchased at Sigma Aldrich, TCI, and Alfa Aeasar.

Synthesis of trimethyl((2-nitrophenyl)ethynyl)silane (**2**): A mixed solution of 1-bromo-2-nitrobenzene (**1**, 4 g, 19.80 mmol), bis(triphenylphosphine)palladium(II)dichloride (0.695 g, 0.99 mmol), copper(I)iodide (0.377 g, 1.98 mmol), and tetrahydrofuran (40 mL) was purged with Ar. After then, trimethylsilylacetylene (1.945 g, 19.80 mmol) and trimethylamine (10mL) was added, and mixed solution was stirred at 50 °C. After 3 hours later, the reaction mixture was filtered through a silica plug and concentrated under reduced pressure. The concentrated filtrate was purified by column chromatography (ethyl acetate/n-hexane 1:9, v/v) to afford **2** as brown oil (3.635 g, 83.7%). ¹H-NMR (300 MHz, CDCl₃, δ): 8.01 (d, *J* = 8.1 Hz, 1H), 7.64 (d, *J* = 7.5 Hz, 1H), 7.53 (t, *J* = 7.5 Hz, 1H), 7.43 (t, *J* = 7.5 Hz, 1H), 0.29 (s, 9H).

Synthesis of 1-ethynyl-2-nitrobenzene (**3**).

A mixed solution of **2** (3.635 g, 16.57 mmol), K₂CO₃ (2.520g 18.23 mmol), methanol (20 mL), and methylene chloride (80 mL) was stirred at room temperature. After 10 hours, the reaction mixture was poured into water (300 mL), and extracted with methylene chloride. The combined organic phase was dried with MgSO₄ and concentrated under reduced pressure. The crude product was purified by flash column chromatography (ethyl acetate/n-hexane 1.5, v/v) to afford compound **3** as a brown powder (1.994 g, 81.8%). ¹H-NMR (300 MHz, CDCl₃, δ): 8.06 (d, *J* = 7.5 Hz, 1H),

7.71 (d, $J = 7.5$ Hz, 1H), 7.60 (t, $J = 7.5$ Hz, 1H), 7.51 (t, $J = 7.5$ Hz, 1H), 3.51 (s, 1H).

Synthesis of 1,2-bis(2-nitrophenyl)ethyne (**4**).

Compound **4** was synthesized by the same synthetic procedure as that for compound **2** by using **3** (1.994 g, 13.55 mmol), **2** (2.738 g, 13.55 mmol), bis(triphenylphosphine)palladium(II)dichloride (0.467 g, 0.68 mmol), copper(I)iodide (0.258 g, 1.35 mmol), and tetrahydrofuran (60 mL). The crude products was purified by flash column chromatography (chloroform) and subsequently by reprecipitation (methanol) to afford the compound **4** as a brown solid (0.861 g, 23.7%). $^1\text{H-NMR}$ (300 MHz, CDCl_3 , δ): 8.15 (d, $J = 8.1$ Hz, 2H), 7.83 (d, $J = 7.5$ Hz, 2H), 7.66 (t, $J = 8.1$ Hz, 2H), 7.54 (t, $J = 7.5$ Hz, 2H).

Synthesis of 1-2-bis(2-nitrophenyl)ethane-1,2-dione (**5**).

A mixed solution of potassium permanganate (1.522 g, 9.630 mmol), Adogen 464 (catalytic amount), distilled H_2O (30 mL), methylene chloride (40 mL), and acetic acid (1.5 mL) was purged with Ar. After then, **4** (0.861 g, 3.210 mmol) was added and gently refluxed for 5 hours, cooled, and decolorized (using NaHSO_3), sequentially. The combined organic phase was dried with MgSO_4 and filtered through a silica plug. The yellow filtrate was concentrated under reduced pressure, and the resulting solid was washed with methanol to afford compound **5** as a dim yellow crystalline solid (1.451 g, 85.2 %). $^1\text{H-NMR}$ (300 MHz, CDCl_3 , δ): 8.30 (d, $J = 7.5$ Hz, 2H), 7.89 (t, $J = 7.5$ Hz, 2H), 7.76 (t, $J = 7.5$ Hz, 2H), 7.68 (d, $J = 6$ Hz, 2H).

Synthesis of 5,10-dihydroindolo[3,2-b]indole (**6**).

The filtrate of stannous chloride (15.63 g, 82.413 mmol), acetic acid (35 mL), and 1 N HCl (15 mL) mixed solution was added to a mixed solution of **5** (1.237 g, 4.121 mmol) and warm acetic acid (20 mL). The reaction mixture was gently refluxed for 5 hours at 80 °C. After cooling down to room temperature, the resulting precipitates were filtered, and filtered out was washed with acetic acid, 1 N HCl, H₂O, and ethanol. The crude product was purified by flash column chromatography (ethyl acetate) and washing (CHCl₃) to afford the compound **6** as a gray solid (0.557 g, 65.5%). ¹H-NMR (300 MHz, Acetone-d6, δ): 10.26 (s, 2H), 7.78 (d, *J* = 8.4 Hz, 2H), 7.53 (d, *J* = 8.1 Hz, 2H), 7.19 (t, *J* = 6 Hz, 2H), 7.09 (t, *J* = 7.5 Hz, 2H).

Synthesis of **2HIDID**.

A round-bottom flask, equipped with a magnetic stirrer bar and reflux condenser was baked under reduced pressure and backfilled with Ar. After then, **6** (400 mg, 1.94 mmol), anhydrous THF (20 mL), and NaH (0.23 g, 9.700 mmol) were added to the baked reaction vessel. After 10 minutes at room temperature, 1-bromohexane (1.6 g, 9.700 mmol) was added into the reaction mixture. After stirring for 10 minutes, the reaction mixture was gently refluxed for 48 hours. After reaction finished, the reaction mixture was poured into brine (300 mL), and extracted with DCM. The combined organic phase was dried with MgSO₄ and concentrated under reduced pressure. The crude product was purified by flash column chromatography (ethyl acetate/n-hexane 1:4, v/v) and subsequently by recrystallization (ethanol) to afford **2HIDID** as white solid (0.553 g, 76.1%). ¹H-NMR (300 MHz, Acetone-d6, δ): 7.92 (d, *J* = 7.92 Hz, 2H),

7.61 (d, $J = 8.37$ Hz, 2H), 7.27 (td, $J = 7.11$ Hz, 1.2 Hz, 2H), 7.13 (td, $J = 7.02$ Hz, 0.99 Hz, 2H), 4.60 (t, $J = 7.08$ Hz, 4H), 1.98 (q, $J = 7.14$ Hz, 4H), 1.47-1.19 (m, 12H), 0.83 (t, $J = 7.2$ Hz, 6H). ^{13}C -NMR (500MHz, Tetrahydrofuran-d8, δ): 141.85, 126.77, 122.30, 118.84, 118.51, 115.84, 110.59, 45.89, 32.75, 31.44, 27.80, 23.59, 14.49. HRMS (FAB, m/z) Calcd. for $\text{C}_{26}\text{H}_{34}\text{N}_2$: 374.27; found: 374.2716. Elel. Anal. Calcd. for $\text{C}_{26}\text{H}_{34}\text{N}_2$: C 83.37, H 9.15, N 7.48; found: C 83.2017, H 9.1471, N 7.6164.

Synthesis of 2,7-dibromo-5,10-bis(2-octyl)-5,10-dihydroindolo[3,2-b]indole (**7**).

A round-bottom flask, equipped with a reflux condenser was baked under reduced pressure and backfilled with Ar (for three times). 2,7-dibromo-5,10-dihydroindolo[3,2-b]indole (0.720 g, 1.978 mmol), anhydrous THF (30 mL), and NaH (0.190 g, 7.911 mmol), were added into the baked reaction vessel. After 10 minutes, 3.230 g (7.911 mmol) of 1-iodo-2-octyldodecane was added to the reaction mixture. After stirring 10 for minutes, the reaction mixture was gently refluxed for 48 hours. After reaction finished, the reaction mixture was quenched with brine (300 mL), and extracted with dichloromethane. The combined organic phase was dried with MgSO_4 and concentrated under reduced pressure. The crude product was purified by column chromatography (ethyl acetate/n-hexane 1:100, v/v) to afford compound **7** as colorless oil (1.260 g, 68%). ^1H -NMR (300 MHz, Acetone-*d*6, δ): 7.84 (d, $J = 8.49$ Hz, 2H), 7.77 (d, $J = 1.5$ Hz, 2H), 7.28 (dd, $J = 8.49$ Hz, 1.59 Hz, 2H), 4.46 (d, $J = 7.65$ Hz, 4H), 2.21 (m, 2H), 1.37-1.16 (m, 64H), 0.90-0.83 (m, 12H)

Synthesis of 5,10-bis(2-octyldodecyl)-2,7-bis(4,4,5,5-tetramethyl-1,3,2-dioxaborolan-

2-yl)-5,10-dihydroindolo[3,2-b]indole (**8**).

Compound **7** (0.624 g, 0.665 mmol) and anhydrous tetrahydrofuran (25 mL) were added into a 100 mL round bottom flask and evacuated and backfilled with Ar. After then, reaction vessel was cooled down to -78°C. An hour later, n-BuLi (3.324 mmol) was added dropwise at -78°C. After an hour, 2-isopropoxy-4,4,5,5-tetramethyl-1,3,2-dioxaborolane (3.324 mmol) was added and warmed to room temperature. After reaction finished, reaction mixture was quenched with brine (300 mL), and extracted with dichloromethane. The combined organic phase was concentrated under reduced pressure, and purified by column chromatography (ethyl acetate/n-hexane 1:100, v/v) to afford compound **8** as dim yellow solid (0.320 g, 46.5%). ¹H-NMR (300 MHz, Acetone-d₆, δ): 7.97 (s, 2H), 7.95 (d, *J* = 7.98 Hz, 2H), 7.56 (d, *J* = 7.98 Hz, 2H), 4.53 (d, *J* = 7.56 Hz, 4H), 2.26 (m, 2H), 1.38-1.17 (m, 88H), 0.90-0.83 (m, 12H)

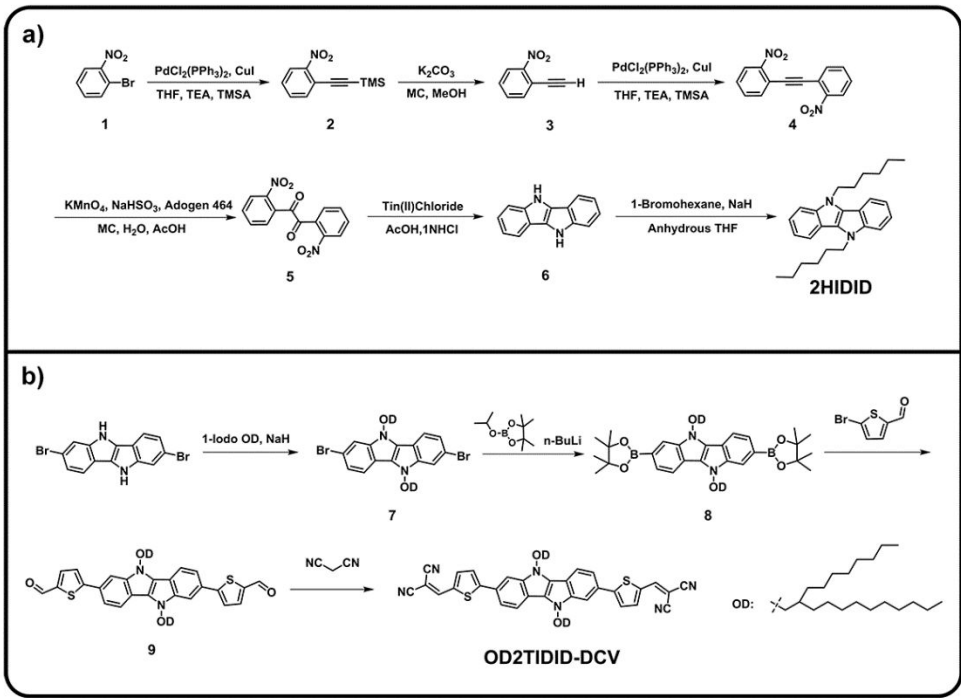
Synthesis of 5,5'-(5,10-bis(2-octyldodecyl)-5,10-dihydroindolo[3,2-b]indole-2,7-diyl)bis(thiophene-2-carbaldehyde) (**9**).

Compound **9** was synthesized by the same synthetic procedure as that for 5,5'-(5,10-dihexyl-5,10-dihydroindolo[3,2-b]indole-2,7-diyl)bis(thiophene-2-carbaldehyde) by using the compound **8** (0.180 g, 0.177 mmol), 5-bromothiophene-2-carbaldehyde (74.2 mg, 0.388 mmol), tetrakis(triphenylphosphine)palladium(0) (30.6 mg, 0.027 mmol), 2N K₂CO₃ aqueous solution (10 mL), and tetrahydrofuran (20 mL). The crude product was purified by column chromatography (chloroform/ethyl acetate/n-hexane 1:0.1:9, v/v) to afford compound **9** as red solid (160 mg, 91.7%) ¹H-NMR (300 MHz,

Tetrahydrofuran-d8, δ): 9.90 (s, 2H), 7.98 (d, J = 7.68 Hz, 2H), 7.95 (s, 2H), 7.87 (d, J = 3.9 Hz, 2H), 7.64 (d, J = 4.05 Hz, 2H), 7.61 (d, J = 8.58 Hz, 2H), 4.57 (d, J = 7.56 Hz, 4H), 2.23 (m, 2H), 1.46-1.23 (m, 64H), 0.92-0.85 (m, 12H)

Synthesis of **OD2TIDID-DCV**.

OD2TIDID-DCV was synthesized by the same synthetic procedure as that for **2HIDID-DCV** by using the compound **9** (180 mg, 0.186 mmol), malononitrile (36.9 mg, 0.0559 mmol), Al₂O₃ (0.171 g, 1.676 mmol), and methylene chloride (70 mL). The crude product was purified by flash column chromatography (tetrahydrofuran) and subsequently by recrystallization (ethyl acetate) to afford **OD2TIDID-DCV** as dark purple solid (0.155 g, 76.9%) ¹H-NMR (500MHz, Tetrahydrofuran-d8, δ): 8.22 (s, 2H), 7.94-7.90 (m, 4H), 7.85 (d, J = 4Hz, 2H), 7.69 (d, J = 4Hz, 2H), 7.60 (d, J = 8.5Hz, 2H), 4.49 (d, J = 7.5Hz, 4H), 2.24 (m, 2H), 1.39-1.18 (m, 56H), 0.88-0.82 (m, 12H). ¹³C-NMR (500MHz, Tetrahydrofuran-d8, δ): 158.82, 151.92, 143.05, 141.81, 135.08, 129.51, 127.69, 125.01, 120.03, 118.33, 116.11, 115.44, 114.77, 109.36, 76.22, 50.37, 40.03, 33.05, 33.00, 32.70, 31.10, 30.79, 30.76, 30.63, 30.58, 30.48, 30.44, 27.58, 23.74, 23.71, 14.62. HRMS (FAB, m/z) Calcd. for C₅₀H₄₂N₆S₄: 1082.70; found: 1082.6974. Elem. Anal. Calcd. for C₇₀H₉₄N₆S₂: C 77.58, H 8.74, N 7.76, S 5.92; found: C 77.5827, H 8.7514, N 7.7111, S 5.9135.



Scheme 3-2. a) Synthesis route for 5,10-dihexyl-5,10-dihydroindolo[3,2-b]indole (2HIDID), and b) OD2TIDID-DCV.

Characterization

Chemical structures of newly synthesized materials were fully identified by ^1H NMR, ^{13}C NMR, (Bruker Advanced-300 and Advanced-500), GC-Mass (JEOL, JMS-700) and elemental analysis (CE Instrument, EA1110). UV-vis spectra were recorded on a SHIMADZU UV-1650PC. HOMO and LUMO energy levels of organic materials were obtained from the cyclic voltammetry (CV) measurements. CV measurements were performed using a 273A (Princeton Applied Research) with a one-compartment platinum working electrode, a platinum wire counter-electrode, and a quasi Ag+/Ag electrode as a reference electrode. Measurement was performed in a 0.5 mM tetrahydrofuran solution with 0.1M tetrabutylammonium tetrafluoroborate (TBATFB) as a supporting electrolyte, and acetonitrile with 0.1 M tetrabutylammonium tetrafluoroborate for film as a supporting electrolyte, at a scan rate of 50 mV/s. Each oxidation and reduction potential was calibrated using ferrocene as a reference. Film surface topologies were obtained by a Bruker Nanoscope III multimode SPM with tapping mode using TREST cantilever. Out-of-plane X-ray diffraction and powder X-ray diffraction measurement was performed using a Bruker D8-Advance X-ray diffractometer. Two-dimensional grazing incidence X-ray diffraction measurement was performed at the 3C beam-line of Pohang Acceleration Laboratory. Density functional theory (DFT) calculations were performed using Gaussian 09 package B3LYP method with the basis set of 6-31G d p. The I - V characteristics of all devices were measured using Keithley 4200 SCS.

OFET device fabrication and measurement

As a OFET substrate, SiO₂/Si wafer (p-doped 300 nm) was rinsed with acetone and isopropyl alcohol, respectively, for 10 minute in an ultrasonicator, followed by 15 minute UV (360 nm) O₃ treatment.

For the thermally evaporated vacuum deposited polycrystalline OFET device fabrication, octadecyltrichlorosilane (ODTS) was treated as self-assembled monolayer (SAM) on the prepared substrate, to reduce charge trap sites as well as to enlarge domain size. ODTS was treated in vapor phase in a vacuum oven; then the substrates were passed into nitrogen filled glove box. Organic semiconductor active layers of ~30 nm thickness were thermally deposited with deposition rate of 0.1 - 0.2 Å s⁻¹ at different substrate temperatures (T_{sub} : room temperature, 50, 70, 100, 120, and 140 °C), under a vacuum of 7×10^{-7} Torr. As source and drain electrodes, 50 nm thick Au was thermally deposited with deposition rate of 0.2 - 0.3 Å s⁻¹. For the spin-coated OFET device fabrication, same substrate preparation procedure with VD device was performed. OD2TIDID-DCV were dissolved in chloroform (0.3 - 0.4 weight %), and spin-coated at 1500-3000 rpm for 1 minute in nitrogen filled glove box; then the substrates were annealed at different temperature from room temperature to 150 °C). Source and drain electrode were thermally deposited at the same condition as VD device fabrication. The *I-V* characteristics of all the OFETs were measured in a

nitrogen-filled glove box, using a Keithley 4200 SCS instrument connected to a probe station. All OFET characteristics were obtained from the transfer curve in the saturated regime. For the charge carrier mobility calculations, we checked the channel width and length of the individual devices using an optical microscope.

3.3. Results and Discussion

3.3.1 Design and Synthesis

To understand the effect of the ICT interaction and molecular structure alteration on electronic characteristics of IDID derivatives, and also to realize ambipolar OSC for practical application, I rationally designed molecular structure as follows. Using the DCV unit as a strong electronic acceptor, A- π -D- π -A type molecular architecture was designed not only for manifesting strong ICT interaction but also for enabling efficient electron injection through lowering LUMO energy level.^[25,26] In this molecular architecture, electronic and intermolecular interaction characteristics were delicately tuned by altering the π -linker (none, thiophene, bithiophene). Based on this idea, I have designed a series of three different IDID-DCV derivatives, 2HIDID-DCV, 2H2TIDID-DCV, and 2H4TIDID-DCV (**Scheme 3-1**). Synthesis of 2,7-dibromo-N,N-dihexyl-IDID (**1**) was carried out according to **Scheme 2-1** in section 2.2; from which IDID-

DCV derivatives were successfully synthesized through lithium-exchange formylation, palladium-catalyzed borylation, Suzuki-Miyaura cross-coupling, and Knoevenagel-condensation reaction in sequence. All the three target compounds were carefully characterized by ^1H NMR, ^{13}C NMR, elemental analysis, and mass analysis. Detailed synthetic procedures are described in **Scheme 3-1 and Experimental Section**.

For the comprehensive understanding of newly synthesized IDID-DCV derivatives in terms of their photophysical properties, I also prepared three IDID reference materials, 2HIDID, 2H₂TIDID, and 2H₄TIDID, which have exactly the same molecular structures with those of 2HIDID-DCV, 2H₂TIDID-DCV, and 2H₄TIDID-DCV but without acceptor unit (DCV), respectively (see **Scheme 3-1**, 2H₂TIDID and 2H₄TIDID were described in **chapter 1**, but 2HIDID was newly synthesized in this chapter. Detailed synthetic procedure and characterization of 2HIDID is described in **Experimental Section**).

3.3.2. Theoretical, Optical, and Electrochemical Properties

The electronic characteristics of IDID-DCV derivatives were evaluated through the molecular orbital calculation, UV-vis spectroscopy, and cyclic voltammetry (CV) measurement. Ground-state optimized geometries and electronic structures of IDID derivatives were calculated within the density functional theory (DFT) B3LYP method

by using Gaussian 09 package with basis set of 6-31G d p. According to the calculated frontier orbital energies shown in **Figure 3-1**, it is noted that the effect of different π -linking units (none, thiophene, bithiophene) in IDID-DCV derivatives is quite different from that in p-type IDID reference derivatives. Because IDID unit intrinsically holds very low ionization potential, π -conjugation extension with thiophene unit mostly resulted in the stabilization of LUMO energies without any HOMO variation in case of the p-type reference derivatives. On the other hand, both the HOMO and LUMO energies of a given IDID-DCV derivative were strongly stabilized compared to those of respective IDID reference derivative, the actual degree of stabilization increased in the order of different π -linking units (none > thiophene > bithiophene) as seen in **Figure 3-1**. This can be rationally correlated with the increasing strength of ICT characteristics with decreasing D-A distance.

For the empirical exploration of electronic transition, UV-vis absorption spectra of IDID derivatives were measured at a concentration of 1×10^{-5} M in tetrahydrofuran (THF) solutions and also for spin-coated films (see **Figure 3-2**, detailed data listed in **Table 3-1**). In solution states, all the IDID-DCV derivatives exhibited broad absorption bands consisting of three absorption maxima. Interestingly, the location of lowest energy transition maxima corresponding to the ICT transition were virtually the same for all of them (544 nm for 2HIDID-DCV, and 555 nm for 2H2TIDID-DCV and 2H4TIDID-DCV), in spite of their different π -linker length from each other. This

feature can be comprehended by comparing their absorption spectra with those of the reference derivatives. As shown in **Figure 3-2c**, IDID-DCV derivatives show different degree of bathochromically shifted absorption spectra ($\Delta \lambda_{\text{max.}}$ vs. reference derivative; see **Table 3-1**) which increases with decreasing D-A distance. The apparently similar ICT absorption wavelengths among IDID-DCV derivatives can thus be rationalized by compromised ICT strength and conjugation length effects. Strength of ICT interaction between IDID and DCV is getting weaker for the molecules with larger number of thiophene π -spacer, which at the same time is compensated by increased π -conjugation length to give comparable absorption λ maximum. In the solid states samples of IDID-DCV derivatives, further bathochromic shifts of 90-100 nm with distinct vibronic features are observed as shown in **Figure 3-2b** and summarized in **Table 3-1**.

To investigate electrochemical properties of IDID-DCV derivatives, cyclic voltammetry (CV) measurements were made both in solution states and solid (film) states. The HOMO, LUMO, and electrochemical band-gap energies which were extracted from the first oxidation onset and the first reduction onset of CV curves are listed in **Table 3-1**. As shown in **Figure 3-3**, IDID-DCV derivatives exhibited quasi-reversible multistage electrochemical oxidation and reduction behaviors in THF solvent. Consistent with the DFT calculation results in **Figure 3-1**, LUMO energies of IDID-DCV derivatives were strongly stabilized and located at similar level (about -3.5 eV) as seen in **Figure 3-3** and **Table 3-1**. Meanwhile, HOMO energies were gradually

destabilized with increasing π -spacer length; i.e., -5.34, -5.08, and -4.90 eV. Consequently, quite small band-gap (i.e., down to 1.41 eV) could be achieved through the using compensated ICT interaction between IDID and DCV. In case of film states, HOMO and LUMO energies of IDID-DCV derivatives were even further stabilized with higher degree of stabilization for LUMO energies than HOMO energies to give smaller band-gap energies. Interestingly, largest solid state LUMO stabilization to give the smallest band-gap energy of 1.23 eV was observed for 2H₂TIDID-DCV (**see Table 3-1**), which attests the most strong and efficient electronic interaction in the tightly packed solid state suggesting its excellent OFET mobility (*vide infra*).

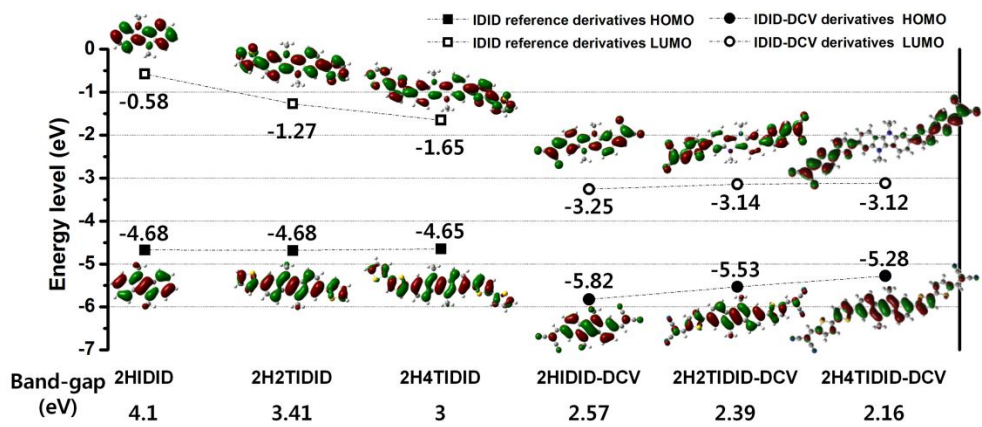


Figure 3-1. Plot of calculated energy levels for IDID-DCV derivatives and IDID reference derivatives, and their molecular orbital contour (DFT/B3LYP-6-31G d p, the alkyl chains were replaced by methyl in calculation).

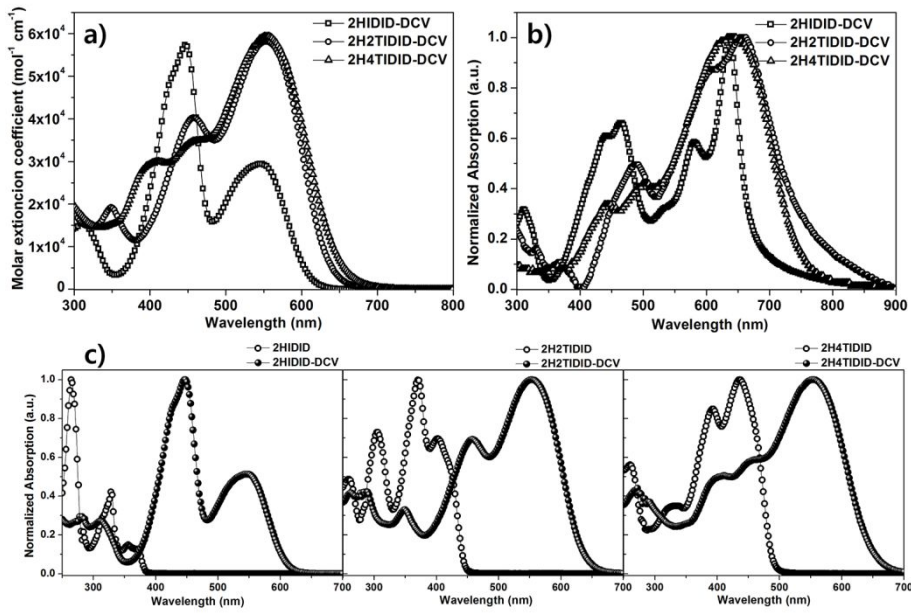


Figure 3-2. Absorption spectra of IDID-DCV derivatives for solution state (a) and film state (b), and each solution state absorption spectra with correspondent reference (c).

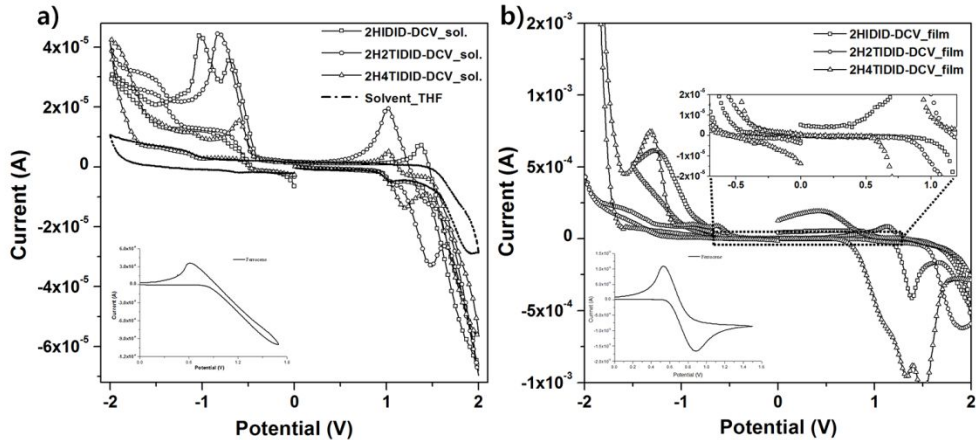


Figure 3-3. Cyclic voltammograms of IDID-DCV derivatives in solution state (a) and film state (b).

Table 3-1. Optical and electrochemical properties of IDID-DCV derivatives.

Compound	Abs. λ_{\max} [sol./film/ $\Delta \lambda_{\max}$, nm] ^{a)}	$\Delta \lambda_{\max}$ [nm] ^{b)}	HOMO [sol./film, eV] ^{c)}	LUMO [sol./film, eV] ^{c)}	Band-gap [sol./film, eV] ^{d)}
2HIDID-DCV	544/636/89	179	-5.34/-5.42	-3.51/-3.71	1.81/1.71
2H2TIDID-DCV	555/657/103	151	-5.08/-5.09	-3.46/-3.86	1.62/1.23
2H4TIDID-DCV	555/641/89	118	-4.90/-4.99	-3.49/-3.74	1.41/1.25

^{a)} λ_{\max} is extracted from lowest spin-allowed transition maximum, $\Delta \lambda_{\max}$ presents λ_{\max} difference between solution state and film state, solution absorption spectra were measured in THF (concentration of 1×10^{-5} M), and film absorption spectra were measured with spin-coated sample (1500 RPM/60s, 0.3 wt% in chloroform); ^{b)} Abs. λ_{\max} difference between IDID-DCV derivatives and correspondent IDID reference; ^{c)} HOMO and LUMO energy levels were determined by cyclic voltammetry. Solution sample was prepared 3×10^{-3} M in THF and film sample was prepared on ITO patterned glass by drop-casting; ^{d)} band-gap = $V_{\text{oxidation}} - V_{\text{reduction}}$.

3.3.3. OFET Characteristics

Based on the photophysical and electrochemical properties (i.e., satisfactorily low band-gap with suitable HOMO and LUMO energy in the solid state for efficient bipolar injection from symmetric source-drain electrodes), two of the IDID-DCV derivatives, 2H₂TIDID-DCV and 2H₄TIDID-DCV, were selected for the evaluation of OFET characteristics. Before the OFET device fabrication, however, I have examined their VD thin-film surface topography as a function of substrate temperature (T_{sub}) alteration. As shown in **Figure 3-4**, 2H₂TIDID-DCV films showed dense and compact grain features suitable for OFET fabrication, whilst 2H₄TIDID-DCV VD films showed coarse and unfilled topological characteristics unsuitable for device evaluation. Therefore, charge transporting characteristics of 2H₂TIDID-DCV was evaluated for its ambipolar mobility in the geometry of bottom-gate top-contact (BGTC) VD OFET devices. 2H₂TIDID-DCV was thermally evaporated and deposited on octadecyltrichlorosilane (ODTS) treated SiO₂/Si substrates at different T_{sub} from room temperature (RT) to 140 °C to optimize the device performance. 2H₂TIDID-DCV OFET devices showed ambipolar OFET behavior exhibiting typical V-shaped transfer curves and unique output curves with superlinear regime as seen in **Figure 3-5a** to f. With the T_{sub} increase, hole and electron mobilities were increased simultaneously (see **Figure 3-6** and **Table 3-2**). In particular, the electron mobility was much more

dramatically enhanced by altering the deposition temperature (nearly four orders of magnitude increase, from $1.5 \times 10^{-5} \text{ cm}^2 \text{ V}^{-1} \text{ s}^{-1}$ to 9.2×10^{-2}) than that of hole mobility (from $1.8 \times 10^{-3} \text{ cm}^2 \text{ V}^{-1} \text{ s}^{-1}$ to 8.2×10^{-2}), and the devices which were deposited at high T_{sub} ($> 70 \text{ }^\circ\text{C}$), showed well balanced hole and electron mobilities (hole mobility to electron mobility ratio is 0.63 at T_{sub} of $140 \text{ }^\circ\text{C}$). Such different tendency of electron and hole mobility modulation is most probably due to the higher sensitivity for the trap site of electron charge carrier than that of hole charge carrier.^[27] The mobility increment could be attributed to the reduced density of trap sites originating from increased grain size, as was rationalized from surface topography study using atomic force microscopy (AFM) measurement. As shown in **Figure 3-7a** to f, surface topography of 2H2TIDID-DCV film evolved from uniform film (root-mean-square roughness value of 0.7 nm) to highly ordered crystalline films with terrace-structured grains along with increasing T_{sub} ; structured grains were developed from T_{sub} of $70 \text{ }^\circ\text{C}$, and micron-sized grains were observed from T_{sub} of $120 \text{ }^\circ\text{C}$. By correlating charge carrier mobility and surface topography, it was found that the terrace-structured and enlarged grains are responsible for the favorable intermolecular packing structure for the transport of both hole and electron charge carriers.

To demonstrate a solution processable IDID-DCV derivative, I additionally synthesized OD2TIDID-DCV, for which linear hexyl side chains in 2H2TIDID-DCV were replaced by branched 2-octyldodecyl group (see **Scheme 3-2**, detailed synthetic

procedures and characterizations are described in section 3-2 **Experimental** section). Spin-coated OFET devices of OD2TIDID-DCV were fabricated and characterized for the same OFET structure and geometry as the VD ones, but with the semiconductor material (OD2TIDID-DCV) deposited by spin-coating method. As shown in **Figure 3-5g to j**, optimized spin-coated OFET device (post annealing temperature of 150 °C) exhibited ambipolar charge transport behavior with hole and electron mobilities of $9.6 \times 10^{-2} \text{ cm}^2 \text{ V}^{-1} \text{ s}^{-1}$ and $3.4 \times 10^{-3} \text{ cm}^2 \text{ V}^{-1} \text{ s}^{-1}$, respectively. With respect to the charge carrier mobility values, solution processed OD2TIDID-DCV devices exhibited slightly higher hole mobility but relatively lower electron mobility values than those of 2H2TIDID-DCV. Such different mobility values is due to the somewhat different π - π distance, *vide infra*, and rather smaller grain size compared to that of optimized VD device (see **Figure 3-7g**). Anyway, experimentally evidenced ambipolarity in the 2H2TIDID-DCV and OD2TIDID-DCV devices suggest that 2TIDID-DCV is a promising π -conjugate backbone for the single-component ambipoar OFET.

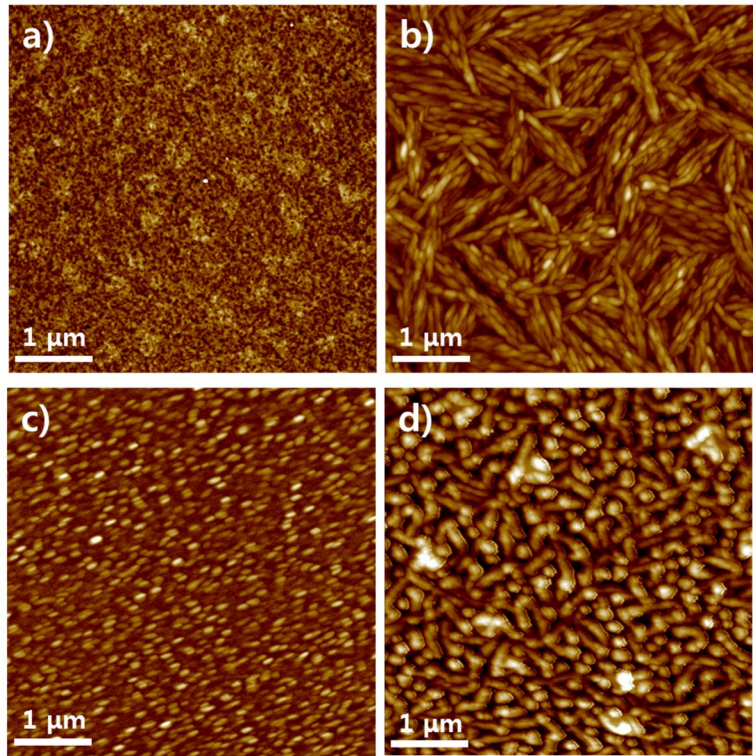


Figure 3-4. AFM surface topologies (height images, $5 \mu\text{m} \times 5 \mu\text{m}$) of 2H2TIDID-DCV (a and b) and 2H4TIDID-DCV (c and d) VD thin films under different T_{sub} ((a and c) RT; (b and d) 70°C).

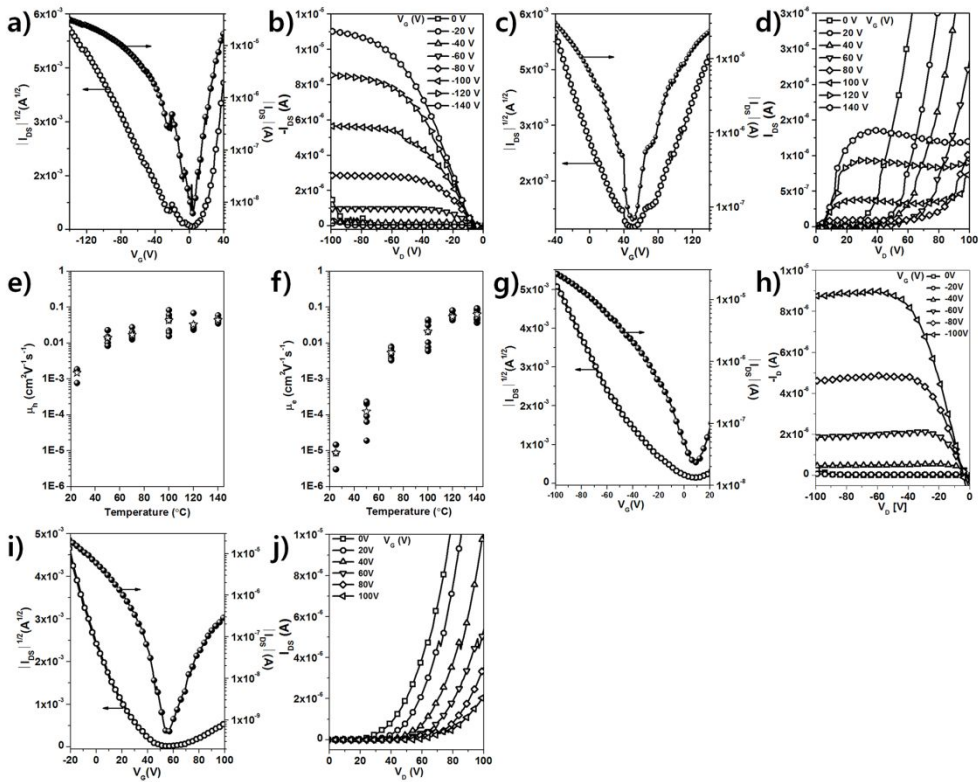


Figure 3-5. OFET devices characteristics. (a to f) Representative OFET device characteristics of 2H2TIDID-DCV ((a and c) transfer curves of T_{sub} 120 °C device, (b and d) output curves T_{sub} 120 °C device, and (e and f) temperature dependent mobility for p- and n-channel operation, respectively. (white stars represent average value)); (g and j) Spin-coated OFET device characteristics of OD2TIDID-DCV (annealing temperature is 150 °C, (g and i) transfer curves and (h and j) output curves for p- and n-channel operation, respectively).

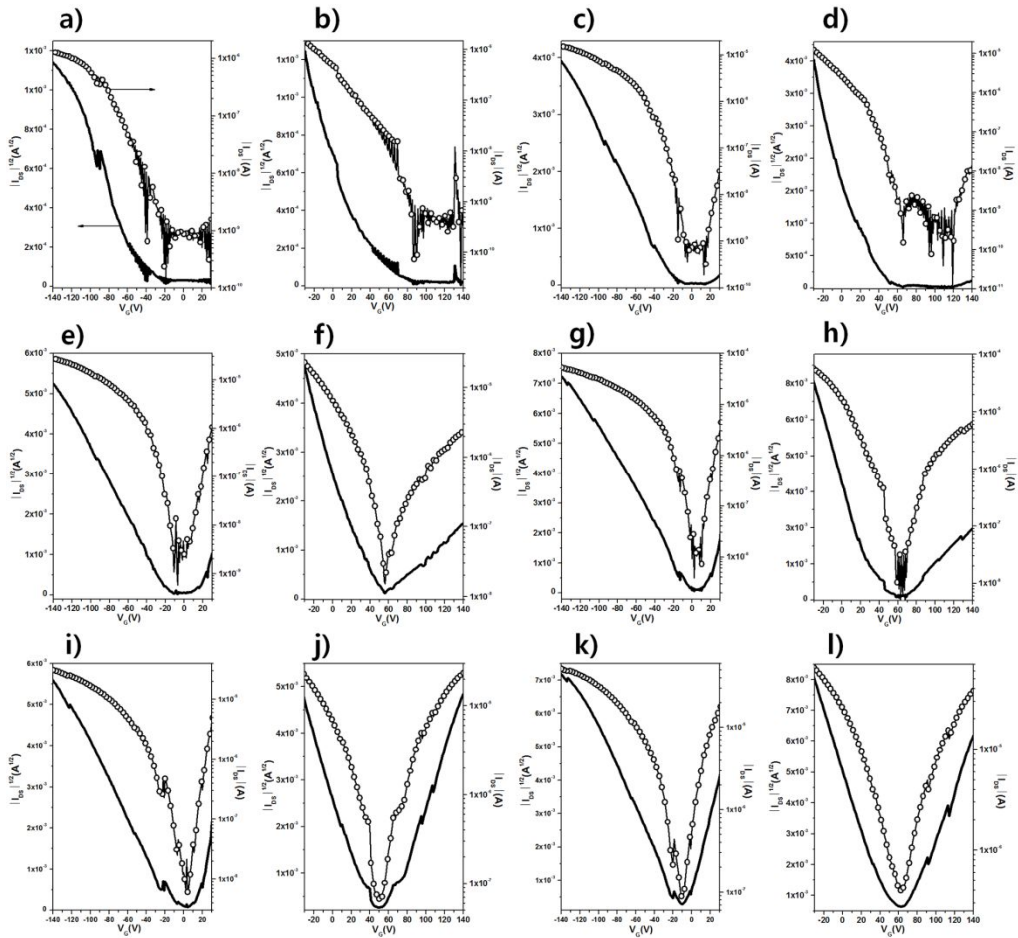


Figure 3-6. The transfer curves of 2H2TIDID-DCV OFET devices for p- and n-channel operation with different T_{sub} , respectively ((a and b) T_{sub} RT, (c and d) T_{sub} 50°C, (e and f) T_{sub} 70°C, (g and h) T_{sub} 100°C, (i and j) T_{sub} 120°C, (k and l) T_{sub} 140°C).

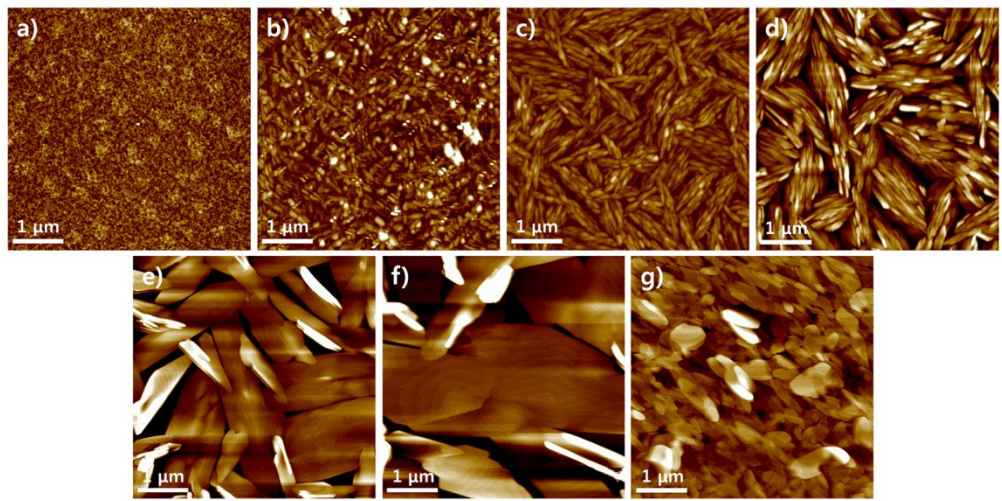


Figure 3-7. AFM surface topologies (height images, $5 \mu\text{m} \times 5 \mu\text{m}$) of 2H2TIDID-DCV VD thin films under different T_{sub} ((a) RT; (b) 50 °C; (c) 70 °C; (d) 100°C; (e) 120 °C; (f) 140 °C), and OD2TIDID-DCV spin-coated film ((g-i), annealed at 150 °C).

Table 3-2. OFET device characteristics.

Compound	T_{sub} [°C] ^{a)}	p-channel operation			n-channel operation			p/n ratio
		μ_h , max/average [cm ² V ⁻¹ s ⁻¹] ^{b)}	V_{th} [V] ^{c)}	I_{on}/I_{off}	μ_e , max/average [cm ² V ⁻¹ s ⁻¹] ^{b)}	V_{th} [V] ^{c)}	I_{on}/I_{off}	
2H2TIDID- DCV	RT	1.85 × 10 ⁻³ / 1.43 × 10 ⁻³	-42 (±8)	3 × 10 ⁴	1.47 × 10 ⁻⁵ / 8.79 × 10 ⁻⁶	60 (±5)	2 × 10 ¹	125.85
	50	2.30 × 10 ⁻² / 1.39 × 10 ⁻²	-22 (±12)	1 × 10 ⁵	2.32 × 10 ⁻⁴ / 1.23 × 10 ⁻⁴	100 (±10)	3 × 10 ²	99.14
	70	2.76 × 10 ⁻² / 1.69 × 10 ⁻²	-9 (±9)	4 × 10 ⁴	8.07 × 10 ⁻³ / 5.39 × 10 ⁻³	67 (±18)	3 × 10 ³	3.42
	100	8.28 × 10 ⁻² / 4.30 × 10 ⁻²	-7 (±3)	1 × 10 ³	4.46 × 10 ⁻² / 2.09 × 10 ⁻²	61 (±10)	5 × 10 ²	1.86
	120	6.86 × 10 ⁻² / 3.30 × 10 ⁻²	-13 (±4)	4 × 10 ³	8.13 × 10 ⁻² / 5.45 × 10 ⁻²	61 (±13)	9 × 10 ²	0.84
	140	5.89 × 10 ⁻² / 4.41 × 10 ⁻²	-15 (±3)	1 × 10 ⁴	9.24 × 10 ⁻² / 6.21 × 10 ⁻²	77 (±9)	3 × 10 ³	0.63
OD2TIDID- DCV	150 ^{d)}	9.67 × 10 ⁻² / 5.28 × 10 ⁻²	-24 (±9)	4 × 10 ⁴	3.42 × 10 ⁻³ / 1.25 × 10 ⁻³	50 (±11)	1 × 10 ²	28.27

^{a)} Substrate temperature in vacuum deposition; ^{b)} The mobilities were extracted from the saturation regimes; ^{c)} Average threshold voltages. The values in the parentheses are standard deviation; ^{d)} Post annealing temperature of spin-coated device (°C).

3.3.4. Structural Analyses

To investigate the molecular packing structure in the organic semiconductor samples, out-of-plane X-ray diffraction (XRD), powder XRD, and 2D grazing incidence X-ray diffraction (2D-GIXD) analyses were carried out. **Figure 3-8a** shows out-of-plane XRD patterns of 2H2TIDID-DCV thin films. While low T_{sub} (RT and 50 °C) samples exhibited quite dim diffraction peaks, samples which were deposited at high T_{sub} (over 70 °C) exhibited sharp and strong diffraction peaks up to the third (300) order, at 2 theta degrees of 8.37°, 16.78°, and 25.28°; this could be interpreted as lamellar diffraction with a *d*-spacing of 10.58 Å. From the powder XRD, (**Figure 6b**) identical lamellar diffraction peaks with those of out-of-plane XRD could be observed at almost same 2 theta degrees (8.36°, 16.67°, and 25.16°), and moreover, I could recognize diffraction peak at wide angle region (24.9°) which might be interpreted as π - π distance with a *d*-spacing of 3.57 Å (inset of **Figure 3-8b**). The 2D-GIXD result of 2H2TIDID-DCV thin film could further support our interpretation; diffraction peaks corresponding to lamellar and π - π *d*-spacing at q_z of 0.60 Å⁻¹ (10.47 Å) and q_{xy} of 1.76 Å⁻¹(3.57 Å), respectively, were absorbed. Moreover, the 2D-GIXD patterns of OD2TIDID-DCV spin-coated film also exhibited similar result with that of 2H2TIDID-DCV; i.e., semiconductor molecules are oriented exactly same manner with that of 2H2TIDID-DCV VD film but with different values of *d*-spacing (the lamellar spacing and π - π

spacing values are 17.9 Å and 3.64 Å, respectively). Through the comprehensive correlation between XRDs, DFT calculation, and AFM surface topographic results shown in **Figure 3-8**, it was concluded that 2H2TIDID-DCV (and OD2TIDID-DCV) molecules are oriented on the substrate with edge-on manner, and their π -planes are stacked up toward surface parallel direction. On the other hand, van der Waals interactions of *N*-aliphatic chains enable 2H2TIDID-DCV and OD2TIDID-DCV to construct well-organized three-dimensional lamellar structure with lamellar spacing of 10.58 Å and 17.9 Å, respectively (see **Figure 3-8j**).

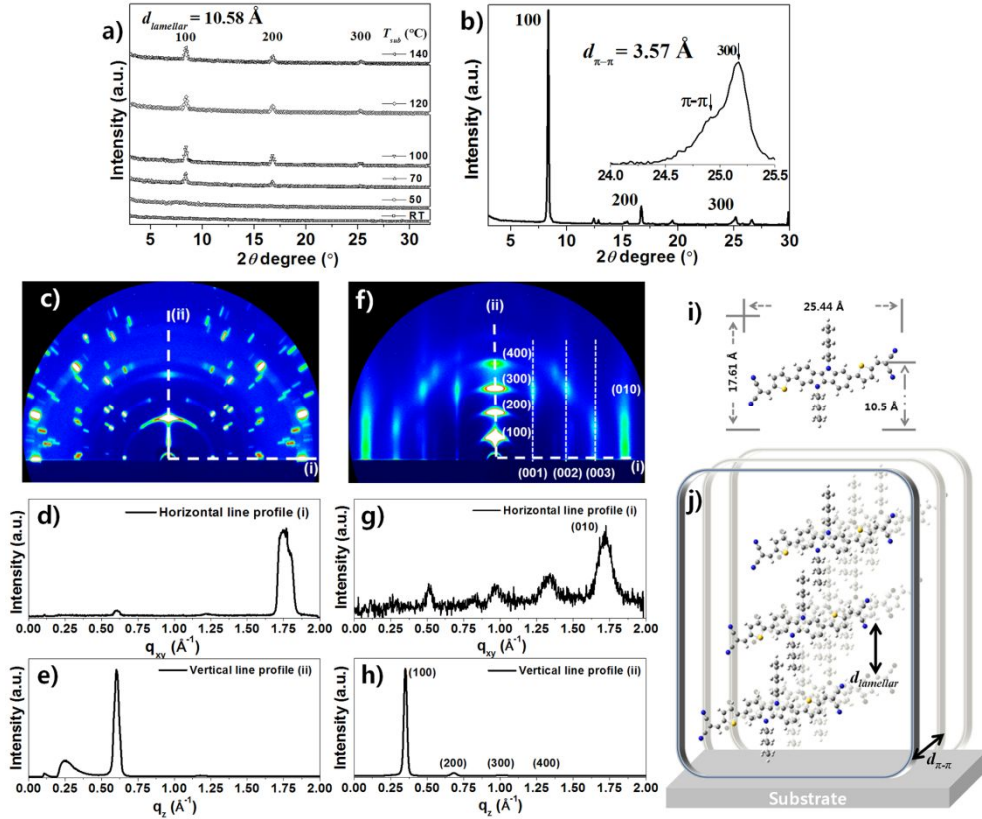


Figure 3-8. (a) Out-of-plane XRD pattern of 2H2TIDID-DCV VD films under different T_{sub} ; (b) Powder XRD pattern of 2H2TIDID-DCV powder; (c) 2D-GIXD diffraction pattern image of 2H2TIDID-DCV VD films ($T_{\text{sub}} 140^{\circ}\text{C}$); (d and e) Horizontal and vertical line profile of (c), respectively; (f) 2D-GIXD diffraction pattern image of OD2TIDID-DCV film; (g and h) Horizontal and vertical line profile of (e), respectively; (i) Calculated molecular size of 2H2TIDID-DCV; (j) Schematic diagram of 2H2TIDID-DCV packing structure.

3.4. Conclusion

I have designed and successfully synthesized A- π -D- π -A type IDID-DCV derivatives with different π -spacer. It was found that the compensated ICT interaction between IDID and DCV of 2TIDID-DCV derivatives (with thiophene π -spacer) and their efficient electronic interaction in the three-dimensional lamellar π -stacking structure gave rise to the dramatically reduced energy band-gap as well as excellent film morphology. As a consequence, the VD OFET device using 2H2TIDID-DCV exhibited highly balanced ambipolar charge transport with hole and electron mobilities of $0.08 \text{ cm}^2 \text{ V}^{-1} \text{ s}^{-1}$ and $0.09 \text{ cm}^2 \text{ V}^{-1} \text{ s}^{-1}$, respectively, and the spin-coated OFET devices using OD2TIDID-DCV, also exhibited ambipolar charge transport behavior (mobility of $9.67 \times 10^{-2} \text{ cm}^2 \text{ V}^{-1} \text{ s}^{-1}$ for hole, and $3.43 \times 10^{-3} \text{ cm}^2 \text{ V}^{-1} \text{ s}^{-1}$ for electron).

3.5. Reference

- [1] J. G. Champlain, *Appl. Phys. Lett.* **2011**, *99*, 123502.
- [2] J. Zaumseil, H. Siringhaus, *Chem. Rev.* **2007**, *107*, 1296.
- [3] S.-I. Noro, T. Takenobu, Y. Iwasa, H.-C. Chang, S. Kitagawa, T. Akutagawa, T. Nakamura, *Adv. Mater.* **2008**, *20*, 3399.
- [4] T. D. Anthopoulos, S. Setayesh, E. Smits, M. Cölle, E. Cantatore, B. Bore, P. W. M. Blom, D. M. Leeuw, *Adv. Mater.* **2006**, *18*, 1900.
- [5] K. Liu, C. -L. Song, Y. -C. Zhou, X. -Y. Zhou, X. -J. Pan, L. -Y. Cao, C. Zhang, Y. Liu, X. Gong, H. -L. Zhang, *J. Mater. Chem. C.* **2015**, *3*, 4188.
- [6] J. Bardeen, *J. Phys. Rev.* **1947**, *71*, 717.
- [7] T. Kanagasekaran, H. Shimotani, S. Ikeda, H. Shang, R. Kumashiro, K. Tanigake, *Appl. Phys. Lett.* **2015**, *107*, 043304.
- [8] E. J. Meijer, D. M. D. Leeuw, S. Setayesh, E. V. Veenendaal, B. -H. Huisman, P. W. M. Blom, J. C. Hummelen, U. Scherf, T. M. Klapwijk, *Nat. Mater.* **2003**, *2*, 678.
- [9] B. Jaeckel, J. B. Sambur, B. A. Parkinson, *Appl. Phys. Lett.* **2008**, *103*, 063719.
- [10] T. Yasuda, T. Goto, K. Fujita, T. Tsutsui, *Appl. Phys. Lett.* **2004**, *85*, 2098.
- [11] J. -Y. Hu, M. Nakano, I. Osaka, K. Takimiya, *J. Mater. Chem. C.* **2015**, *3*, 4244.

- [12] M. L. Tang, A. D. Reichardt, N. Miyaki, R. M. Stoltenberg, Z. Bao, *J. Am. Chem. Soc.* **2008**, *130*, 6064.
- [13] Y.-Y. Liu, C.-L. Song, W.-J. Zeng, K.-G. Zhou, Z.-F. Shi, C.-B. Ma, F. Yang, H.-L. Zhang, X. Gong, *J. Am. Chem. Soc.* **2010**, *132*, 16349.
- [14] C.-L. Song, C.-B. Ma, F. Yang, W.-J. Zeng, H.-L. Zhang, X. Gong, *Org. Lett.* **2011**, *13*, 2880.
- [15] J. Lee, A. -R. Han, H. Yu, T. J. Shin, C. Yang, J. H. Oh, *J. Am. Chem. Soc.* **2013**, *135*, 9540.
- [16] B. Sun, W. Hong, Z. Yan, H. Aziz, Y. Li, *Adv. Mater.* **2014**, *26*, 2636.
- [17] L. Wang, X. Zhang, H. Tian, Y. Lu, Y. Geng, F. Wang, *Chem. Commun.* **2013**, *49*, 11272.
- [18] A. Riaño, P. M. Burrezo, M. J. Mancheño, A. Timalsina, J. Smith, A. Facchetti, T. J. Marks, H. T. L. Navarrete, J. L. Segura, J. Casado, R. P. Ortiz, *J. Mater. Chem. C.* **2014**, *2*, 6376.
- [19] M. Irimia-Vladu, E. D. Głowacki, P. A. Troshin, G. Schwabegger, L. Leonat, D. K. Susarova, O. Krystal, M. Ullah, Y. Kanbur, M. A. Bodea, V. F. Razumov, H. Sitter, S. Bauer, N. S. Sariciftci, *Adv. Mater.* **2012**, *24*, 375.
- [20] I. Meager, M. Nikolka, B. C. Schroeder, C. B. Nielsen, M. Planells, H. Bronstein, J. W. Rumer, D. I. James, R. S. Ashraf, A. Sadhanala, P. Hayoz, J.-C. Flores, H. Sirringhaus, I. McCulloch, *Adv. Funct. Mater.* **2014**, *24*, 7109.
- [21] J. C. Ribierre, L. Zhao, S. Furukawa, T. Kikitsu, D. Inoue, A. Muranaka, K.

- Takaishi, T. Muto, S. Matsumoto, D. Hashizume, M. Uchiyama, P. André, C. Adachi, T. Aoyama, *Chem. Commun.* **2015**, *51*, 5836.
- [22] J. Li, X. Qiao, Y. Xiong, H. Li, D. Zhu, *Chem. Mater.* **2014**, *26*, 5782.
- [23] J. C. Ribierre, S. Watanabe, M. Matsumoto, T. Muto, D. Hashizume, T. Aoyama, *J. Phys. Chem. C* **2011**, *115*, 20703.
- [24] K. Zhou, H. Dong, H. -L. Zhang, W. Hu, *Phys. Chem. Chem. Phys.* **2014**, *16*, 22448.
- [25] T. Qi, Y. Liu, W. Qiu, H. Zhang, X. Gao, Y. Liu, K. Lu, C. Du, G. Yu, D. Zhu, *J. Mater. Chem.* **2008**, *18*, 1131.
- [26] X. Lu, S. Fan, J. Wu, X. Jia, Z. -S. Wang, G. Zhou, *J. Org. Chem.* **2014**, *79*, 6480.
- [27] H. Dong, X. Fu, J. Liu, Z. Wang, W. Hu, *Adv. Mater.* **2013**, *25*, 6158.

Chapter 4.

Crystal Engineering of Indolo[3,2-b]indole Derivatives for High Performance Single-Crystal Organic Field-Effect Transistor: Exploring Fluorination Effect on Structural and Electrical Characteristics

4.1. Introduction

During the last two decades, magnificent advances have been made in organic field-effect transistors (OFETs) in terms of their electrical performance and theoretical fundamentals.^[1-4] Particularly, single crystal (SC) OFETs have drawn great attentions because their defect-free long-range ordered molecular arrangement and clearly resolved crystalline structure provide opportunity to evaluate inherent charge transport property as well as in-depth study of structure-property relationship.^[5] Generally, charge carrier transport between π -conjugated materials can be appropriately explained by hopping mechanism (at room temperature), and the nature of transport depends sensitively on their electronic interactions and electron-phonon interactions.^[6] Consequently, solid state electronic structure and charge carrier mobility are determined not only by the chemical structure of the molecule but also by the intermolecular stacking structure.^[1,7] In this sense, recently, great efforts are devoted to control molecular arrangement for maximizing π -orbital overlap with neighboring

molecules, and to understand the nature of inherent molecular interaction by examining their structure-property correlation.

As a strategy of tuning the molecular arrangement, introduction of non-covalent secondary interactions such as electrostatic interactions, van der Waals interaction, and π - π interactions is most promisingly considered. For instance, Anthony group reported in-depth structure-property correlations of pentacene derivatives for the crystal engineering; e.g., incorporating bulky substituents, replacing phenyl rings with thiophene rings, and introducing halogen atom into peripheries.^[8-12] Bao group and Zhu group reported chlorinated polycyclic aromatic hydrocarbons (PAHs) (5,11-dichlorotetracene and 6,13-dichloropentacene, respectively) which exhibited π -stacking motif different from those of parent PAHs to give impressive hole mobility (hole mobility of $1.6\text{ cm}^2\text{ v}^{-1}\text{ s}^{-1}$ and $9\text{ cm}^2\text{ v}^{-1}\text{ s}^{-1}$, respectively).^[13,14] Recently, Pei group reported structure-property correlation of fluorinated benzodifurandione-based oligo(*p*-phenylenevinylene) derivatives of which packing structures were delicately controlled through altering number and position of substituent fluorine atoms.^[15] To date, only a few molecular systems have been investigated for crystal engineering. This is because the nature of intermolecular interaction is very sensitively dependent on chemical structure, and exact prediction of molecular packing is extremely difficult. Therefore, to establish general guidelines for the crystal engineering, research and investigations in various molecular systems are strongly demanded.

Among various kinds of heteroacenes, pyrrole-containing one consisting of, for instance, carbazole, indolocarbazole, and indoloindole, have been considered as one of the most promising backbone units for the organic semiconductor owing to their rigid and planar backbone structure, high ionization potential, and feasibly controllable chemical structure. Therefore, their derivatives have been reported with substantial device performances for various applications in organic electronics.^[16-17] However, many of their derivatives for OFETs exhibited herringbone packing structure owing to the abundant electron density on their π -plane giving rise to electrostatic repulsion. Moreover, their π -plane is largely mismatched with neighboring molecules in solid state because of the presence of bulky substituents in central *N*-positions.^[18-20] In this regard, to realize high performance OFETs by increasing the degree of π -orbital overlap, various attempts, such as extending fused structure and introducing self-organization functional groups, have been attempted.^[21-23] In the course of my investigation on IDID-based organic semiconductor, I also observed aforementioned tendency of molecular interaction for one of the IDID derivatives, i.e., 2H2TIDID which exhibited slipped-herringbone structure, distorted π -plane, and conformational polymorphism.^[24] To solve such kinds of drawbacks and to provide effective strategy for the crystal engineering, I tried to tune the molecular interaction motif of indolo[3,2-*b*]indole (IDID) derivatives through the incorporation of fluorine (F) atom into the IDID core. Fluorine atom which is known to generate inter- and/or intramolecular secondary interaction (F···F, C-H···F, and F··· π), has the smallest van der Waals

radius (1.47Å) and the largest Pauling electronegativity (3.98), among halogens. Therefore, by the F atom substitution at appropriate position of the IDID core, I could expect π -conjugated backbone planarization through the intramolecular secondary bonding interactions (conformation locking), minimal steric hindrance between aromatic substituents and IDID core, and efficient control of the electron density on IDID derivatives.^[25] To examine the F atom incorporation effect on pyrrole-fused heteroacene derivatives, I have carefully carried out structure-property correlation between fluorinated and non-fluorinated IDID derivatives through the single crystal X-ray diffraction (SC XRD) analyses and the density functional theory (DFT) calculation. From the results, it was concluded that incorporation of F atom into IDID core gave rise to inter and/or intramolecular C-H \cdots F hydrogen bonds, and molecular packing structure could be efficiently controlled; changing from herringbone to π -stack (*vide infra*). Furthermore, 4H4TIDIDF for which hydrogen atoms of 3- and 8-position of IDID in 4H4TIDID were replaced by F atom to develop advanced IDID-based organic semiconductor, which exhibited remarkably high p-type field-effect mobility of 1.88 cm 2 V $^{-1}$ s $^{-1}$ from SC OFET device with molecular packing structure of slipped π -stack.

4.2. Experimental

Synthesis

Fluorine substituted IDID derivatives, 2H2TIDID and 4H4TIDID, were synthesized according to the procedure shown in **Scheme 4-1**. Synthesis of 2H2TIDID was described in **chapter 2**. Unless otherwise stated, all reagents were purchased at Sigma Aldrich, TCI, and Alfa Aesar.

Synthesis of 5-fluoro-2-nitroaniline (**2**).

5-fluoro-2-nitrobenzene (30.00 g, 192.16 mmol), N-bromosuccinimide (35.91 g, 201.77 mmol), and 500 mL of acetic acid were added to a 1000 mL two-neck round-bottom flask, equipped with a magnetic stirrer bar and a reflux condenser. The reaction mixture was gently refluxed during 1.5 hours. After reaction finished, the reaction mixture was cooled down to room temperature, after then, poured into 1500 mL of distilled water (H_2O). The yellow precipitates were collected by filtration and washed with H_2O (500 mL \times 2) to afford compound **2** (40.35 g, yield 89.35%). $^1\text{H-NMR}$ (300 MHz, CDCl_3 , δ): 8.39 (d, $J = 7.08$ Hz, 1H), 6.60 (d, $J = 9.60$ Hz, 1H), 6.1963 (s, 2H)

Synthesis of 1-bromo-2-fluoro-4-iodo-5-nitrobenzene (**3**).

H_2O (40 mL) and H_2SO_4 (75 mL) mixed solution was slowly added to a mixed solution of acetic acid (70 mL), and 4-bromo-2-nitroaniline (20.00 g, 85.10 mmol) using dropping funnel at 0°C. Afterwards, a solution of NaNO_2 (6.46 g, 93 mmol, in 20 mL of H_2O) was added dropwise to the reaction mixture and stirred an hour. After then, a solution of KI (16.95 g, 102 mmol, in 20 mL of H_2O) was added dropwise. After completion of the addition, the reaction mixture was heated to 60 °C for 3 hours,

cooled down to 0°C again, and dichloromethane was added until all precipitates were completely dissolved. The reaction mixture was poured into 400 mL of saturated NaHCO₃ aqueous solution in ice bath and extracted with dichloromethane. The organic phase was washed with brine and saturated Na₂S₂O₃ aqueous solution (250 mL x 2, each), dried over MgSO₄, filtered, and concentrated, sequentially. The concentrated crude product was recrystallized from hexane to afford compound **3** as an orange crystal (15.70 g, yield 53.35%). ¹H-NMR (300 MHz, CDCl₃, δ): 8.18 (d, *J* = 6.21 Hz 1H), 7.81 (d, *J* = 7.35 Hz, 1H)

Synthesis of ((4-bromo-5-fluoro-2-nitrophenyl)ethynyl)trimethylsilane (**4**).

Compound **3** (7 g, 20.24 mmol), bis(triphenylphosphine)palladium(II)dichloride (710 mg, 1.01 mmol), and copper(I)iodide (385 mg, 2.02 mmol) were added to a 100 mL two-neck round bottom flask, equipped with a magnetic stirrer bar. The reaction vessel was evacuated and backfilled with Ar. After then, tetrahydrofuran (40 mL), trimethylsilylacetylene (1.99 g, 20.24 mmol) and triethylamine (12 mL) were added. After 3 hours stirring at room temperature, the reaction mixture was filtered through a silica plug. The concentrated filtrate purified by column chromatography (ethyl acetate (EA)/n-hexane 1:9, v/v) to afford compound **4** as dark brown oil (4.85 g, yield 75.79%). ¹H-NMR (300 MHz, CDCl₃, δ): 8.31 (d, *J* = 6.24 Hz, 1H), 7.38 (d, *J* = 8.19 Hz, 1H), 0.28 (s, 9H)

Synthesis of 1-bromo-4-ethynyl-2-fluoro-5-nitrobenzene (**5**).

Compound **4** (4.8 g, 15.33 mmol), K₂CO₃ (2.33 g, 16.86 mmol), 18-crown-6 (0.41g

1.53 mmol), and a mixed-solvent of dichloromethane (30 mL), H₂O (15 mL), and acetone (7mL) were added to a 100 mL one-neck round bottom flask, equipped with a magnetic stirrer bar. After 2 hours stirring at room temperature, the reaction mixture was poured into H₂O (300 mL), and extracted with dichloromethane. The organic phase was separated, washed with brine (300 mL × 2), dried over MgSO₄, and concentrated, sequentially. The concentrated crude product was purified by column chromatography (ethyl acetate/n-hexane 1:3, v/v) to afford compound **5** as brown powder (2.79 g, yield 75.57%). ¹H-NMR (300 MHz, CDCl₃, δ): 8.36 (d, *J* = 6.24 Hz, 1H), 7.43 (d, *J* = 8.04 Hz, 1H), 3.64 (s, 1H)

Synthesis of 1,2-bis(4-bromo-5-fluoro-2-nitrophenyl)ethyne (**6**).

Compound **6** was synthesized by the same synthetic procedure as compound **4**, using compound **3** (4.80 g, 13.89 mmol), compound **5** (3.39 g, 13.89 mmol), bis(triphenylphosphine)palladium(II)dichloride (487 mg, 0.69 mmol), copper(I)iodide (264 mg, 1.38 mmol), tetrahydrofuran (40 mL), and triethylamine (10mL). Flash column chromatography (chloroform) and methanol washing afforded the compound **6** as a brown solid (2.90 g, yield 45.18%). ¹H-NMR (300 MHz, CDCl₃, δ): 8.47 (d, *J* = 6.18 Hz, 2H), 7.56 (d, *J* = 7.86 Hz, 2H)

Synthesis of 1,2-bis(4-bromo-5-fluoro-2-nitrophenyl)ethane-1,2-dione (**7**).

Potassium permanganate (2.19 g, 13.84 mmol), Adogen 464 (catalytic amount), H₂O (30 mL), dichloromethane (40 mL), and acetic acid (1.5 mL) were added to a 250 mL

two-neck round bottom flask, equipped with a magnetic stirrer bar. The reaction mixture was stirred, and evacuated and backfilled with Ar. After then, compound **6** (2.13 g, 4.64 mmol) was added to reaction mixture. The reaction mixture was gently refluxed for 5 hours, cooled, and decolorized using NaHSO₃, sequentially. The resulting two clear phases were separated, and the yellow organic phase was dried over MgSO₄ and filtered through a silica plug. The yellow filtrate was concentrated, and the resulting solid was washed with methanol to afford compound **7** as a yellow crystalline solid (1.85 g, yield 81.23%). ¹H-NMR (300 MHz, CDCl₃, δ): 8.55 (d, *J* = 5.61 Hz, 2H), 7.4 (d, *J* = 6.93 Hz, 2H)

Synthesis of 2,7-dibromo-3,8-difluoro-5,10-dihydroindolo[3,2-b]indole (**8**).

Compound **7** (1.85 g, 3.74 mmol) and acetic acid (20 mL) were added to a 100 mL two-neck round bottom flask, equipped with a magnetic stirrer bar. With vigorous stirring, the filtrate of stannous chloride (14.87 g, 74.89 mmol), acetic acid (15 mL), and 1 N HCl (15 mL) mixed solution was added to the reaction mixture. The reaction mixture was gently refluxed for 5 hours at 80°C, cooled down to room temperature. After then, the reaction mixture was poured into the 300 mL of H₂O, and extracted with ethyl acetate. The concentrated crude product was purified by flash column chromatography (ethyl acetate /n-hexane 1:2 v/v) and resulting solid was washed with chloroform (100 mL) to afford the compound **8** as dim brown solid (1.23 g, yield 82.10%). ¹H-NMR (300 MHz, Acetone-d₆, δ): 10.47 (s, 2H), 7.84 (d, *J* = 5.88 Hz, 2H), 7.67 (d, *J* = 9.36 Hz, 2H)

Synthesis of 2,7-dibromo-3,8-difluoro-5,10-dihexyl-5,10-dihydroinolo[3,2-b]indole (9).

A 100 mL two-neck round bottom flask, equipped with a magnetic stirrer bar and reflux condenser was baked under reduced pressure and backfilled with Ar. Compound **8** (380 mg, 0.95 mmol), anhydrous tetrahydrofuran (20 mL), and NaH (91.20 mg, 3.79 mmol) were added to the baked reaction vessel. After 10 minutes at room temperature, 1-bromohexane (627 mg, 3.79 mmol) was added to the reaction mixture. After then, the reaction mixture was gently refluxed for 24 hours. After reaction finished, the reaction mixture was poured into brine (200 mL) and extracted with dichloromethane. The organic layer was separated, washed (H₂O), dried with MgSO₄, and concentrated, sequentially. Resulting crude product was purified by flash column chromatography (ethyl acetate /n-hexane 1:4, v/v) and subsequently by recrystallization (EA) to afford compound **9** as white crystalline solid (410 mg, yield 75.94%).

¹H-NMR (300 MHz, THF-d₈, δ): 7.94 (d, *J* = 5.76 Hz, 2H), 7.84 (d, *J* = 9.45 Hz, 2H), 4.62 (t, *J* = 7.08 Hz, 4H), 1.94 (m, *J* = 7.23Hz, 4H), 1.45~1.19 (m, 12H), 0.81 (t, *J* = 7.11 Hz, 6H)

Synthesis of 2H2TIDIDF.

2,7-dibromo-3,8-difluoro-5,10-dihexyl-5,10-dihydroinolo[3,2-b]indole (0.200 g, 0.352 mmol), 2-(tributylstannyl)thiophene (0.276 g, 0.739 mmol), tetrakis(triphenylphosphine)palladium(0) (0.040 g, 0.035 mmol), and toluene (30 mL) were added to a 100 mL two-neck round-bottom flask, equipped with a magnetic stirrer

bar and reflux condenser. The reaction vessel was purged with an Ar, and was gently refluxed at 110 °C. After reaction finished, the reaction mixture was then quenched with H₂O (300 mL) and extracted with dichloromethane (200 mL). The combined organic phase was dried with MgSO₄ and concentrated under reduced pressure. The crude product was purified by flash column chromatography (ethyl acetate/n-hexane 1:1, v/v) and subsequently by recrystallization (ethyl acetate) to afford **2H2TIDIDF** as yellow crystal (0.138 g, 68.2%) ¹H-NMR (500MHz, Tetrahydrofuran-d8,δ): 7.781 (d, *J*=6.5 Hz, 2H), 7.684 (d, *J*=11.5 Hz, 2H), 7.535 (dt, *J*=3.5 Hz, 1.5 Hz 2H), 7.445 (dd, *J*=5 Hz, 1 Hz, 2H), 7.118 (td, *J*=4 Hz, 1 Hz, 2H), 4.569 (t, *J*=7 Hz, 4H), 1.959 (quint., *J*=7.5 Hz, 4H) 1.430 (quint., *J*=8 Hz, 4H) 1.400 ~ 1.251 (m, 8H), 0.842 (t, *J*=7 Hz, 6H), ¹³C NMR (500MHz, Tetrahydrofuran-d8, δ) :155.69, 153.79, 139.90, 139.88, 139.17, 128.85, 128.37, 126.55, 126.51, 126.14, 126.22, 118.36, 118.23, 114.10, 114.02, 109.96, 109.93, 104.93, 104.71, 45.89, 32.72, 31.38, 27.70, 23.59, 14.49, HRMS(FAB, m/z): Calcd. for C₃₄H₃₆F₂N₂S₂: 574.2288, found: 574.2295, Elel. Anal. Calcd. For C₃₄H₃₆F₂N₂S₂: C 71.05, H 6.31, F 6.61, N 4.87, S 11.16; found: C 71.07, H 6.30, N 4.81, S 11.07.

Synthesis of 4H4TIDIDF.

Compound **9** (650 mg, 1.14 mmol), 5'-hexyl-2,2'-bithiophene-5-boronic acid pinacol ester (904 mg, 2.40 mmol), tetrakis(triphenylphosphine)palladium(0) (132 mg, 0.11 mmol), THF (30 mL), and 2 N NaOH aqueous solution (15 mL) were added to a 100 mL two-neck round bottom flask, equipped with a magnetic stirrer bar and reflux

condenser. The reaction mixture was gently refluxed at 80 °C in Ar atmosphere. After 24 hours, the reaction mixture was then quenched with H₂O (300 mL), neutralized (1 N HCl), and extracted with dichloromethane. The combined organic phase was dried with MgSO₄ and concentrated under reduced pressure. The crude product was purified by flash column chromatography (chloroform/n-hexane 1:4, v/v) and subsequently by recrystallization (EA) to afford **4H4TIDIDF** as orange crystal (760 mg, yield 73.23%)
¹H-NMR (300 MHz, Tetrahydrofuran-d8, δ): 7.78 (d, *J* = 6.21 Hz, 2H), 7.69 (d, *J* = 12.03 Hz, 2H), 7.46 (d, *J* = 3.27 Hz, 2H), 7.15 (d, *J* = 3.84 Hz, 2H), 7.07 (d, *J* = 3.51 Hz, 2H), 6.73 (d, *J* = 3.42 Hz, 2H), 4.57 (t, *J* = 6.69 Hz, 4H), 2.82 (t, *J* = 7.5 Hz, 4H), 1.98~1.93 (m, 4H), 1.72~1.65 (m, 4H), 1.43 ~ 1.26 (m, 24H), 0.90 (t, *J* = 6.9 Hz, 6H), 0.84 (t, *J* = 6.93 Hz, 6H). ¹³C NMR (500MHz, Tetrahydrofuran-d8, δ): 155.73, 153.83, 146.13, 139.27, 138.48, 138.45, 138.25, 138.22, 135.95, 129.09, 127.24, 127.20, 126.04, 124.37, 124.14, 118.07, 117.94, 114.01, 113.92, 109.36, 109.33, 104.99, 104.78, 45.98, 32.74, 31.38, 31.01, 29.84, 27.70, 23.64, 23.60, 14.59, 14.52 HRMS(FAB, m/z): Cald. for C₅₄H₆₂F₂N₂S₄: 906.39, found: 906.392. Elel. Anal. Calcd. For C₅₄H₆₂F₂N₂S₄: C 71.48, H 7.11, F 4.19, N 3.09, S 14.13; found: C 71.14, H 7.22, N 3.08, S 13.94

Characterizations

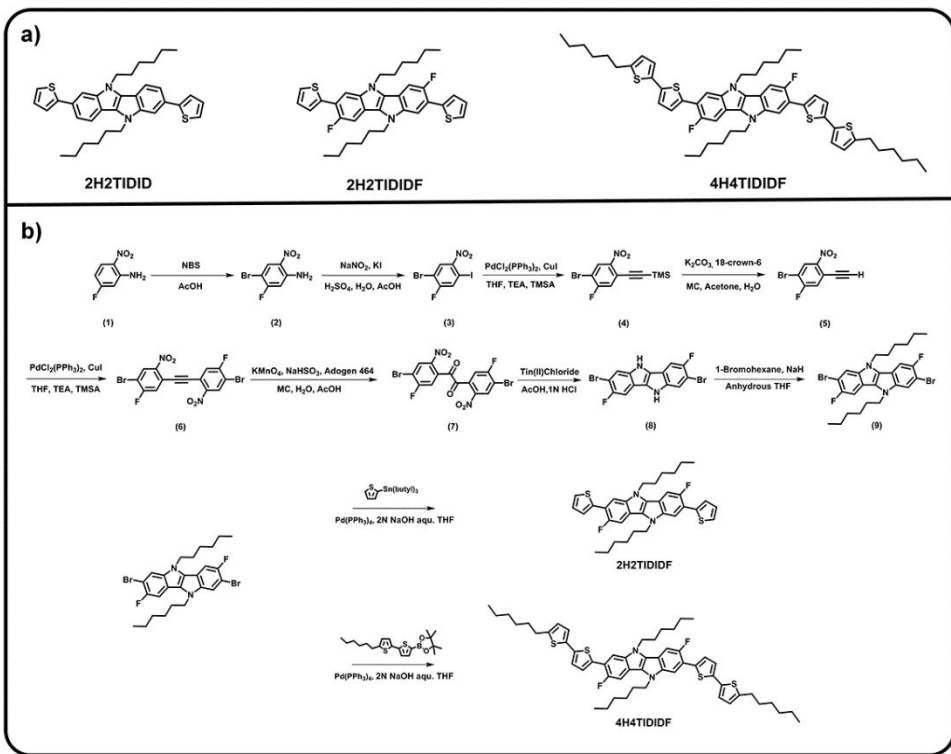
Chemical structures were carefully identified by ¹H NMR (Bruker, Avance-300), ¹³C NMR (Bruker. Avance-500), GC-MASS (JEOL, JMS-700), and elemental analysis

(Flash 2000, Thermo Scientific). Single crystal X-ray crystallographic data was collected by Bruker SMART APEX II X-ray diffractometer and was analyzed by Bruker SHELXTL software. AFM images were obtained by a Bruker Nanoscope III multimode SPM with tapping mode using TREST cantilever. Ground state geometries of all molecules were extracted from single crystal X-ray analysis, and their electrostatic potential map were computed using the B3LYP level of density functional theory (DFT), in which the 6-31+g** basis set was applied. All calculations were carried out using Gaussian 09.

Device Fabrication and Characterization

As a OFET substrate, SiO₂/Si wafer (p-doped 300 nm) was rinsed with acetone and isopropyl alcohol, respectively, for 10 minute in an ultrasonicator, followed by 15 minute UV (360 nm) O₃ treatment. After then, octadecyltrichlorosilane (ODTS) was treated as self-assembled monolayer (SAM) on prepared substrate, to reduce charge trap sites, by vapor phase in a vacuum oven. Aligned organic semiconductor crystal active layers were deposited using dip coating method (4H4TIDIDF concentration of 0.05 wt% in chloroform and n-hexane co-solvent (1:3 v/v), drawing speed of 5μm/s) in air. As source and drain electrode, 50 nm thick of Au was thermally deposited with deposition rate of 0.2 – 0.3 Å s⁻¹. The *I-V* characteristics of all the OFETs were measured in a nitrogen-filled glove box, using a Keithley 4200 SCS instrument connected to a probe station. All OFET characteristics were obtained from the transfer curve in the

saturation regime. For the charge carrier mobility calculations, we checked the channel width and length of the individual crystals on OFET devices were measured by an optical microscope.



Scheme 4-1. a) Molecular structures of target materials; b) Synthetic routes for 2H2TIDIDF and 4H4TIDIDF.

4.3. Results and Discussion

4.3.1. Design and Synthesis

To explore fluorination effect on IDID derivatives in terms of molecular packing structure, among previously synthesized IDID derivatives, 2H2TIDID was selected as a reference molecule; because its crystal structure had been clearly analyzed, and that revealed typical drawbacks as mentioned before. From that molecular analog, hydrogen atoms at 3- and 8- positions of IDID were replaced by F atom (2H2TIDIDF see **Scheme 4-1**), not only to provide intramolecular C-H···F interaction for the conformational locking, but also to rearrange their electron density for efficient π - π interaction. The synthetic procedure of 2,7-dibromo-3,8-difluoro-5,10-dihexyl-5,10-dihydroinolo[3,2-b]indole was described in **Experimental** section, and from that intermediate, 2H2TIDIDF was successfully synthesized by Stille coupling reaction. Detailed synthetic procedure and characterization results were described in **Experimental** section.

4.3.2. Single Crystal Packing and Analysis

Through the slow solvent evaporation method (ethyl acetate), needle-type 2H₂TIDIDF single crystals (hexagonal for 2H₂TIDID) were obtained, and that of 2H₂TIDIDF molecules crystallized in space group of P-1 of the triclinic with unit cell dimensions of $a = 5.5460 (10)$ Å, $b = 15.7261 (3)$ Å, $c = 17.4158 (3)$ Å, $\alpha = 80.9410 (10)^\circ$, $\beta = 87.1990 (10)^\circ$, and $\gamma = 80.8540 (10)^\circ$ (see **Table 4-1**). As shown in **Figure 4-1a** to **c**, different from 2H₂TIDID case (i.e., slipped herringbone motif, torsion angle of 35.32° between outer benzene ring of IDID core and neighboring thiophene, and conformationally disordered conjugate backbone, see **Figure 4-1d** and **e**, 2H₂TIDIDF crystal exhibited slipped π-stack and planarized π-conjugated backbone, and also, unit cell consisted of two different conformers having different conformation of *N*-aliphatic side chains. Notably, 2H₂TIDIDF was much more densely packed than 2H₂TIDID (packing density of 1.289 g cm⁻³ for 2H₂TIDIDF and 0.612 g cm⁻³ for 2H₂TIDID) in their crystal. α-conformer exhibited torsion angle of 11.1° between outer benzene ring of IDIDF core and neighboring thiophene, and their C-H···F distance was found to be 2.244 Å. While β-conformer exhibited torsion angle of 18.58° between outer benzene ring of IDIDF core and neighboring thiophene, and their C-H···F distance was found to be 2.324 Å. In case of F atom of β-conformer exhibited additional intermolecular C-H···F interaction with hydrogen atom on aliphatic side chains of α-conformer (distance

of 2.560 Å). Two conformers stacked toward a-axis, and the estimated π - π distance was 3.23 Å for α -stack and 3.39 Å for β -stack; their pitch and roll angle which were measured by reported method were described in **Figure 4-1**.^[26] According to the reported literature,^[25] it was conclude that 2H2TIDIDF exhibited strong inter- and intramolecular C-H···F interactions. However, because F atoms in β -conformer exhibited multiple C-H···F interaction, torsion angle and C-H···F distance of β -conformer were slightly larger than those of α -conformer. Furthermore, electron density on its π -plane should be higher than those of α -conformer, owing to electron-withdrawing effect of F atom would be attenuated by multiple C-H···F interactions. Therefore, presumably, β -stack exhibited longer π - π distance than that of α -stack.

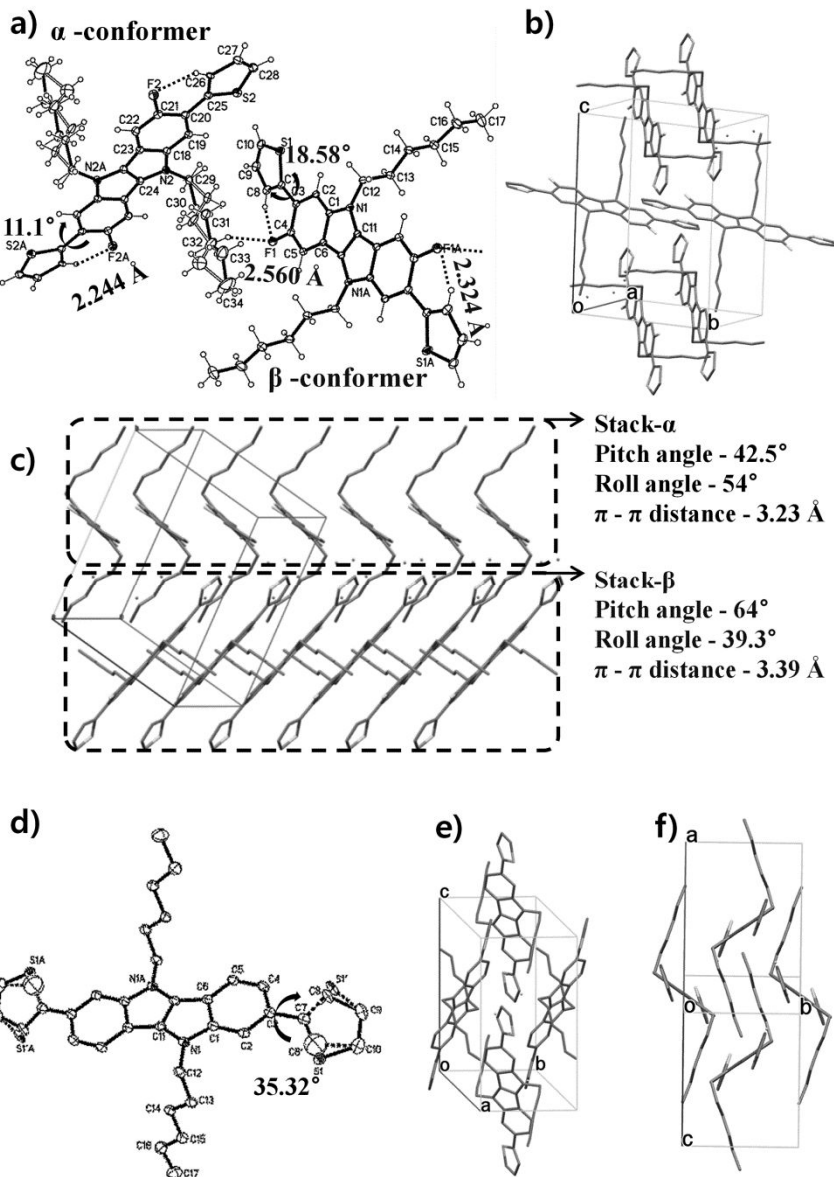


Figure 4-1. Crystal structures of 2H2TIDIDF (a to c) and 2H2TIDID (d to f). (For the clear identification, hydrogen atoms of the molecules are expelled in images on b, c, d, e, and f).

Table 4-1. Crystal data and structure refinement for 2H2TIDIDF.

Empirical formula	C34 H36 F2 N2 S2
Formula weight	574.77
Temperature	172(2) K
Wavelength	0.71073 Å
Crystal system	Triclinic
Space group	P -1
Unit cell dimensions	a = 5.54600(10) Å b = 15.7261(3) Å c = 17.4158(3) Å
Volume	1480.49(5) Å ³
Z	2
Density (calculated)	1.289 Mg/m ³
Absorption coefficient	0.219 mm ⁻¹
F(000)	608
Crystal size	0.650 x 0.160 x 0.140 mm ³
Theta range for data collection	1.184 to 28.255°.
Index ranges	-7<=h<=7, -20<=k<=20, -23<=l<=23
Reflections collected	27684
Independent reflections	7318 [R(int) = 0.0307]
Completeness to theta = 25.242°	99.8 %
Absorption correction	Semi-empirical from equivalents
Max. and min. transmission	0.7457 and 0.6655
Refinement method	Full-matrix least-squares on F ²
Data / restraints / parameters	7318 / 0 / 388
Goodness-of-fit on F ²	1.032
Final R indices [I>2sigma(I)]	R1 = 0.0600, wR2 = 0.1808
R indices (all data)	R1 = 0.0732, wR2 = 0.1952
Extinction coefficient	n/a

4.3.3. Charge Distribution and Impact on Crystal packing

To obtain in-depth understanding of the F atom substitution effect on crystal packing nature alteration, electrostatic potential (ESP) map of two IDID derivatives were calculated, because the ESP is considered as an efficient tool for the understanding of the non-covalent interactions of organic molecules, and also, it is widely used for visualization of charge distribution on organic molecules.^[27,28] As shown in **Figure 4-2** a to c, for 2H2TIDID (**Figure 4-2a**), negative potential was delocalized on the π -plane, especially outer benzene rings and thiophenes, and periphery of the π -plane showed positive potential, mainly due to abundant π -electron and low electronegativity of hydrogen atom. While, for both 2H2TIDIDF conformers (**Figure 4-2b** and c), negative potential was mainly located around intramolecular C-H \cdots F interaction position, and the rest of periphery of the π -plane showed positive potential. Furthermore, electron density on their π -plane was dramatically reduced than that of 2H2TIDID. Through this ESP calculation results, I could conclude as follows; i) Slipped herringbone packing nature of 2H2TIDID is driven by central *N*-aliphatic side chains and strong electrostatic repulsion force toward π -stacking direction, ii) F atom substitution into IDID core give rise to strong local dipole moment on their planarized π -plane, and reduces electrostatic repulsion force toward π -stacking direction. Therefore, 2H2TIDIDF molecules adopt π - π stacking motif, as shown in **Figure 4-2d** and e, each

dimers showed efficient Coulombic interaction with similar molecular alignments. However, because of the central *N*-aliphatic chains, molecules stacked slipped manner, and the different pitch- and roll-angle between two conformers were most probably due to their subtle difference of electron density. In brief, when F atom substituted into the IDID core, abundant electron density on its π -plane is dramatically reduced and localized at F atoms, and therefore strong local dipole is induced. Furthermore, intramolecular C-H \cdots F interaction with hydrogen atom in neighboring thiophene give rise to π -conjugated backbone planarization with conformational locking. To this end, attributing beneficially modulated Coulombic force and π -conjugated structure, fluorinated IDID derivatives could have packing motif of slipped π - π stacking.

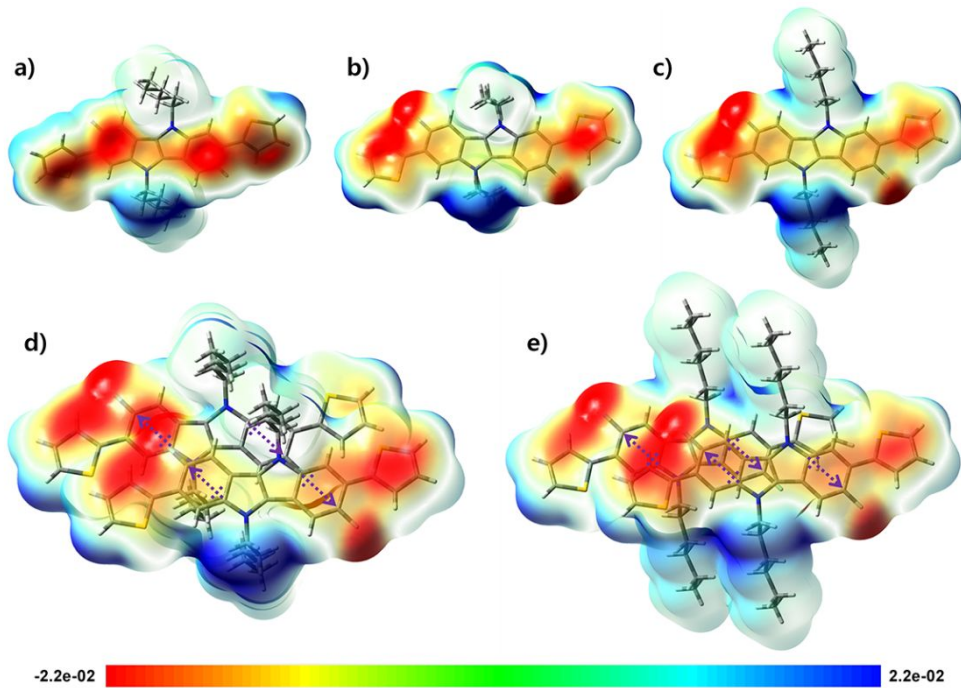


Figure 4-2. Electrostatic potential maps; (a) 2H2TIDID, (b) 2H2TIDIDF _{α} -conformer, (c) 2H2TIDIDF _{β} -conformer, (d) 2H2TIDIDF-dimer _{α} -conformer, (e) 2H2TIDIDF-dimer _{β} -conformer.

4.3.4. Single Crystal Device

4.3.4.1. Molecular Design and Synthesis

On the basis of aforementioned fluorination effect on crystal engineering, F atom was introduced into the 4H4TIDID (**Scheme 2-1**), exhibiting excellent p-type OFET characteristic and versatile processability, to realize high performance SC OFET. As shown in **Scheme 4-1**, from the intermediate compound 9, 2,7-dibromo-3,8-difluoro-5,10-dihexylindolo[3,2-b]indole, 4H4TIDIDF was successfully synthesized by Suzuki-Miyaura cross coupling. Newly synthesized molecule, 4H4TIDIDF, exhibited acicular crystal habit, and are highly soluble in common organic solvents such as tetrahydrofuran, chloroform, and dichloromethane. Molecular structure was carefully characterized by ^1H NMR, ^{13}C NMR, elemental analysis, and mass analysis. Detailed synthetic procedure is described in section 4-2 **Experimental** section.

4.3.4.2. Crystal Structure Analysis and Charge Distribution.

To fully elucidate molecular conformation and packing motif of 4H4TIDIDF in solid state, the SC XRD analysis was performed (See **Figure 4-3** and **Table 4-2**). As for the molecular conformation, 4H4TIDIDF exhibited almost planar conformation with a

torsion angle of 10.45° between fluorinated IDID core and neighboring thiophene, and a torsion angle of 0.98° between two thiophenes. More importantly, as similar as 2H2TIDIDF, F···H distance between fluorinated IDID core and neighboring thiophene is found to be 2.276 \AA , which is less than the sum of the van der Waals radii of the fluorine and the hydrogen (= about 2.67 \AA). Thus, such strong intramolecular interaction of C-F···H is one of the key factors reducing a distortion between IDID core and the neighbored thiophene and enhancing a planarity of the elongated molecule. This may enable 4H4TIDIDF to successfully build the single crystal. In contrast, for the 4H4TIDID, single crystal could not obtain for identifying the molecular packing in the previous study. With this planar structure, 4H4TIDIDF crystallized in space group of P-1 of the triclinic with unit cell dimensions of $a = 5.5351(1)\text{ \AA}$, $b = 13.7138(2)\text{ \AA}$, $c = 17.7912(3)\text{ \AA}$, $\alpha = 68.191(1)^\circ$, $\beta = 82.836(1)^\circ$, and $\gamma = 80.889(1)^\circ$ (see **Table 4-2**). As shown in **Figure 4-3d**, 4H4TIDIDF molecules stacked toward a-axis with slipped π -stacking motif, and the estimated π - π distance was 3.480 \AA . Interestingly, 4H4TIDIDF has multiple short contacts with the neighboring 8 molecules, and beside π - π contacts (3.362 \AA for C-C), all of four aliphatic side chains of 4H4TIDIDF participate in intermolecular interaction with short contacts (2.388 \AA and 2.312 \AA for H-H and 2.985 \AA for S-H, see **Figure 4-3e**), giving rise to a rigid and stable crystalline networks. On the basis of SC analysis result, ESP calculation of 4H4TIDIDF was conducted, and result was well corresponded to aforementioned result, i.e., 4H4TIDIDF also exhibited elongated planar π -conjugated backbone structure with

localized charge density, packing motif of slipped π -stack, and the packing density of 1.220 g cm⁻³, owing to strong H···F intramolecular interaction and strong intermolecular Coulombic interaction (see **Figure 4-3b**).

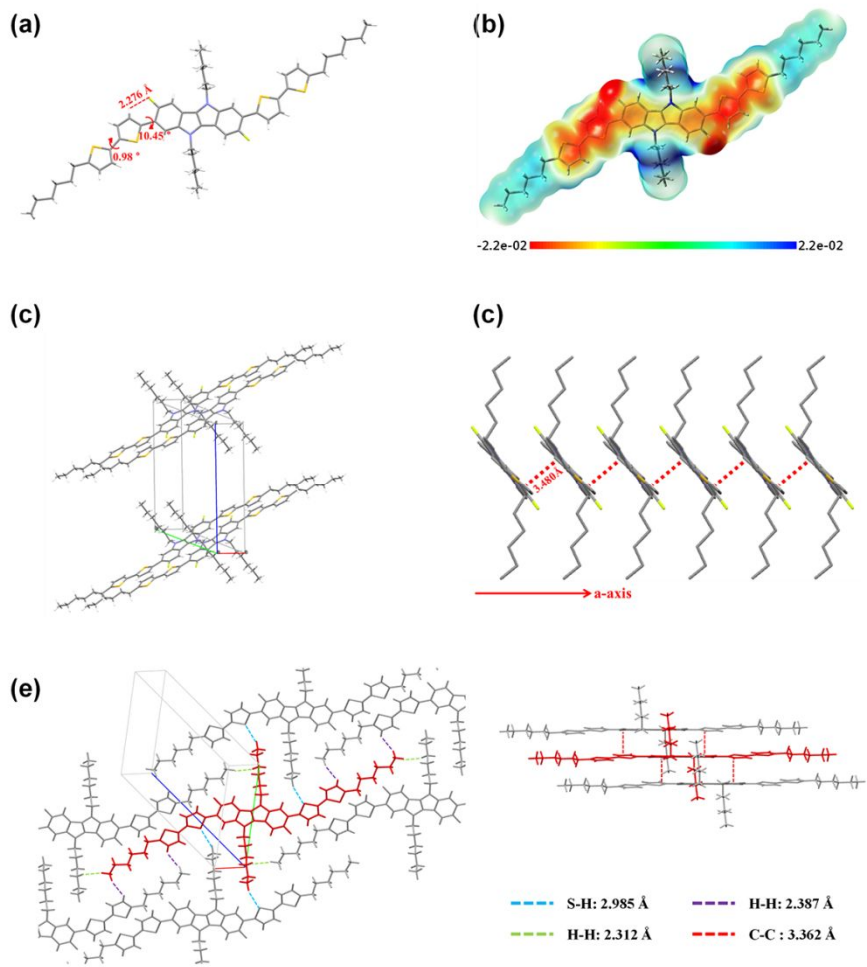


Figure 4-3. Single Crystal Structure and electrostatic potential map of 4H4TIDIDF.

Table 4-2. Crystal data and structure refinement for 4H4TIDIDF.

Empirical formula	C27 H32 F N S2
Formula weight	453.66
Temperature	296(1) K
Wavelength	0.71073 Å
Crystal system	Triclinic
Space group	P-1
Unit cell dimensions	a = 5.53520(10) Å b = 13.7138(2) Å c = 17.7912(3) Å
Volume	1234.83(4) Å ³
Z	2
Density (calculated)	1.220 Mg/m ³
Absorption coefficient	0.237 mm ⁻¹
F(000)	484
Crystal size	0.38 x 0.12 x 0.05 mm ³
Theta range for data collection	1.24 to 28.35°
Index ranges	-7<=h<=7, -16<=k<=18, 0<=l<=23
Reflections collected	6148
Independent reflections	6148 [R(int) = 0.0000]
Completeness to theta = 28.35°	99.4 %
Absorption correction	Multi-scan
Max. and min. transmission	0.9882 and 0.9152
Refinement method	Full-matrix least-squares on F ²
Data / restraints / parameters	6148 / 6 / 280
Goodness-of-fit on F ²	1.084
Final R indices [I>2sigma(I)]	R1 = 0.0756, wR2 = 0.2440
R indices (all data)	R1 = 0.1261, wR2 = 0.2884
Largest diff. peak and hole	0.619 and -0.462 e.Å ⁻³

4.3.4.3. OFET device

To explore inherent charge transport property of 4H4TIDIDF, electrical characteristics was evaluated by fabricating SC-OFET device. Because 4H4TIDIDF has versatile processabilty with high solubility, SC-OFET device was fabricated using dip-coating method affording large-area and well-aligned micro structures; that have practical advantages in developing transistor arrays for integrated circuits.^[29,30] As shown in **Figure 4-4**, well aligned ribbon type micro-crystals of 4H4TIDIDF was successfully obtained. Micro-crystals were well aligned toward pulling direction, and atomic force microscope (AFM) topography revealed that aligned crystals exhibited width of $2 \sim 3 \mu\text{m}$, and were constructed by multi-layered crystalline sheets, i.e., terrace like structure. The SC-OFET device was fabricated bottom-gate top-contact (BGTC) device architecture. 4H4TIDIDF SCs were deposited by dip-coating method, directly on the octadecyltrichlorosilane (ODTS) treated SiO_2/Si substrates, and 50 nm of source and drain electrode (Au) was deposited by thermal deposition in vacuum. Detailed conditions were described in section 4-2 **Experimental** section. As shown in **Figure 4-5**, 4H4TIDIDF SC-OFET devices exhibit typical p-type transfer and output characteristics. The highest mobility was measured to be $1.88 \text{ cm}^2 \text{ V}^{-1} \text{ s}^{-1}$, and the averaged mobility of 10 devices was $0.61 \text{ cm}^2 \text{ V}^{-1} \text{ s}^{-1}$ with on-off ratio of 1×10^5 and threshold voltage of -13V.

To obtain a deeper insight into the charge transport of 4H4TIDIDF in terms of molecular orientation, out-of-plane X-ray diffraction (XRD) measurement of the 4H4TIDIDF SC OFET device was conducted. As shown in **Figure 4-6a**, the XRD pattern exhibited strong diffraction at 2 θ degree of 7.1° corresponding to (0, 1, 1) diffraction of single crystal analysis data; this indicates that 4H4TIDIDF molecules oriented on substrate with edge-on manner, and their extended and planar π -plane stacked toward substrate parallel direction favorable for efficient charge carrier transport in field-effect transistor architecture (see **Figure 4-6b**). In short, attributing dense and favorably oriented molecular arrangement, such high transistor mobility could be obtained.

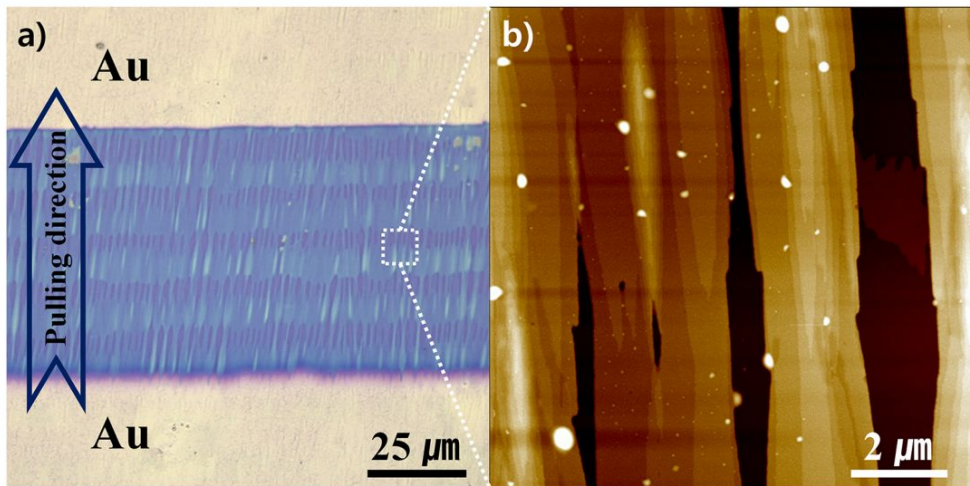


Figure 4-4. Optical microscope (OM) image of 4H4TIDIDF dip-coating device (a), and atomic force microscope (AFM) height image of 4H4TIDIDF micro-crystals (b).

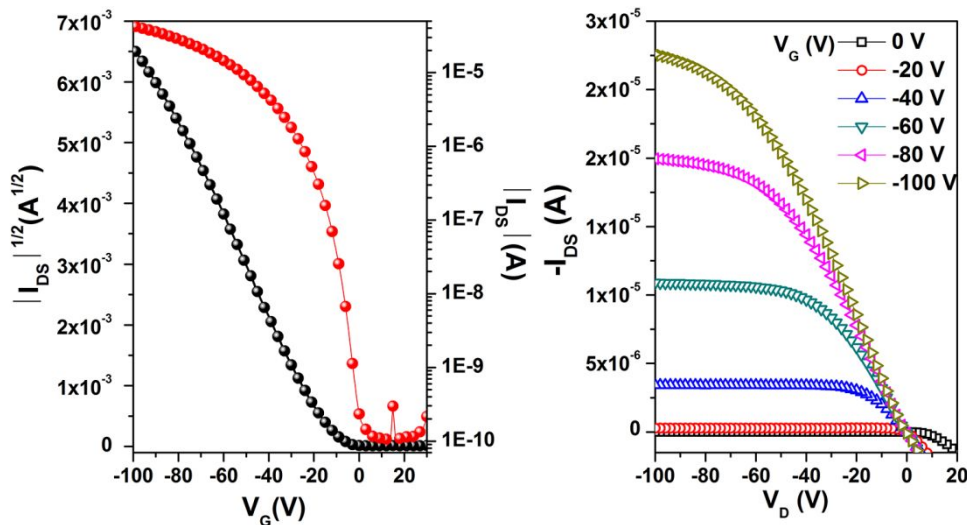


Figure 4-5. Single crystal OFET characteristics of 4H4TIDIDF. a) Transfer curve; b) Out-put curve.

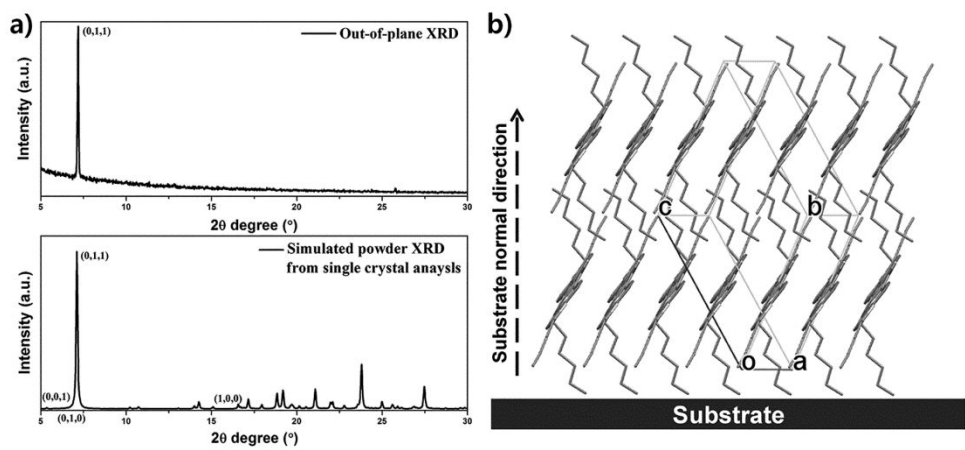


Figure 4-6. (a) Out-of-plane XRD of 4H4TIDIDF SC device (up) and simulated powder XRD from single crystal analysis data of 4H4TIDID (b) Molecular packing structure of 4H4TIDIDF for SC device.

4.4. Conclusion

In conclusion, fluorinated IDID derivatives have designed and synthesized not only to develop effective strategy for the crystal engineering, but also to realize high performance SC-OFET. It was found that the substitution of F atom into IDID core gave rise to planar and extended π -conjugated backbone structure, strong Coulombic force toward π - π stacking, and compact 1D crystal for their derivatives. As a consequence, 4H4TIDIDF for which hydrogen atoms at 3- and 8-position of IDID in 4H4TIDID were replaced by F atom, exhibited excellent p-type field-effect mobility of $1.88 \text{ cm}^2 \text{ V}^{-1} \text{ s}^{-1}$ in SC OFET device, with packing structure of slipped π -stack.

4.5. Reference

- [1] V. Coropceanu, J. Cornil, D. A. da S. Filho, Y. Olivier, R. Silbey, J.-L. Bredas, *Chem. Rev.* **2007**, *107*, 926.
- [2] C. Wang, H. Dong, W. Hu, Y. Liu, D. Zhu. *Chem. Rev.* **2012**, *112*, 2208.
- [3] A. R. Murphy, J. M. J. Fréchet, *Chem. Rev.* **2007**, *107*, 1066.
- [4] H. Dong, X. Fu, J. Liu, Z. Wang, W. Hu, *Adv. Mater.* **2013**, *25*, 6158.
- [5] R. Li, W. Hu, Y. Liu, D. Zhu, *Acc. Chem. Res.* **2010**, *43*, 529.
- [6] J. -L. Brédas, G. B. Street, *Acc. Chem. Res.* **1985**, *18*, 309
- [7] J. -L. Brédas, D. Beljonne, V. Coropceanu, J. Cornil, *Chem. Rev.* **2004**, *104*, 4971
- [8] J. E. Anthony, J. S. Brooks, D. L. Eaton, S. R. Parkin, *J. Am. Chem. Soc.* **2001**, *123*, 9482
- [9] M. M. Payne, S. R. Parkin, J. E. Anthony, C.-C. Kuo, T. N. Jackson, *J. Am. Chem. Soc.* **2005**, *127*, 4986
- [10] J. E. Anthony, D. L. Eaton, S. R. Parkin, *Org. Lett.* **2002**, *4*, 15
- [11] C. D. Sheraw, T. N. Jackson, D. L. Eaton, J. E. Anthony, *Adv. Mater.* **2003**, *15*, 2009
- [12] S. Subramanian, S. K. Park, S. R. Parkin, V. Podzorov, T. N. Jackson, J. E. Anthony, *J. Am. Chem. Soc.* **2008**, *130*, 2706.

- [13] H. Moon, R. Zeis, E.-J. Borkent, C. Besnard, A. J. Lovinger, T. Siegrist, C. Kloc, Z. Bao, *J. Am. Chem. Soc.* **2004**, *126*, 15322.
- [14] M. Wang, J. Li, G. Zhao, Q. Wu, Y. Huang, W. Hu, X. Gao, H. Li, D. Zhu, *Adv. Mater.* **2013**, *25*, 2229.
- [15] D.-H. Dou, Y.-Q. Zheng, Z.-F. Yao, Z.-A Yu, T. Lei, X. Shen, X.-Y Luo, J. Sun, S.-D. Zhang, Y.-F Ding, G. Han, Y. Yi, J.-Y. Wang, J. Pei, *J. Am. Chem. Soc.* **2015**, *137*, 15947.
- [16] N. Blouin, A. Michaud, M. Leclerc, *Adv. Mater.* **2007**, *19*, 2295.
- [17] H. Uoyama, K. Goushi, K. Shizu, H. Nomura, C. Adachi, *Nature*. **2012**, *492*, 234.
- [18] P.-L. T. Boudreault, S. Wakim, N. Blouin, M. Simard, C. Tessier, Y. Tao, M. Leclerc, *J. Am. Chem. Soc.* **2007**, *129*, 9125.
- [19] T. V. Pho, J. D. Yuen, J. A. Kurzman, B. G. Smith, M. Miao, W. T. Walker, R. Seshadri, F. Wudl, *J. Am. Chem. Soc.* **2012**, *134*, 18185.
- [20] H. Jiang, H. Zhao, K. K. Zhang, X. Chen, C. Kloc, W. Hu, *Adv. Mater.* **2011**, *23*, 5075.
- [21] K. S. Park, S. M. Salunkhe, I. Lim, C.-G. Cho, S.-H. Han, M. M. Sung, *Adv. Mater.* **2013**, *25*, 3351.
- [22] Y. Guo, H. Zhao, G. Yu, C. Di, W. Liu, S. Jiang, S. Yan, C. Wang, H. Zhang, X. Sun, X. Tao, Y. Liu, *Adv. Mater.* **2008**, *20*, 4835.

- [23] G. Zhao, H. Dong, H. Zhao, L. Jiang, X. Zhang, J. Tan, Q. Meng, W. Hu, *J. Mater. Chem.* **2012**, *22*, 4409.
- [24] I. Cho, S. K. Park, B. Kang, J. W. Chung, J. H. Kim, K. Cho, S. Y. Park, *Adv. Funct. Mater.* DOI: 10.1002/adfm.201505023.
- [25] K. Reichembächer, H. I. Süss, J. Hulliger, *Chem. Soc. Rev.* **2005**, *34*, 22.
- [26] M. D. Curtis, J. Cao, J. W. Kampf, *J. Am. Chem. Soc.* **2004**, *126*, 4318.
- [27] S. E. Wheeler, *J. Am. Chem. Soc.* **2011**, *133*, 10262.
- [28] J.-H. Dou, Y.-Q. Zheng, Z.-F Yao, T. Lei, X. Shen, X.-Y. Luo, Z.-A. Yu, S.-D. Zhang, G. Han, Z. Wang, Y. Yi, J.-Y. Wang, J. Pei, *Adv. Mater.* **2015**, *27*, 8051.
- [29] H. Li, B. C-K. Tee, J. J. Cha, Y. Cui, J. W. Chung, S. Y. Lee, Z. Bao, *J. Am. Chem. Soc.* **2012**, *134*, 2760.
- [30] J. Jang, S. Nam, K. Im, J. Hur, S. N. Cha, J. Kim, H. B. Son, H. Suh, M. A. Loth, J. E. Anthony, J.-J. Park, C. E. Park, J. M. Kim, K. Kim, *Adv. Funct. Mater.* **2012**, *22*, 1005

Chapter 5.

Fluorinated Indolo[3,2-b]indole-Based Crystalline Hole Transporting Material for Highly Efficient Perovskite Solar Cells

5.1. Introduction

Inorganic/organic lead halide perovskite solar cells (PSCs) have attracted significant attention due to their advantages such as low-cost fabrication, light-weight, flexibility and high performance, already surpassing a power conversion efficiency (PCE) of 20%.^[1-6] Among various device architectures, high efficiencies have been achieved in a n-i-p type “bilayered” structure employing a perovskite layer as a light absorber atop of mesoporous (mp)-TiO₂ scaffold as a n-type selective contact and hole transporting material (HTM).^[5]

In this device configuration, an ideal HTM in perovskite solar cells requires a well-matched highest occupied molecular orbital (HOMO) level with the valence band of the perovskite for a hole injection and a high mobility for a hole extraction without recombination.^[7,8] To date, several attempts have been made to develop best-performing class of HTMs by incorporating ethylenedioxythiophene, cruciform oligothiophene, fused thiophene, pyrene, quinolizino acridine, and triptycene as a good p-type unit into molecular core structure.^[9-13] Despite such efforts, so far, triarylamine-

based HTMs including 2,2',7,7'-tetrakis(*N,N*-di-p-methoxyphenylamine)-9,9'-spirobifluorene (p,p-spiro-OMeTAD) and polytriarylamine (PTAA) have been considered to be most effective for facilitating hole extraction and preventing electron leakage from the perovskite layer toward the electrode.^[7,8] Very recently, spiro-OMeTAD derivatives offered a superior performance to that using p,p-spiro-OMeTAD by simply modifying a position of the methoxy substituents or introducing a fluorene-dithiophene into spirobifluorene core.^[14-16]

Recently, as a similar p-type analogue to triarylamine, pyrrole-containing heteroacene HTMs based on carbazole, indolocarbazole and fused indoles have been extensively investigated because of their interesting features;^[17-20] a low cost of carbazole and its derivatives, a low redox potential by strong electron donating property, a good chemical-environmental stability by full aromaticity, and a molecular structural variation by introduction of alkyl groups or functional groups into the nitrogen atom or the outer benzene that allows for a tuned electronic property, a controllable solubility and a controllable molecular packing. For example, star-shaped triazatruxene derivative containing three indole units combined by one benzene was utilized as a HTM in perovskite solar cells, exhibiting a remarkable PCE over 18% that is superior to that obtained by p,p-spiro-OMeTAD.^[20] Recently, indolo[3,2-b]indole(IDID)-based π-conjugated p-type semiconductors have been attempted to be exploited in organic light-emitting diode (OLED), organic field-effect transistor (OTFT), and organic photovoltaics (OPV).^[21-24] In the course of my investigation about IDID, it was found

that the IDID has high potential as p-type backbone unit with its well-designed molecular structure (**Chapter 2**, 4H4TIDID), exhibiting an outstanding hole mobility of $0.97 \text{ cm}^2 \text{ V}^{-1} \text{ s}^{-1}$ in a vacuum-deposited (VD) crystalline film and versatile processability. However, the solution-processed spin-coated film showed a somewhat lower hole mobility ($0.18 \text{ cm}^2 \text{ V}^{-1} \text{ s}^{-1}$) than that of VD device, thereby requiring more optimization with respect to the molecular structure for a better molecular packing upon aggregation from the concentrated solution. In fact, this is crucial for its use as high performance HTM in PSCs.

In this regard, 4H4TIDIDF (shown in **Figure 5-1a**) which exhibited excellent p-type field-effect mobility of $1.88 \text{ cm}^2 \text{ V}^{-1} \text{ s}^{-1}$ from single crystal OFET device with high solubility was investigated for p-type HTM for PSCs. Its optoelectronic and electrochemical properties were characterized. With respect to the hole mobility of sandwich-type device, HOMO energy level, and hole collection capability at the perovskite/HTM, 4H4TIDIDF showed a better performance, when compared with p,p-Spiro-OMeTAD. As a result, I and coworker could demonstrate 4H4TIDIDF as a best-performing class of HTMs for PSCs by achieving a high efficiency of 19%.

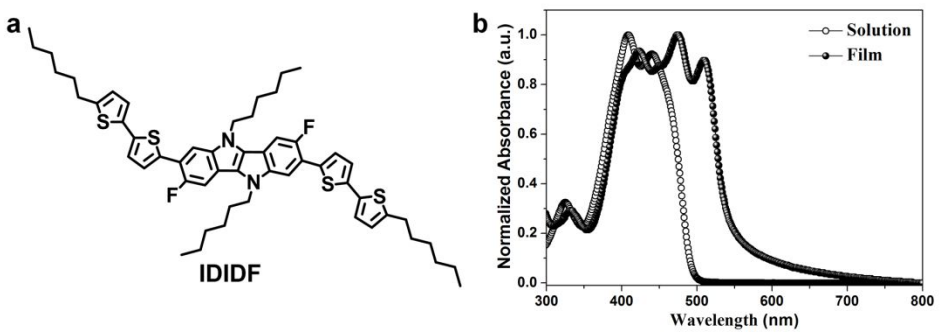


Figure 5-1. (a) Molecular structure of 4H4TIDIDF. (b) UV-vis absorption spectra of 4H4TIDIDF in solution (tetrahydrofuran, 1×10^{-5} M) and film state.

5.2. Experimental

Synthesis

The 4H4TIDIDF was synthesized according to the procedure shown in **Scheme 4-1**.

Synthesis of 4H4TIDIDF was described in **chapter 4**.

Characterizations

Chemical structures were fully identified by ^1H NMR (Bruker, Avance-300), ^{13}C NMR (Bruker, Avance-500), GC-MASS (JEOL, JMS-700), and elemental analysis (Flash 2000, Thermo Scientific). UV-vis spectra were recorded on a SMIMADZU UV-1650PC. Solution absorption spectra were obtained with the concentration of 1.0×10^{-5} M in THF, and film absorption spectra were obtained with spin-coated sample on quartz substrate (using 1 wt% in CHCl₃, 1500rpm/60s). The out-of-plane XRD analysis was carried out using a Bruker D8-Advance X-ray diffractometer. Single crystal X-ray crystallographic data was collected by Bruker SMART APEX II X-ray diffractometer and was analyzed by Bruker SHELXTL software. HOMO energy level of the compound was obtained from the cyclic voltammetry measurement. Cyclic voltammetry measurement was performed using a 273A (Princeton Applied Research) with an one-compartment electrolysis cell consisting of a ITO patterned glass working-electrode, a platinum wire counter-electrode, and a quasi Ag⁺/Ag electrode as reference.

Measurement was performed in an acetonitrile solution with 0.1 M tetrabutylammonium tetrafluoroborate as the supporting electrolyte, at a scan rate of 50 mV/s. Oxidation potential was calibrated using ferrocene as a reference. HOMO energy level of p,p-Spiro-OMeTAD and 4H4TIDIDF were evaluated from the equation of $\text{HOMO} = -(4.8 + (\text{V}_{\text{ox}} - \text{V}_{\text{ferro}}))$, in which V_{ox} is onset position of sample oxidation scan, V_{ferro} is onset position of ferrocene oxidation scan, and the LUMO energy level was evaluated from the HOMO energy level and the solid-state optical energy bandgap, which was obtained from the edge of absorption spectra. Hole mobilities were measured using the space-charge-limited-current (SCLC) model with hole-only device utilizing the configuration of indium tin oxide (ITO)/ Poly(3,4-ethylenedioxythiophene)-polystyrene sulfonate (PEDOT:PSS)/p,p-Spiro-OMeTAD or IDIDF (with Li-bis(trifluoromethanesulfonyl) imide (Li-TFSI) and 4-*tert*-butylpyridine (*t*BP) as additives) /Au. Hole mobility was determined from equation (1):

$$J = \frac{9}{8} \varepsilon_0 \varepsilon_r \mu \frac{V^2}{L^3} \quad (1)$$

In which ε_0 is the permittivity of free space, ε_r is the dielectric constant of the organic semiconductor material (herein ε_r was assumed to be 3 that typical value for organic semiconducting material), μ is the zero-field hole mobility, V is effective voltage with the equation of $V = V_{\text{appl}} - V_{\text{bi}} - V_r$ (V_{appl} : applied bias, V_{bi} : the built in potential due to the difference in electrical contact work function, V_r : the voltage drop due to contact resistance and series resistance across the electrodes) and L is the

thickness of active layer. The evaluated hole mobilities of p,p-Spiro-OMeTAD and IDIDF with Li-bis(trifluoromethanesulfonyl) imide (Li-TFSI) and 4-*tert*-butylpyridine (*t*BP) as additives are 2.17×10^{-4} and 1.69×10^{-3} , respectively.

Device Fabrication and Characterization

F-doped SnO₂ (FTO, Pilkington, TEC8) substrate was cleaned in an ultrasonic bath containing detergents for 30 min and then a dense blocking layer of TiO₂ (60 nm, bl-TiO₂) was deposited onto the FTO by spray pyrolysis using a 20 mM titanium diisopropoxide bis(acetylacetone) solution (Aldrich) at 450 °C. A 100-nm thin mesoporous (mp)-TiO₂ was spin-coated on top of the bl-TiO₂/FTO substrate at 1000 rpm for 50 s using home-made TiO₂ (~ 50 nm in particle size) pastes. Where, the pristine paste had been diluted in 2-methoxyethanol (1g / 5mL), and calcinated at 500 °C for 1 h in air which led to a thickness of about 100 nm. The (FAPbI₃)_{0.92}(MAPbBr₃)_{0.08} perovskite solutions with small excess of PbI₂ were then coated onto the mp-TiO₂/bl-TiO₂/FTO substrate heated to 50°C by two consecutive spin-coating steps, at 1000 and 5000 rpm for 5 s and 10 s, respectively. During the second spin-coating step, 1 mL ethyl ether was poured onto the substrate. The 1.05M solution for (FAPbI₃)_{0.92}(MAPbBr₃)_{0.08} perovskite was obtained by dissolving NH₂CH=NH₂I (=FAI) and CH₃NH₃Br(=MABr) with PbI₂ and PbBr₂ in *N*-*N*-dimethylformamide(=DMF) and dimethylsulfoxide(=DMSO) =(6 : 1 v/v). Then the

perovskite deposited substrate was dried on a hot plate at 150 °C for 10 min. A *p,p*-spiro-OMeTAD /chlorobenzene (30mg/1ml) solution with an additive of 21.5 μ l Li-bis(trifluoromethanesulfonyl) imide (Li-TFSI)/acetonitrile (170 mg/1 ml) and 21.5 μ l 4-*tert*-butylpyridine (TBP)/acetonitrile (1ml/1ml) was spin-coated on (FAPbI₃)_{0.92}(MAPbBr₃)_{0.08}/mp-TiO₂/bl-TiO₂/FTO substrate at 3000 rpm for 30 s. By following the same procedure, 4H4TIDIDF was deposited. Finally, Au counter electrode was deposited by thermal evaporation. The active area of this electrode was fixed at 0.16 cm². The cross section of the perovskite films were investigated using FE-SEM (Tescan Mira 3 LMU FEG). The absorption spectra were obtained using a UV-visible spectrophotometer (Shimadzu UV 2550) in the wavelength range of 300 nm to 850 nm. The photovoltaic properties of the devices were measured using a solar simulator (Newport, Oriel Class A, 91195 A) with a source meter (Keithley 2420) at AM 1.5 G 100 mAc m⁻² of illumination and a calibrated Si-reference cell certificated by NREL. The *J*–*V* curves of all the devices were measured by masking the active area using a metal mask with an area of 0.0955 cm². The external quantum efficiency (EQE) was measured using a power source (Newport 300 W Xenon lamp, 66920) with a monochromator (Newport Cornerstone 260) and a multimeter (Keithley 2001). The ionization energy for the mixed perovskite film on fused silica was measured using photoelectron spectroscopy (Riken Keiki AC-2).

5.3. Results and Discussion

5.3.1. Optical and Electrochemical Properties

Figure 5-1b displays UV-vis absorption spectra of 4H4TIDIDF in solution and in film state. In solution state, the $\pi-\pi^*$ transition of the absorption band was observed at 440 nm, whereas in film state, the corresponding $\pi-\pi^*$ transition was found at 510 nm. As compared to that in solution, a large bathochromic shift of the absorption spectra in film is clearly observed. In association with this shift, the solution-processed film with a good transparency exhibited apparently crystalline nature (See **Figure 5-2**), which is totally different from many amorphous HTMs including spiro-OMeTAD for PSC. As a result, this crystalline feature indicates a highly ordered structure of 4H4TIDIDF molecules, most probably due to strong intermolecular interaction.

With respect to the electrochemical property, cyclic voltammogram was measured using the solid film as shown in **Figure 5-3**. From this measurement, HOMO energy level was estimated to be -5.23 eV and -4.93 eV for 4H4TIDIDF and p,p-Spiro-OMeTAD, respectively. Their optical band gaps were found to be 2.30 eV and 2.94 eV from the edge of the absorption spectra and thus the LUMO energy levels were evaluated to be -2.93 eV and -1.99 eV, respectively. In comparison to p,p-Spiro-OMeTAD, the HOMO energy level of 4H4TIDIDF was lower, but was still higher than

the valence band (5.3 eV) of the perovskite, thereby providing sufficient driving force for the hole transfer at the interface of the perovskite and 4H4TIDIDF (**Figure 5-4**). Importantly, however, such lower HOMO level is expected to lead to a higher open-circuit voltage (V_{oc}) for 4H4TIDIDF.

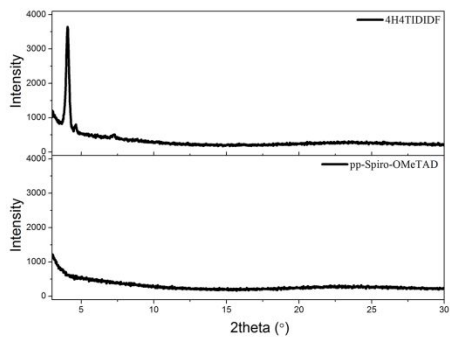


Figure 5-2. Out-of-plane XRD of 4H4TIDIDF and p,p-Spiro-OMeTAD.

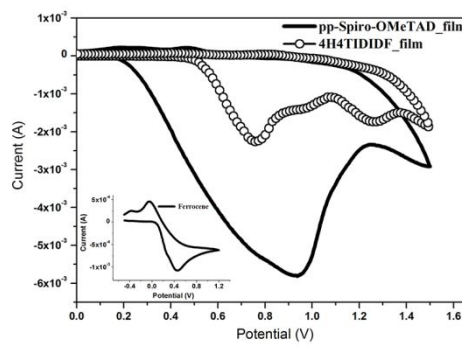


Figure 5-3. Cyclic voltammograms (CVs) of 4H4TIDIDF and p,p-Spiro-OMeTAD. Film samples were prepared on ITO patterned glass by drop-casting method (Inset: CV of ferrocene).

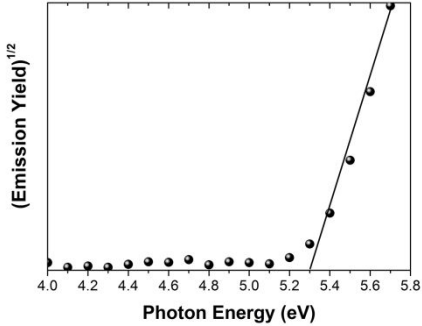


Figure 5-4. Photoelectron spectrum of the mixed perovskite film on a fused silica substrate.

5.3.2. Charge Transport Property

In order to get more insight into the charge transport property of 4H4TIDIDF in the sandwich-type device, space-charge-limited currents (SCLCs) measurement was carried out according to the literature method.^[25] As shown in **Figure 5-5a**, the hole mobility of each materials was determined by fitting the J - V curves to the reported equation (See section 5-2 Experimental section); The evaluated hole mobilities of p,p-Spiro-OMeTAD and 4H4TIDIDF are 2.17×10^{-4} and 1.69×10^{-3} , respectively. The value obtained in this work for p,p-Spiro-OMeTAD is similar to the data previously reported in the literature.^[26] Obviously, 4H4TIDIDF shows a higher mobility than that of p,p-Spiro-OMeTAD, which is attributed to a strong π - π interaction between a planar structures of the extended core as revealed in **Chapter 4**.

Photoluminescence (PL) quenching of the perovskite emission was examined to investigate the hole accepting capability of HTMs in bilayered film. The perovskite film employing the mixed perovskite of FAPbI₃ and MAPbBr₃ was prepared according to previous publication.^[4,6] Upon excitation at 670 nm, a broad PL band of perovskite/PMMA film is observed to be centered at 780 nm. Perovskite/4H4TIDIDF film shows a much larger decrease in PL intensity, as compared with perovskite/p,p-Spiro-OMeTAD film. This means that the charge transfer is more effective in the interface with 4H4TIDIDF, exhibiting a better hole collection capability at the

perovskite/4H4TIDIDF interface.

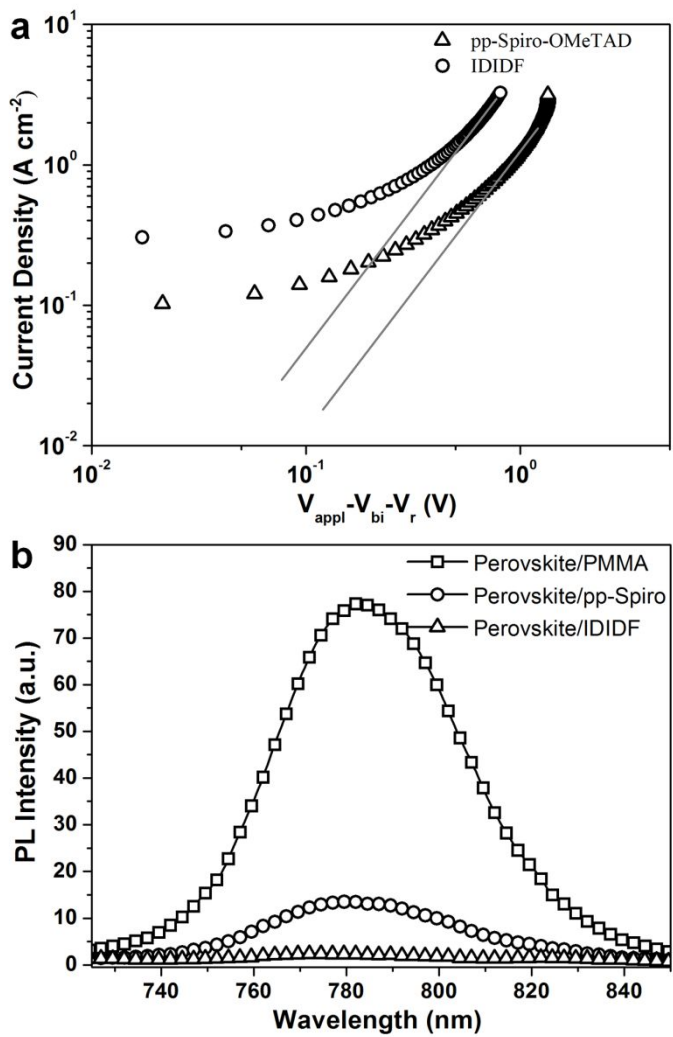


Figure 5-5. (a) The space-charge-limited-current (SCLC) of hole-only devices with the configuration of indium tin oxide (ITO)/poly(3,4-ethylenedioxythiophene)-polystyrene sulfonate (PEDOT:PSS)/p,p-Spiro-OMeTAD or 4H4TIDIDF/ Au. (b) PL emission spectra of perovskite/PMMA, perovskite/p,p-Spiro-OMeTAD, and perovskite/4H4TIDIDF film under excitation at 670 nm.

5.3.3. Perovskite Solar Cell Device Characteristics

To evaluate electrical characteristics of 4H4TIDIDF as a HTM for PSC, FAPbI₃-based PSC which is based on the typical bilayered device configuration consisting of fluorine doped tin oxide (FTO) substrate/blocking layer (bl)-TiO₂/mp-TiO₂/FAPbI₃-based perovskite/HTM/Au was fabricated. Through the reported solvent engineering technique,^[4-6] I and coworker prepared a dense and flat perovskite absorbing layer on the mp-TiO₂ scaffold, as shown in cross-sectional SEM image of the whole device (See **Figure 5-6a**). The subsequent deposition of 4H4TIDIDF forms a ~100 nm-thick HTM layer which is clearly distinguished from the perovskite layer and Au electrode. Details are described in Experimental section. **Figure 5-6b** describes a schematic energy level diagram of the whole device. As explained above, 4H4TIDIDF has appropriate HOMO and LUMO level for facilitating hole extraction and blocking electron leakage, considering the valence and conduction band of the perovskite in the device.

Figure 5-7a presents the average current density-voltage (*J-V*) curves for the best photovoltaic device fabricated using 4H4TIDIDF under reverse and forward scans, resulting in the average PCE of 19.05%, together with $J_{sc} = 23.55 \text{ mA/cm}^2$, $V_{oc} = 1.045 \text{ V}$, and FF= 77.2 %. This curve values obtained in the both scan directions with 10 mV voltage steps and a delay time of 50 ms, are averaged; the device shows a PCE of 19.8% for a reverse scan (from V_{oc} to J_{sc}), and a PCE of 18.3% for a forward scan (from J_{sc} to

V_{oc}) (See **Figure 5-7b**). To obtain the exact efficiency of the resultant device, the steady-state photocurrent was monitored at the maximum power point of 0.88 V and the corresponding steady-state efficiency was estimated to be 18.8%. (See **Figure 5-7c**) This is close to the average PCE in the device. External quantum efficiency (EQE) spectrum for the resultant device is shown in **Figure 5-7d**. The integrated J_{sc} calculated from EQE spectrum ($\sim 23 \text{ mA/cm}^2$) is almost similar to the measured J_{sc} . A high EQE of 80~88% in a broad range from 370 to 770 nm is found, which indicates an efficient light harvesting originating from a light absorber of the FAPbI₃-based perovskite, thereby contributing to a high J_{sc} . To unambiguously compare the performance with that of p,p-Spiro-OMeTAD, PSC devices were prepared using 4H4TIDIDF and p,p-Spiro-OMeTAD under the same condition. As shown in **Figure 5-7e**, the device fabricated using 4H4TIDIDF exhibits a higher PCE than that using p,p-Spiro-OMeTAD. Especially, as compared to other photovoltaic parameters, a relatively meaningful difference in V_{oc} is found, which is supported by the fact that the HOMO energy level of 4H4TIDIDF was lower than that of p,p-Spiro-OMeTAD. Furthermore, as compared to p,p-Spiro-OMeTAD, a higher hole mobility and a higher hole collection capability of 4H4TIDIDF must have facilitated hole extraction toward the Au with minimizing a carrier recombination, which is one of factors leading to a higher FF and PCE.

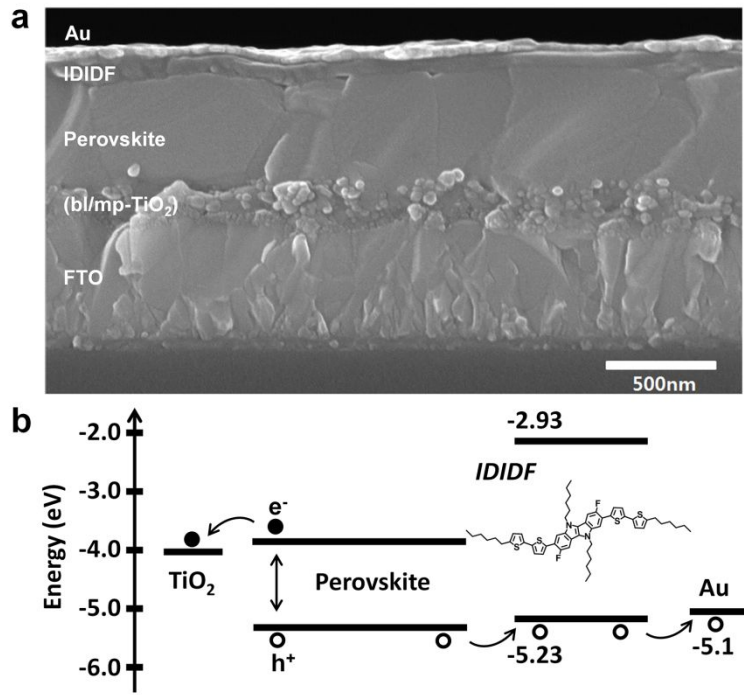


Figure 5-6. (a) Cross-sectional scanning electron microscopy (SEM) image of the device including FTO/ bl-TiO₂/mp-TiO₂/ perovskite/4H4TIDIDF/Au. (b) The schematic energy diagram of the corresponding device.

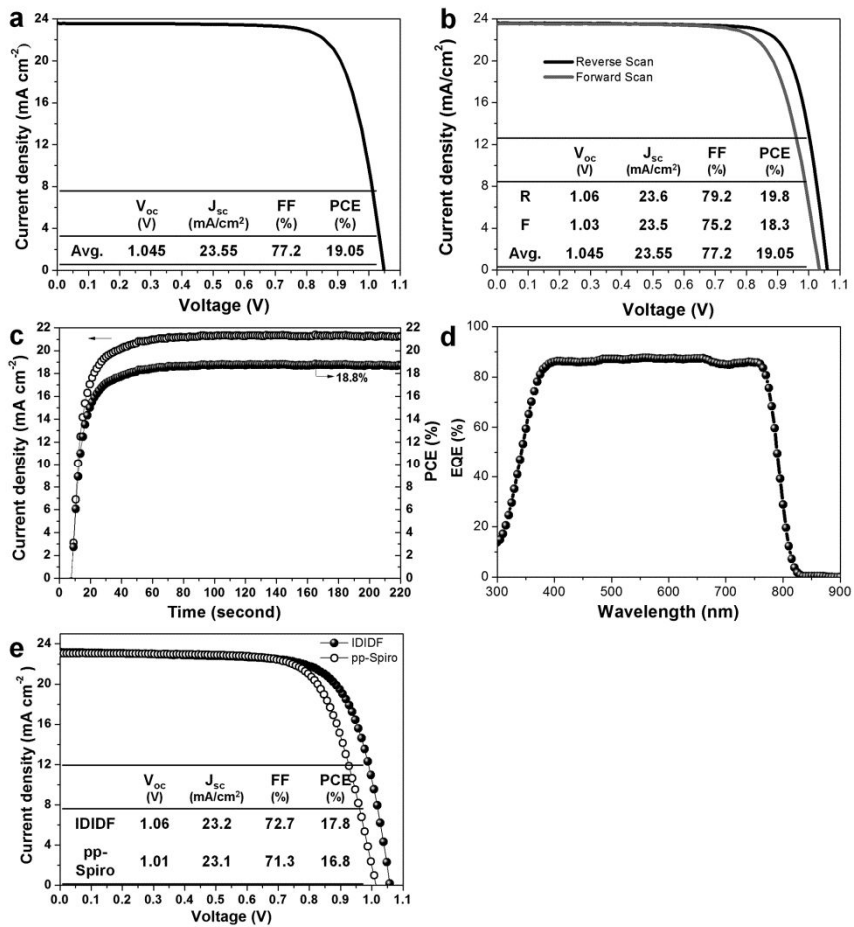


Figure 5-7. (a, b) Current density-voltage ($J-V$) curves of the best device (FTO/ bl-TiO₂/mp-TiO₂/ perovskite/IDIDF/Au, a) is average curve), (c) The steady-state photocurrent and efficiency of the corresponding device at the maximum power point (0.88 V). (d) The corresponding external quantum efficiency (EQE) spectra. (e) The comparison of $J-V$ curves of the devices fabricated using IDIDF and commercial pp-Spiro. Li-bis(trifluoromethanesulfonyl)imide (Li-TFSI) and 4-*tert*-butylpyridine (*t*BP) as additives are used in this work.

5.4. Conclusion

I synthesized fluorinated IDID derivative as a high-performance crystalline HTM for perovskite solar cells. A planar π -conjugated backbone linked with a flexible alkyl chain enabled a formation of molecular stacked arrangement by strong π - π interaction, which was revealed in single crystal analysis. In this regard, 4H4TIDIDF in film state showed a higher mobility than that of p,p-Spiro-OMeTAD. PL quenching occurred more effectively at the perovskite/4H4TIDIDF interface, when compared to that at the perovskite/p,p-Spiro-OMeTAD. From CV measurement, a proper HOMO and LUMO energy level for 4H4TIDIDF was found to be suitable for a HTM. As a result, the device fabricated using 4H4TIDIDF showed a better performance as compared to p,p-Spiro-OMeTAD, exhibiting a best PCE of 19%. It was thus shown that a planar IDID core-based crystalline HTM is a promising candidate for highly efficient perovskite solar cells.

5.5. Reference

- [1] A. Kojima, K. Teshima, Y. Shirai, T. Miyasaka, *J. Am. Chem. Soc.* **2009**, *131*, 6050.
- [2] P. Gao, M. Grätzel, M. K. Nazeeruddin, *Energy Environ. Sci.* **2014**, *7*, 2448.
- [3] M. A. Green, A. Ho-Baillie, H. J. Snaith, *Nat. Photonics* **2014**, *8*, 506.
- [4] N. J. Jeon, J. H. Noh, W. S. Yang, Y. C. Kim, S. Ryu, J. Seo, Seok, S. I. *Nature* **2015**, *517*, 476.
- [5] W. S. Yang, J. H. Noh, N. J. Jeon, Y. C. Kim, S. Ryu, J. Seo, S. I. Seok, *Science* **2015**, *348*, 1234
- [6] Y. C. Kim, J. H. Noh, N. J. Jeon, W. S. Yang, J. Seo, J. S. Yun, A. Ho-Baillie, S. Huang, M. A. Green, J. Seidel, T. K. Ahn, S. I. Seok, *Adv. Energy Mater.*, DOI:10.1002/aenm.201502104.
- [7] F. Matteocci, S. Razza, F. D. Giacomo, S. Casaluci, G. Mincuzzi, T. M. Brown, A. D'Epifanio, S. Licoccia, A. D. Carlo, *Phys. Chem. Chem. Phys.* **2014**, *16*, 3918.
- [8] Y. Rong, L. Liu, A. Mei, X. Li, H. Han, *Adv. Energy Mater.* **2015**, *5*, 1501066.

- [9] H. Li, K. Fu, A. Hagfeldt, M. Grätzel, S. G. Mhaisalkar, A. C. Grimsdale, *Angew. Chem. Int. Ed.* **2014**, *53*, 4085.
- [10] T. Krishnamoorthy, F. Kunwu, P. P. Boix, H. Li, T. M. Koh, W. L. Leong, S. Powar, A. Grimsdale, M. Grätzel, N. Mathews, S. G. Mhaisalkar, *J. Mater. Chem. A* **2014**, *2*, 6305.
- [11] P. Qin, S. Paek, M. I. Dar, N. Pellet, J. Ko, M. Grätzel, M. K. Nazeeruddin, *J. Am. Chem. Soc.* **2014**, *136*, 8516.
- [12] N. J. Jeon, J. Lee, J. H. Noh, M. K. Nazeeruddin, M. Grätzel, S. I. Seok, *J. Am. Chem. Soc.* **2013**, *135*, 19087.
- [13] A. Krishna, D. Sabba, H. R. Li, J. Yin, P. P. Boix, C. Soci, S. G. Mhaisalkar, A. C. Grimsdale, *Chem. Sci.* **2014**, *5*, 2702.
- [14] N. J. Jeon, H. G. Lee, Y. C. Kim, J. Seo, J. H. Noh, J. Lee, S. I. Seok, *J. Am. Chem. Soc.* **2014**, *136*, 7837.
- [15] J. Seo, N. J. Jeon, W. S. Yang, H.-W. Shin, T. K. Ahn, J. Lee, J. H. Noh, S. I. Seok, *Adv. Energy Mater.* **2015**, *5*, 1501320.
- [16] M. Saliba, S. Orlandi, T. Matsui, S. Aghazada, M. Cavazzini, J.-P. Correa-Baena, P. Gao, R. Scopelliti, E. Mosconi, K.-H. Dahmen, F. D. Andgelis, A. Abate, A. Hagfeldt, G. Pozzi, M. Grätzel, M. K. Nazeeruddin, *Nat. Energy*, DOI:10.1038/NENERGY.2015.17.

- [17] H. Wang, A. D. Sheikh, Q. Feng, F. Li, Y. Chen, W. Yu, E. Alarousu, C. Ma, M. A. Haque, D. Shi, Z.-S. Wang, O. F. Mohammed, O. M. Bakr, T. Wu, *ACS Photonics* **2015**, *2*, 849.
- [18] B. Xu, E. Sheibani, P. Liu, J. Zhang, H. Tian, N. Vlachopoulos, G. Boschloo, L. Kloo, A. Hagfeldt, L. Sun, *Adv. Mater.* **2014**, *26*, 6629.
- [19] I. Lim, E.-K. Kim, S. A. Patil, D. Y. Ahn, W. Lee, N. K. Shrestha, J. K. Lee, W. K. Seok, C.-G. Cho, S.-W. Han, *RSC Adv.* **2015**, *5*, 55321.
- [20] K. Rakstys, A. Abate, M. I. Dar, P. Gao, V. Jankauskas, G. Jacopin, E. Kamarauskas, S. Kazim, S. Ahmad, M. Grätzel, M. K. Nazeeruddin, *J. Am. Chem. Soc.* **2015**, *137*, 16172.
- [21] Y. Jin, K. Kim, S. Song, J. Kim, J. Kim, S. H. Park, K. Lee, H. Shu, *Bull. Korean Chem. Soc.* **2006**, *27*, 1043.
- [22] L. Qiu, C. Yu, N. Zhao, W. Chen, Y. Guo, X. Wan, R. Yang, Y. Liu, *Chem. Commun.* **2012**, *48*, 12225.
- [23] Y.-Y. Lai, J.-M. Yeh, C.-E. Tsai, Y.-J. Cheng, *Eur. J. Org. Chem.* **2013**, *23*, 5076.
- [24] Z. R. Owczarczyk, W. A. Braunecker, A. Garcia, R. Larsen, A. M. Nardes, N. Kopidakis, D. S. Ginley, D. C. Olson, *Macromolecules* **2013**, *46*, 1350.
- [25] O. K. Kwon, M. A. Uddin, J. H. Park, S. K. Park, T. L. Nguyen, H. Y. Woo, S. Y. Park, *Adv. Mater.* DOI:10.1002/adma.201504091.

- [26] S. S. Reddy, K. Gunasekar, J. H. Heo, S. H. Im, C. S. Kim, D.-H. Kim, J. H. Moon, J. Y. Lee, M. Song, S.-H. Jin, *Adv. Mater.* **2016**, *28*, 686.

Chapter 6.

Fluorinated Indolo[3,2-b]indole-Based Low Band-gap Small Molecules for High-Performance Organic Solar Cells

6.1. Introduction

Over the past decade, solution-processed bulk heterojunction organic solar cells (BHJ-OSCs) comprising p-type (donor) and n-type (acceptor) semiconductors, have tremendous interest as a promising technology for the next generation of renewable energy-conversion, owing to their capability of realizing low-cost, large area, flexible, and light-weight electronic devices.^[1-3] Intensive research on developing noble photoactive organic semiconductor materials and fabrication technique optimization have led steep and significant advances, and nowadays, ca. > 10% of power conversion efficiency (PCE) was achieved.^[4-5] Even though, polymeric donors have been presciently progressed as a majority of research until now,^[6-10] their inherent disadvantages such as batch-to-batch variations, unclear molecular structure, and fastidious purification considered as drawbacks to the further improvement of device performance, and precluded precise structure-property correlation. Therefore, small molecules which offer advantages such as well-defined molecular structure, easy purification, high reproducibility, and device consistency, have attracted tremendous

attentions in view of fine-tuning of molecular structure, electronic characteristic, and intermolecular interaction, and also, gave a chance to elucidate precise structure-property relationship.^[11-15] Consequently, PCE of small molecular donor system also reached up to ca. 10%, recently.^[16-17]

In order to improve PCE of the BHJ-OSC, in principle, the donor material has to have wide range of absorption with high extinction coefficient, low-lying highest occupied molecular orbital (HOMO) energy level, and high charge carrier mobility.^[18,19] In other words, band-gap of the donor material should be less than 1.6 eV, because the solar photon in the solar spectrum is mainly distributed around 600-800 nm, and HOMO level should be located around 5.3~5.6 eV because the lowest unoccupied molecular orbital (LUMO) energy level of the [6,6]-phenyl-C₆₁-butyric acid methyl ester (PC₆₁BM) which is commonly used acceptor is located around 4.0~4.3 eV and exciton dissociation energy (ca. 0.3 eV) should be considered. Furthermore, efficient intermolecular interaction motif of which electronic structure is favorable for free charge carrier hopping. To satisfy aforementioned parameters simultaneously, wide range of π -conjugated materials were extensively investigated.^[11,12]

One of the most promising strategies for designing high performance low bandgap small molecule is to use intramolecular charge transfer (ICT) interaction which is occurred between covalently linked electron-donor (D) and electron-acceptor (A) units. Therefore, various analogs, for instance, D-A, D-A-D, and A-D-A, were employed and reported with diverse combination of D and A building blocks. However, D and A

building blocks who ensure the high performance is still rather limited for few molecular structures, such as benzodithiophene, dithienosilole, diketopyrrolypyrrole, and fluorinate benzothiadiazole.^[20-30] Therefore, development of novel π -conjugated structure is strongly demanded to enrich the pool of promising building block for the realizing high performance SMOCS. As for the D building block for the push-pull structure, pyrrole-fused heteroacenes have attracted intensive interests owing to their electron donating nature and structural diversity.^[31] As one of the most famous D building block, indeed, carbazole unit have been lead the field of polymer OSC in early years,^[32-34] therefore other pyrrole-fused heteroacenes, such as dithienopyrrole and indolocarbazole, were extensively investigated.^[35-41] Among various kinds of pyrrole-fused heteroacenes, recently, indolo[3,2-b]indole (IDID) core which is comprised two pyrrole rings and two benzene rings fused linearly with centrosymmetric geometry, also investigated as a donor building block for the push-pull structure of small molecule and polymer analog.^[39-41] Attributed to symmetrically-fused two pyrrole rings, IDID exhibited strong electron donating nature, and also, solubility of incorporated structure could be feasibly controlled. Therefore, reported IDID derivatives, of which electron acceptor building block was diketopyrrolypyrrole, exhibited optical bandgap of ca. 1.6 eV, and their aliphatic side chains were quite variable. However, resulting electrical characteristics of OSC devices revealed rather low open circuit voltage (V_{oc}); most probably due to energy level mismatch with PC₆₁BM, owing to relatively low ionization potential of IDID core. To solve this inherent drawback of IDID core, and to

make the most of advantages of IDID molecular platform simultaneously, in this work, I tried to use halogenated IDID core as a D building block of low bandgap small molecule for the p-type semiconductor of SMOSC. Even though, in point of energy level stabilization, chlorine (Cl) atom substitution should work more effectively than fluorine (F) atom substitution attributed to their vacant d orbital, formation of free charge carrier transport pathway through the efficient intermolecular packing could be interrupted by much bigger van der Walls radius of Cl atom than that of F atom.^[42] Furthermore, fluorination on π -conjugated system is verified strategy for the energy level stabilization and inter-/intramolecular secondary interaction occurrence in several molecular systems for OSC.^[43] To this end, fluorinated IDID-based low bandgap small molecules were designed and synthesized for applications in OSC. Furthermore, to elucidate fluorination effect on IDID-based low bandgap small molecules, their photophysical, electrochemical, thermal, and electrical properties were directly compared with non-fluorinated counter molecules.

6.2. Experimental

Synthesis

Unless stated otherwise, all reagents were purchased at Sigma Aldrich, TCI, and Alfa Aesar. The synthesis of 2,7-dibromo-5,10-dihydroindolo[3,2-b]indole and 2,7-dibromo-3,8-difluoro-5,10-dihydroindolo[3,2-b]indole was described in **chapter 2** and

chapter 4, respectively.

Synthesis of 2,7-dibromo-5,10-bis(2-hexyldecyle)-5,10-dihydroindolo[3,2-b]indole (**2**).

A round-bottom flask, equipped with a magnetic stirrer bar and reflux condenser was baked under reduced pressure and backfilled with Ar. After then, 2,7-dibromo-5,10-dihydroindolo[3,2-b]indole (620 mg, 1.708 mmol), anhydrous tetrahydrofuran (30 mL), and NaH (204 mg, 8.516 mmol) were added to the baked reaction vessel. After 10 minutes at room temperature, 3 g (8.516 mmol) of 1-iodo-2-hexyldecane was added to the reaction mixture. After stirring 10 minutes, the reaction mixture was gently refluxed for 48 hours. After reaction finished, the reaction mixture was poured into brine (300 mL), and extracted with dichloromethane. The combined organic phase was dried with MgSO₄ and concentrated under reduced pressure. The crude product was purified by flash column chromatography (ethyl acetate/n-hexane 1:50, v/v) to afford compound **2** as white glassy solid (980 mg, 70 %). ¹H-NMR (300 MHz, Acetone-d6, δ): 7.86 (d, *J* = 8.49 Hz, 2H), 7.79 (d, *J* = 1.56 Hz, 2H), 7.28 (dd, *J* = 8.46 Hz, 1.68 Hz, 2H), 4.48 (d, *J* = 7.68 Hz, 4H), 2.26-2.21 (m, 2H), 1.38-1.17 (m, 48H), 0.88-0.79 (m, 12H).

Synthesis of 5,10-bis(2-hexyldecyle)-2,7-bis(4,4,5,5-tetramethyl-1,3,2-dioxaborolan-2-yl)-5,10-dihydroindolo[3,2-b]indole (**3**).

Compound **2** (712 mg, 0.866 mmol) and anhydrous tetrahydrofuran (25 mL) were added into a 100 mL round-bottom flask and evacuated and backfilled with Ar. After then, reaction vessel was cooled down to -78°C. An hour later, n-BuLi (4.331 mmol)

was added dropwise at -78°C. After an hour, 2-isopropoxy-4,4,5,5-tetramethyl-1,3,2-dioxaborolane (4.331 mmol) was added and warmed to room temperature. After reaction finished, reaction mixture was quenched with brine (300 mL), and extracted with dichloromethane. The combined organic phase was concentrated under reduced pressure, and purified by column chromatography (ethyl acetate/n-hexane 1:100, v/v) to afford compound **3** as dim yellow solid (0.380 g, 48.3%). ¹H-NMR (300 MHz, Acetone-d6, δ): 7.97 (s, 2H), 7.95 (d, *J* = 8.07 Hz, 2H), 7.56 (d, *J* = 8.04 Hz, 2H), 4.53 (d, *J* = 7.56 Hz, 4H), 2.26-2.25 (m, 2H), 1.38-1.16 (m, 72H), 0.87-0.78 (m, 12H).

Synthesis of 5',5'''-(5,10-bis(2-hexyldecyl)-5,10-dihydroindolo[3,2-b]indole-2,7-diyl)bis([2,2'-bithiophene]-5-carbaldehyde)) (**4**).

Compound **3** (350 mg, 0.386 mmol), 5'-bromo-[2,2'-bithiophene]-5-carbaldehyde (232 mg, 0.849 mmol), tetrakis(triphenylphosphine)palladium(0) (67 mg, 0.058 mmol), 2N K₂CO₃ aqueous solution (10 mL), and tetrahydrofuran (20 mL) were added into a 100 mL round-bottom flask and evacuated and backfilled with Ar. After then, reaction vessel was gently refluxed for 12 hours. After reaction finished, reaction mixture was quenched with 1N HCl aqueous solution (300 mL), and extracted with dichloromethane. The combined organic phase was dried with MgSO₄ and concentrated under reduced pressure. The crude product was purified by flash column chromatography (chloroform/ethyl acetate/n-hexane; 1:0.5:3, v/v) and subsequently by recrystallization (ethyl acetate) to afforded compound **4** as red solid (260 mg, 64.8%). ¹H-NMR (300 MHz, Tetrahydrofuran-d8, δ): 9.84 (s, 2H), 7.90 (d, *J* = 8 Hz, 2H), 7.81

(m, 4H), 7.50 ~ 7.38 (m, 8H), 4.51 (d, J = 11.65 Hz, 4H), 2.29 (m, 2H), 1.44 ~ 1.21 (m, 48H), 0.83 ~ 0.81 (m, 12H).

Synthesis of 2,7-dibromo-5,10-bis(2-hexyldecyle)-5,10-dihydroindolo[3,2-b]indole (**6**).

Compound **6** was synthesized by the same synthetic procedure as that for compound **2** by using compound **5** (600 mg, 1.499 mmol), 1-iodo-2-hexyldecane (2.64 g, 7.499 mmol) anhydrous THF (20 mL), and NaH (180 mg, 7.499 mmol). The crude product was purified by column chromatography (ethyl acetate/n-hexane; 1:99, v/v) to afford compound **6** as glassy solid (1.15 g, 90%). $^1\text{H-NMR}$ (300 MHz, Acetone-d₆, δ): 7.89 (d, J = 5.76 Hz, 2H), 7.79 (d, J = 9.48 Hz, 2H), 4.49 (d, J = 7.71 Hz, 4H), 2.18 (m, 2H), 1.35-1.16 (m, 48H), 0.87-0.78 (m, 12H).

Synthesis of 2,7-dibromo-3,8-difluoro-5,10-bis(2-octyldodecyle)-5,10-dihydroindolo[3,2-b]indole (**6'**).

Compound **6'** was synthesized by the same synthetic procedure as that for compound **6** using compound **5** (900 mg, 2.250 mmol), 1-iodo-2-octyldodecane (4.6g, 11.249 mmol) anhydrous THF (40 mL), and NaH (270 mg, 11.249 mmol). The crude product was purified by column chromatography (ethyl acetate/n-hexane; 1:99, v/v) to afford compound **6'** as glassy solid (1.68 g, 77.7%). $^1\text{H-NMR}$ (300 MHz, Tetrahydrofuran-d₈, δ): 7.78 (d, J = 5.67, 2H), 7.68 (d, J = 9.24, 2H), 4.39 (d, J = 7.56, 4H), 2.14 (m, 2H), 1.50 ~ 0.84 (m, 64H), 0.67 ~ 0.66 (m, 12H).

Synthesis of 3,8-difluoro-5,10-bis(2-hexyldecyl)-2,7-bis(4,4,5,5-tetramethyl-1,3,2-dioxaborolan-2-yl)-5,10-dihydroindolo[3,2-b]indole (**7**).

Compound **7** was synthesized by the same synthetic procedure as that for compound **3** by using compound **6** (750 mg, 0.884 mmol), n-BuLi (2.650 mmol), 2-isopropoxy-4,4,5,5-tetramethyl-1,3,2-dioxaborolane (2.650 mmol), and tetrahydrofuran (25 mL). The crude product was purified by column chromatography (ethyl acetate/n-hexane; 1:50, v/v) to afford compound **7** as dim green solid (450 mg, 61.2%). ¹H-NMR (300 MHz, Acetone-d₆, δ): 7.88 (d, *J* = 4.53 Hz, 2H), 7.60 (d, *J* = 10.02 Hz, 2H), 4.50 (d, *J* = 7.56 Hz, 4H), 2.18 (m, 2H), 1.38-1.15 (m, 72H), 0.86-0.79 (m, 12H).

Synthesis of 3,8-difluoro-5,10-bis(2-octyldodecyle)-2,7-bis(4,4,5,5-tetramethyl-1,3,2-dioxaborolan-2-yl)-5,10-dihydroindolo[3,2-b]indole (**7'**).

Compound **7'** was synthesized by the same synthetic procedure as that for compound **7** by using compound **6'** (1.3 g, 1.353 mmol), n-BuLi (4.058 mmol), 2-isopropoxy-4,4,5,5-tetramethyl-1,3,2-dioxaborolane (4.058 mmol), and tetrahydrofuran (30 mL). The crude product was purified by column chromatography (ethyl acetate/n-hexane; 1:50, v/v) to afford compound **7** as dim green solid (950 mg, 67.6%). ¹H-NMR (300 MHz, Acetone-d₆, δ): 7.83 (d, *J* = 3.93 Hz, 2H), 7.49 (d, *J* = 9.75 Hz, 2H), 4.42 (d, *J* = 7.17 Hz, 4H), 2.16 (m, 2H), 1.35-1.18 (m, 88H), 0.87-0.83 (m, 12H).

Synthesis of 5',5'''-(3,8-difluoro-5,10-bis(2-hexyldecyl)-5,10-dihydroindolo[3,2-b]indole-2,7-diyl)bis([2,2'-bithiophene]-5-carbaldehyde) (**8**).

Compound **8** was synthesized by the same synthetic procedure as that for compound **4** by using compound **7** (300 mg, 0.318 mmol), 5'-bromo-[2,2'-bithiophene]-5-carbaldehyde (192 mg, 0.699 mmol),

tetrakis(triphenylphosphine)palladium(0) (55 mg, 0.048 mmol), 2N K₂CO₃ aqueous solution (10 mL), and tetrahydrofuran (20 mL). The crude product was purified by column chromatography (chloroform/ethyl acetate/n-hexane; 3:0.3:6.7, v/v) to afford compound **8** as red solid (250 mg, 78.9%). ¹H-NMR (300 MHz, Tetrahydrofuran-d8, δ): 9.84 (s, 2H), 7.84 (d, *J* = 6.33 Hz, 2H), 7.80 (d, *J* = 3.99 Hz, 2H), 7.71 (d, *J* = 12.27 Hz, 2H), 7.57 (d, *J* = 3.81 Hz, 2H), 7.51 (d, *J* = 3.93 Hz, 2H), 7.43 (d, *J* = 3.93 Hz, 2H), 4.49 (d, *J* = 7.65 Hz, 4H), 2.21 (m, 2H), 1.41-1.19 (m, 48H), 0.84-0.80 (m, 12H).

Synthesis of 5',5'''-(3,8-difluoro-5,10-bis(2-octyldodecyle)-5,10-dihydroindolo[3,2-b]indole-2,7-diyl)bis([2,2'-bithiophene]-5-carbaldehyde) (**8'**).

Compound **8'** was synthesized by the same synthetic procedure as that for compound **8** by using compound **7'** (600 mg, 0.588 mmol), 5'-bromo-[2,2'-bithiophene]-5-carbaldehyde (354 mg, 1.295 mmol), tetrakis(triphenylphosphine)palladium(0) (102 mg, 0.088 mmol), 2N K₂CO₃ aqueous solution (10 mL), and tetrahydrofuran (20 mL). The crude product was purified by column chromatography (chloroform/ethyl acetate/n-hexane; 5:0.3:4.7, v/v) and subsequently by recrystallization (ethyl acetate) to afford compound **8** as red solid (250 mg, 78.9%). ¹H-NMR (300 MHz, Tetrahydrofuran-d8, δ): 9.84 (s, 2H), 7.84 (d, *J* = 5.64 Hz, 2H), 7.80 (d, *J* = 3.96 Hz, 2H), 7.71 (d, *J* = 12.09 Hz, 2H), 7.56 (d, *J* = 3.3 Hz, 2H), 7.51 (d, *J* = 3.99 Hz, 2H), 7.42 (d, *J* = 4.11 Hz, 2H), 4.49 (d, *J* = 7.65 Hz, 4H), 2.22 (m, 2H), 1.60-1.19 (m, 64H), 0.99-0.78 (m, 12H).

Synthesis of **HD4TIDID-OCA**.

A mixed solution of compound **4** (120 mg, 0.115 mmol), octyl cyanoacetate (343mg, 1.154 mmol), trimethylamine (catalytic amount), and chloroform (20 mL) was vigorously stirred for 48 hours under Ar atmosphere. After reaction finished, reaction mixture was poured into methanol (100 mL) and filtered. The crude product (filtered out) was purified by flash column chromatography (chloroform/ethyl acetate/n-hexane; 2:0.15:7.85) to afford **HD4TIDID-OCA** as dark purple solid (100 mg, 61.9%). ¹H-NMR (500MHz, Tetrahydrofuran-d8, δ): 8.360 (s, 2H), 7.868 (d, J =8.5 Hz, 2H), 7.825 ~ 7.810 (m, 4H), 7.545 (d, J =4 Hz, 2H), 7.530 ~ 7.481 (m, 4H), 7.411 (d, J =4 Hz, 2H), 4.472 (d, J =7.5 Hz, 4H), 4.257 (t, J =7 Hz, 4H), 2.272 (m, 2H), 1.438 ~ 1.197 (m, 72H), 0.907 (t, J =7 Hz, 6H), 0.893 ~ 0.849 (m, 12H), ¹³C-NMR (500MHz, Tetrahydrofuran-d8, δ): 163.53, 149.51, 148.33, 146.68, 142.91, 141.07, 135.34, 134.90, 128.83, 128.66, 128.43, 124.89, 124.73, 119.45, 117.58, 116.54, 115.32, 108.25, 98.72, 50.33, 39.98, 33.03, 32.94, 32.75, 32.71, 31.13, 30.81, 30.67, 30.45, 30.35, 29.70, 27.62, 26.96, 23.72, 23.68, 14.16, HRMS(FAB, m/z): Calcd for C₈₆H₁₁₆N₄O₄S₄: 1396.7879, found: 1396.7889, Elel. Anal. Calcd. For C₈₆H₁₁₆N₄O₄S₄: C 73.88, H 8.36, N 4.01, O 4.58, S 9.17; found: C 74.09, H 8.39, N 4.03, S 9.46.

Synthesis of **HD4TIDID-Rho**.

A mixed solution of compound **4** (120 mg, 0.115 mmol), 3-ethyl rhodanine (186 mg, 1.154 mmol), piperidine (catalytic amount), and chloroform (30 mL) was vigorously stirred for 48 hours at 50°C under Ar atmosphere. After reaction finished, reaction mixture was poured into methanol (100 mL) and filtered. The crude product (filtered

out) was purified by flash column chromatography and subsequently by recrystallization (tetrahydrofuran) to afford **HD4TIDID-Rho** as dark brown solid (90 mg, 58.8%). ¹H-NMR (500MHz, Tetrahydrofuran-d8, δ): 7.938 (s, 2H), 7.897 (d, J =8 Hz, 2H), 7.828 (s, 2H), 7.545 ~ 7.485 (m, 8H), 7.415 (d, J =3 Hz, 2H), 4.516 (d, J =7 Hz, 4H), 4.168 (m, 4H), 2.297 (m, 2H), 1.446 ~ 1.222 (m, 54H), 0.838 ~ 0.822 (m, 12H),
Elem. Anal. Calcd. For C₇₄H₉₂N₄O₂S₈: C 67.03, H 6.99, N 4.23, O 2.41, S 19.34; found:
C 67.00, H 6.97, N 4.21, S 19.38. (¹³C NMR and HRMS data could not be obtained due to insufficient solubility of **HD4TIDID-Rho** for common solvents)

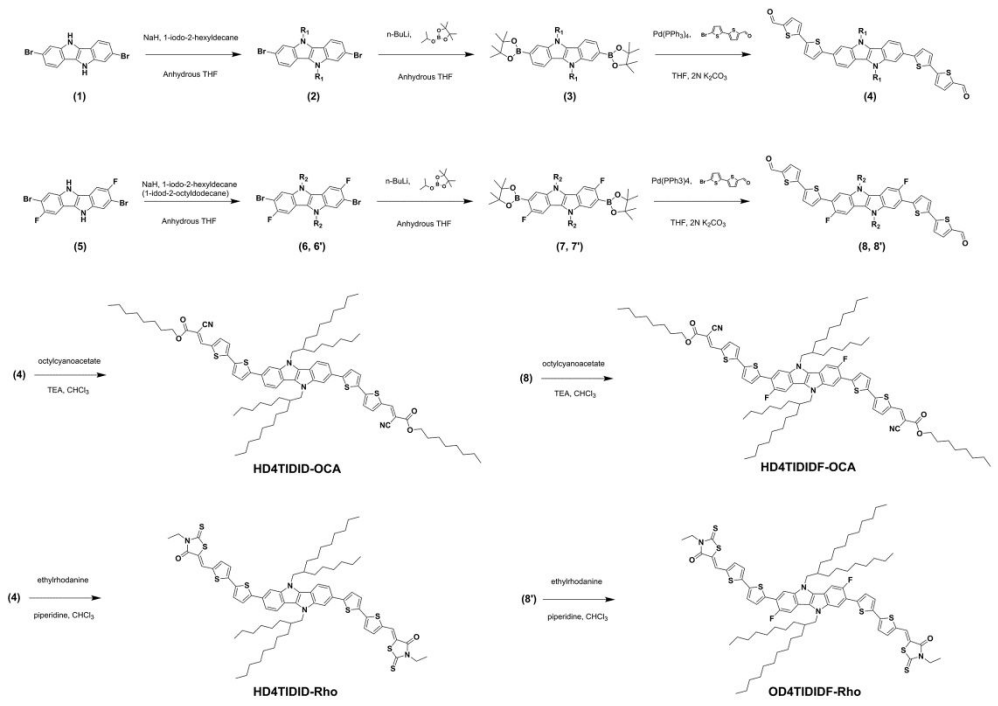
Synthesis of **HD4TIDIDF-OCA**.

A mixed solution of compound **4** (130 mg, 0.121 mmol), octyl cyanoacetate (359 mg, 1.208 mmol), trimethylamine (catalytic amount), and chloroform (20 mL) was vigorously stirred for 48 hours under Ar atmosphere. After reaction finished, reaction mixture was poured into methanol (100 mL) and filtered. The crude product (filtered out) was purified by flash column chromatography (chloroform/ethyl acetate/n-hexane; 3:0.3:6.7) and subsequently by recrystallization (ethyl acetate) to afford **HD4TIDIDF-OCA** as dark purple solid (93 mg, 53.7%). ¹H-NMR (500MHz, Tetrahydrofuran-d8, δ): 8.367 (s, 2H), 7.838 ~ 7.822 (m, 4H), 7.691 (d, J =12 Hz, 2H), 7.601 (d, J =3 Hz, 2H), 7.574 (d, J =3.5 Hz, 2H), 7.452 (d, J =4 Hz, 2H), 4.473 (d, J =7.5 Hz, 4H), 4.259 (t, J =7 Hz, 4H), 2.215 (m, 2H), 1.445 ~ 1.192 (m, 72H), 0.906 (t, J =7 Hz, 6H), 0.845 ~ 0.831 (m, 12H), ¹³C-NMR (500MHz, Tetrahydrofuran-d8, δ): 163.48, 155.66, 153.76, 147.87, 146.69, 142.17, 142.14, 141.01, 139.70, 136.20, 136.16, 135.67, 129.68, 128.24,

127.90, 127.84, 125.25, 117.51, 117.38, 116.50, 114.33, 114.25, 109.84, 105.36, 105.15, 99.01, 50.33, 40.00, 33.01, 32.95, 32.92, 32.69, 32.65, 31.10, 30.78, 30.64, 30.44, 30.35, 29.70, 27.60, 26.94, 23.72, 23.70, 23.67, 14.61, HRMS(FAB, m/z): Calcd for $C_{86}H_{114}F_2N_4O_4S_4$: 1432.7691, found: 1432.7671, Elel. Anal. Calcd. For $C_{86}H_{114}F_2N_4O_4S_4$: C 72.03, H 8.01, F 2.65, N 3.91, O 4.46, S 8.94; found: C 72.08, H 8.07, N 3.90, S 8.99.

Synthesis of **OD4TIDIDF-Rho**.

A mixed solution of compound **8'** (330 mg, 0.228 mmol), 3-ethyl rhodanine (448 mg, 2.778 mmol), piperidine (catalytic amount), and chloroform (40 mL) was vigorously stirred for 48 hours at 50°C under Ar atmosphere. After reaction finished, reaction mixture was poured into methanol (100 mL) and filtered. The crude product (filtered out) was purified by flash column chromatography (chloroform/ethyl acetate/n-hexane; 4:0.2:5.8) and subsequently by recrystallization (chloroform and tetrahydrofuran) to afford **HD4TIDID-Rho** as dark brown solid (310 mg, 75.7%). 1H -NMR (500MHz, Tetrahydrofuran-d8, δ): 7.945 (s, 2H), 7.853 (s, 2H), 7.721 (d, $J=11.5$ Hz, 2H), 7.600 ~ 7.526 (m, 6H), 7.454 (m, 2H), 4.509 (d, $J=6$ Hz, 4H), 4.170 (m, 4H), 2.233 (m, 2H), 1.425 ~ 1.209 (m, 70 H), 0.853 ~ 0.840 (m, 12H), Elel. Anal. Calcd. For $C_{82}H_{106}F_2N_4O_2S_8$: C 66.81, H 7.25, F 2.58, N 3.80, O 2.17, S 17.40; found: C 66.84, H 7.29, N 3.78, S 17.50. (^{13}C NMR and HRMS data could not be obtained due to insufficient solubility of OD4TIDIDF-Rho for common solvents)



Scheme 6-1. Synthetic route for IDID derivatives and their chemical structures.

6.3. Results and Discussion

6.3.1. Design and Synthesis

As described in **chapter 3**, it has confirmed that IDID is efficient electron donor building block for the molecules utilizing ICT interaction. To elaborate structure-property relationship, and also to explore the effect of the fluorinated IDID core on electronic characteristics of ICT-type IDID derivatives as an electron donor building block, two non-fluorinated IDID derivatives, HD4TIDID-OCA and HD4TIDID-Rho, and two fluorinated IDID derivatives, HD4TIDIDF-OCA and OD4TIDIDF-Rho, were designed and synthesized (see **Scheme 6-1**). To realize low enough bandgap for the wide range of absorption with high extinction coefficient, acceptor- π -donor- π -acceptor molecular architecture was employed with octylcyanoacetate (OCA) and 3-ethylrhodanine (Rho) as an electron acceptor, and bithophene as a π -spacer. For enabling the solution processing, 2-hexyldecane was substituted at *N*-position of IDID core; in case of OD4TIDIDF-Rho, 2-octyldodecane was substituted at *N*-positon of fluorinated IDID core because of not enough solubility of 2-hexyldecane substituted derivative for the solution processing. Synthesis of 2,7-dibromo-5,10-dihexyl-5,10-dihydroinolo[3,2-b]indole (**Scheme 6-1**, 1) and 2,7-dibromo-3,8-difluoro-5,10-dihexyl-5,10-dihydroinolo[3,2-b]indole (**Scheme 6-1**, 5) were according to **Scheme 2-1** and

Scheme 4-1, respectively; from which four different IDID derivatives were successfully synthesized through, S_N2 *N*-alkylation, lithium-exchange borylation, Suzuki-Miyaura cross-coupling, and Knoevenagel reaction. All the final products were carefully characterized by 1H NMR, ^{13}C NMR, elemental analysis, and mass analysis. Detailed synthetic procedures are described in **Scheme 3-1** and section 6-2 Experimental Section.

6.3.2. Optical, Electrochemical, and Thermal Properties

The photophysical characteristics of newly synthesized IDID derivatives were evaluated by the UV-vis absorption measurements at a concentration of 1×10^{-5} M in tetrahydrofuran (THF) solutions and also for spin-coated films (see **Figure 6-1**, detailed data listed in **Table 6-1**). In solution states, all of the IDID derivatives exhibited broad absorption range (absorption band-edge of ca. $600 \sim 650$ nm) with considerably high molar absorptivity ($> 65000\text{ M}^{-1}\text{ cm}^{-1}$) at the spin allowed energy transition maxima corresponding to ICT transition. When changed from solution state to solid states, absorption spectra of IDID derivatives exhibited bathochromic shifts, 20 ~ 30 nm for OCA derivatives (HD4TIDID-OCA and HD4TIDIDF-OCA) and 60 \sim 90 nm for Rho derivatives (HD4TIDID-Rho and OD4TIDIDF-Rho), with arising featured vibronic structure. When compared electronic absorption behaviors of non-fluorinated

IDID derivatives and fluorinated IDID derivatives, fluorinated IDID derivatives exhibited slightly shorter absorption maximum and band-edge than those of non-fluorinated IDID derivative (ca. 20 nm) in solution states without acceptor dependency; this can be comprehended that the ICT strength of fluorinated IDID derivatives were slightly diminished owing to decreased electron donating nature of fluorinated IDID by incorporation of highly electronegative F atom. Whilst in solid state, this hierarchy was neglected, most probably due to additional attribution of intermolecular interactions.

To investigate F atom effect on electrochemical properties of ICT type IDID derivatives, the HOMO energies of IDID derivatives were evaluated by cyclic voltammetry (CV) in film states. The HOMO energies were extracted from the onset of first oxidation and the LUMO energies were evaluated using optical bandgap. Generally, the LUMO energy level of ICT-type molecules is determined by acceptor building block. However, as was expected from molecular design rational, fluorinated IDID derivatives exhibited stabilized HOMO energies, ca. 0.1 eV, than those of non-fluorinated IDID derivatives (see **Figure 6-2** and **Table 6-1**). Therefore, higher V_{oc} could be expected from fluorinate IDID derivatives than those of non-fluorinated IDID derivatives.

Thermal properties of newly synthesized IDID derivatives were evaluated by differential scanning calorimeter (DSC) measurement. As shown in **Figure 6-3**, thermograms of four IDID derivatives exhibited crystalline behavior. It is noted that, two OCA derivatives exhibited different thermographic behaviors; HD4TIDID-OCA

showed multiple endo- and exothermic peaks during thermal scan, but HD4TIDID-OCA showed only two phase transition peaks, melting and crystallization, at higher temperature region than those of HD4TIDID-OCA. This is most probably due to rotational freedom of σ -bond between IDID core and neighboring thiophenes were restricted by intramolecular C-F \cdots H interaction, resulting in backbone planarization and crystallinity enhancement (In case of Rho derivatives, their thermographic behavior could not be compared directly because two Rho derivatives have different *N*-alkyl side chain each other). Detailed data listed in **Table 6-1**.

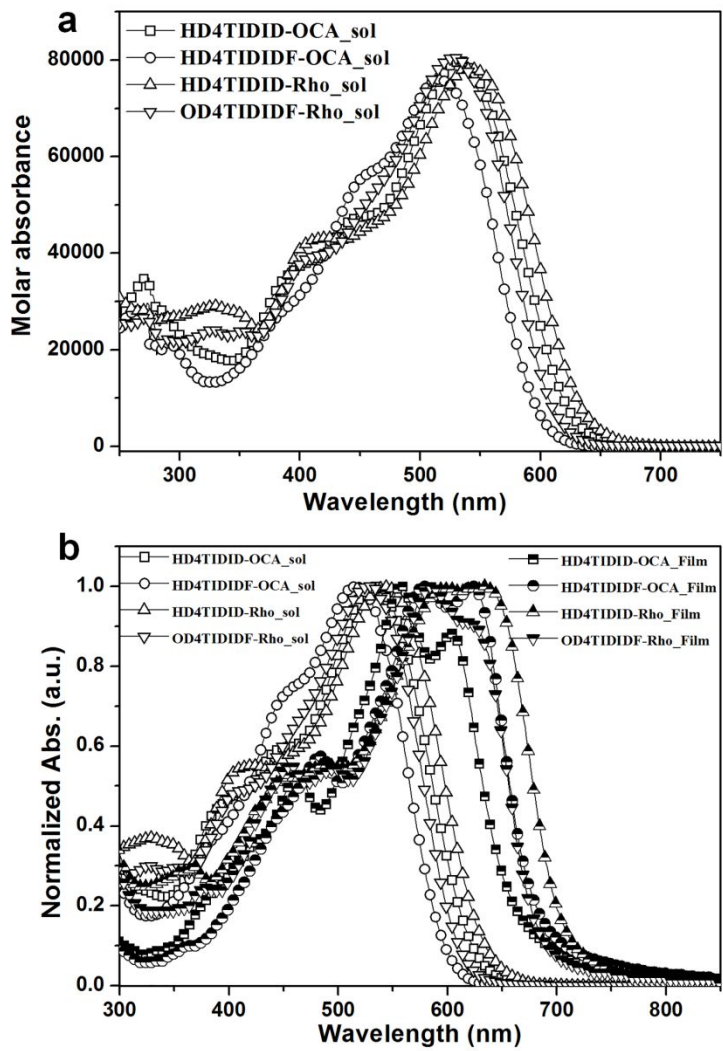


Figure 6-1. (a) UV-vis absorption spectra of IDID derivatives in solution. (b) Normalized absorption spectra of IDID derivatives in solution and film state.

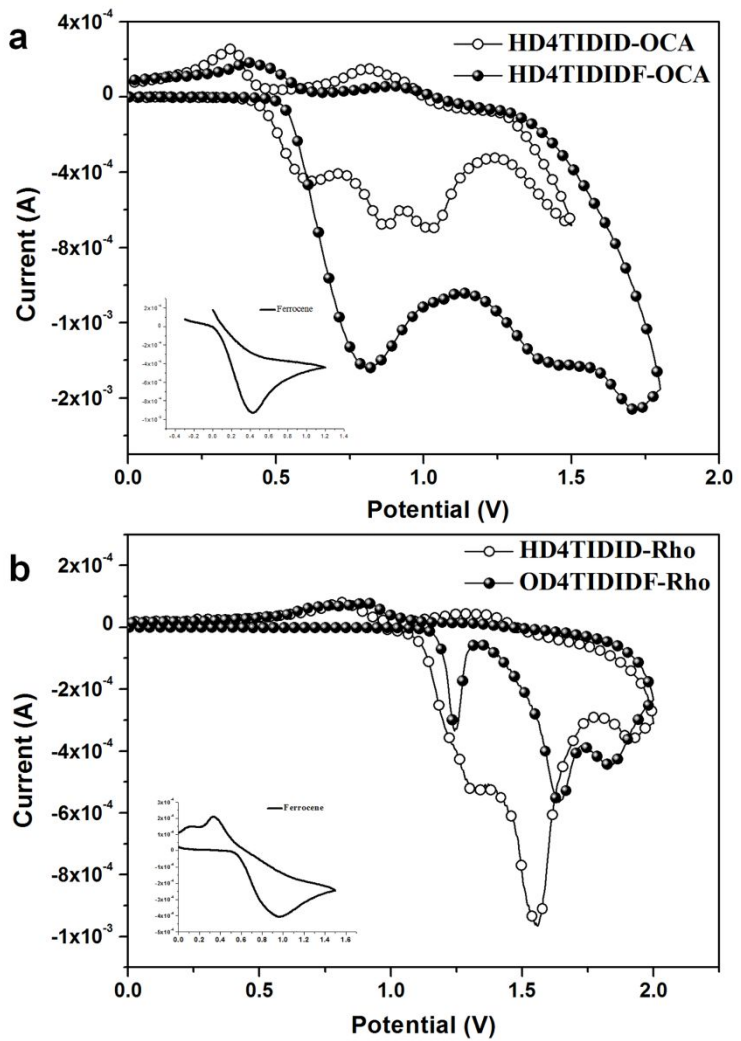


Figure 6-2. Cyclic voltammograms of IDID derivatives in film state: (a) OCA derivatives, and (b) Rho derivatives.

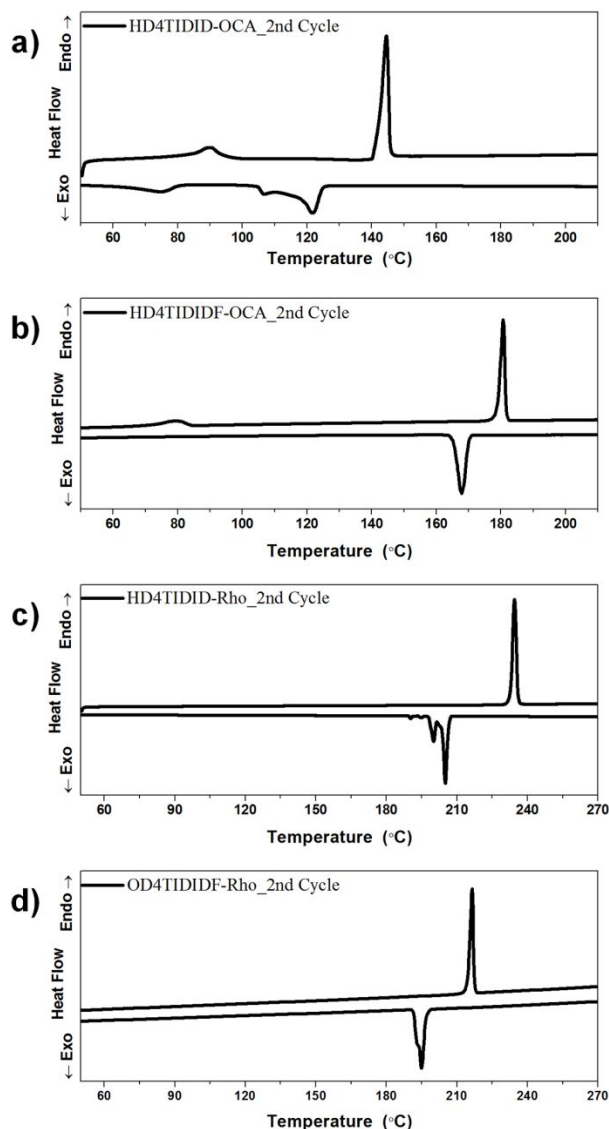


Figure 6-3. Differential scanning calorimetry thermograms of IDID derivatives: (a) HD4TIDID-OCA, (b) HD4TIDIDF-OCA, (c) HD4TIDID-Rho, and (d) HD4TIDIDF-Rho.

Table 6-1. Optical, electrochemical and thermal properties of IDID derivatives.

Compound	Abs. λ_{\max} [sol./film, nm] ^{a)}	$\epsilon.$ [M ⁻¹ cm ⁻¹]	HOMO/ LUMO/band-gap [eV] ^{b)}	Tm/Tc [°C]
HD4TIDID-OCA	534/559	79700	-5.19/-3.31/1.88	90, 144/121, 106,74
HD4TIDIDF-OCA	516/623	76000	-5.29/-3.47/1.82	180/167
HD4TIDID-Rho	544/635	78300	-5.31/-3.55/1.76	234/205,200
HD4TIDIDF-Rho	527/584	80400	-5.4/-3.59/1.81	216/194

^{a)} λ_{\max} is extracted from lowest spin-allowed transition maximum, solution absorption spectra were measured in THF (concentration of 1×10^{-5} M), and film absorption spectra were measured with spin-coated sample (1500 RPM/60s, 0.3 wt% in chloroform); ^{b)} HOMO energy levels were determined by cyclic voltammetry and LUMO energy levels were evaluated using optical bandgap. Film CV samples were prepared on ITO patterned glass by drop-casting, band-gap was measured by onset of absorption band edge.

6.3.3. BHJ-OSC Characteristics

To investigate fluorine substitution effect on photovoltaic performance, solution processed BHJ-OSCs based on four IDID derivatives as p-type material were fabricated with a normal device structure of ITO (indium tin oxide)/PEDOT:PSS (poly(3,4-ethylenedioxythiophene)-poly(styrenesulfonate))/IDID-derivatives:PC₆₁BM /Al, and their performances were optimized by varying blend ratio, concentration, and post thermal treatment. The optimized devices results were listed in **Table 6-2** and their current density-voltage characteristics were illustrated in **Figure 6-4**. The detailed device fabrication procedures were described in section 6-2 **Experimental** section.

For the OCA derivatives, optimized blend ration and thermal treatment temperature were 2:1 (w/w) and 100 °C, respectively. Under optimized condition, HD4TIDID-OCA exhibited the highest PCE of 2.2%, with a V_{oc} of 0.78 V, J_{sc} of 3.89 mA/cm², and FF of 64.9 %. By contrast, HD4TIDIDF-OCA exhibited the highest PCE of 3.07 %, with an increased V_{oc} and J_{sc} of 0.95 V and 4.98 mA/cm², respectively, and same FF of 64.9 %. In case of Rho derivatives, we observed similar results except for J_{sc} ; higher PCE and V_{oc} for OD4TIDID-Rho (3.9% and 0.9 V) than those of HD4TIDID-Rho (3.84% and 0.82 V) with same FF (52%). The incident-photon-to-current efficiency (IPCE) spectrum of the BHJ-OSC devices exhibited broad photocurrent generation between range of 300~700 nm, with efficiency of 20~60% (see **Figure 6-5**), and their calculated

J_{sc} value were well matched for experimental J_{sc} values. It should be noted that, two fluorinated IDID derivatives exhibited higher PCE than those of non-fluorinated counter molecules in BHJOSC devices, mainly attributed to increased V_{oc} . Furthermore, in the same molecular structure except F atom, in case of OCA derivatives, J_{sc} also highly increased, and FF indicating resistances of the OSC devices were not changed. Through these results, I could conclude that F atom substitution into IDID core is the effective molecular design strategy to enhance PCE of BHJOSC based on IDID derivatives by enhancing V_{oc} without rising of other crucial drawbacks.

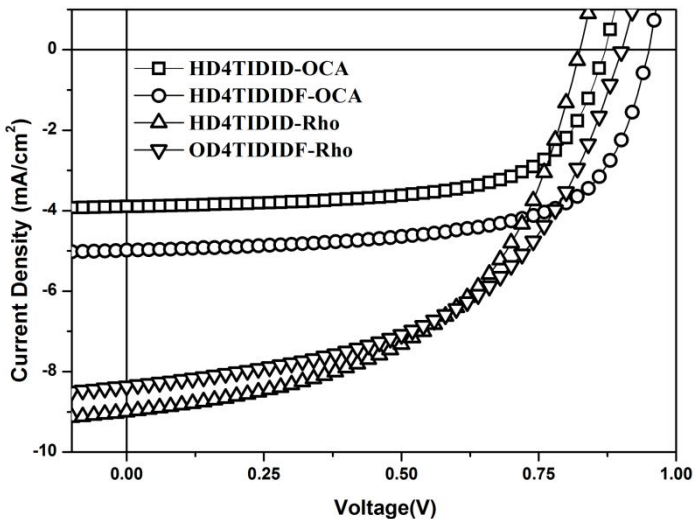


Figure 6-4. Differential scanning calorimetry thermograms of IDID derivatives: (a) HD4TIDID-OCA, (b) HD4TIDIDF-OCA, (c) HD4TIDID-Rho, and (d) HD4TIDIDF-

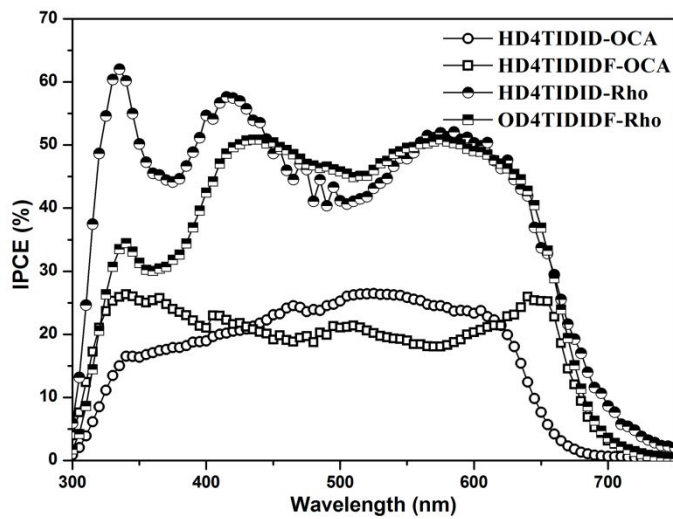


Figure 6-5. IPCE spectra of IDID derivatives:PC₆₁BM BHJ devices

Table 6-2. Optimized BHJOSC device performance of IDID derivatives .

Compound	Blend ratio ^(a)	Annealing (°C)	V_{oc}	J_{sc} (mA cm ⁻²)	J_{sc} measured/Cal. (mA cm ⁻²) ^(b)	FF	PCE (%)
HD4TIDID-OCA	2:1	100°C	0.87(0.84)	3.89(3.81)	3.88/3.87	64.9(53.0)	2.2(1.71)
HD4TIDIDF-OCA	2:1	100°C	0.93(0.93)	4.03(3.85)	4.13/4.07	64.9(62.0)	2.4(2.22)
HD4TIDID-Rho	1:1	110°C	0.82(0.81)	9.00(9.07)	9.00/8.96	52(52)	3.84(3.82)
HD4TIDIDF-Rho	1:1	110°C	0.90(0.91)	8.36(7.76)	8.36/8.52	52(54)	3.90(3.81)

^(a) donor:PC61BM blend ratio; ^(b) Measured current value and calculated current value from IPCE; Parentheses is average value: data obtained from 10 device except HD4TIDID-OCA (4 device)

6.3.4. Film Structure

Two dimensional grazing incidence X-ray diffraction (2D-GIXD) analyses of IDID derivatives and their PC₆₁BM blended films were carried out to investigate fluorine substitution effect on molecular packing motif. To obtain structure-property relationship between molecular structure and OSC characteristics, all of the samples were prepared as same as optimized devices conditions. As shown in **Figure 6-5a**, HD4TIDID-OCA annealed film exhibited distinct Bragg rods (at q_{xy} of 0.110, 0.246, 0.492, 0.754, 1.210, 1.363, 1.520 Å⁻¹) and lamellar diffractions (at q_z of 0.362, 0.722, 1.089 Å⁻¹); this means HD4TIDID-OCA formed 2-dimensionally oriented surface parallel lamellar packing. When HD4TIDID-OCA was blended with PC₆₁BM, diffraction patterns were dimmed and intensities were weakened. Meanwhile, from HD4TIDIDF-OCA annealed film, strong lamellar diffraction peaks were observed until third order (at q_z of 0.331, 0.664, 0.991 Å⁻¹), and π - π diffraction (at q_{xy} of 1.74 Å⁻¹). Moreover, different from HD4TIDID-OCA case, HD4TIDIDF-OCA/PC₆₁BM blended film exhibited strong diffraction peaks at the same position with those of HD4TIDIDF-OCA neat film. Interestingly, from 2D-GIXD results of Rho derivatives, similar tendency was also observed with those of OCA derivatives; i.e., 2D-GIXD diffraction patterns of HD4TIDID-Rho neat film were disappeared when blended with PC₆₁BM, while those of HD4TIDIDF-Rho films were not. Furthermore, it should be noted that,

in both case, OCS and Rho derivatives, fluorination into IDID core gave rise to edge on lamellar packing structure; i.e., π - π distance and lamellar distance of 3.59 Å and 19.03 Å for HD4TIDIDF-OCA, respectively, and 4.00 Å and 19.21 Å for OD4TIDID-Rho, respectively. In short, fluorination induced strong π - π interaction resulting in stable packing structure in PC₆BM blended film.

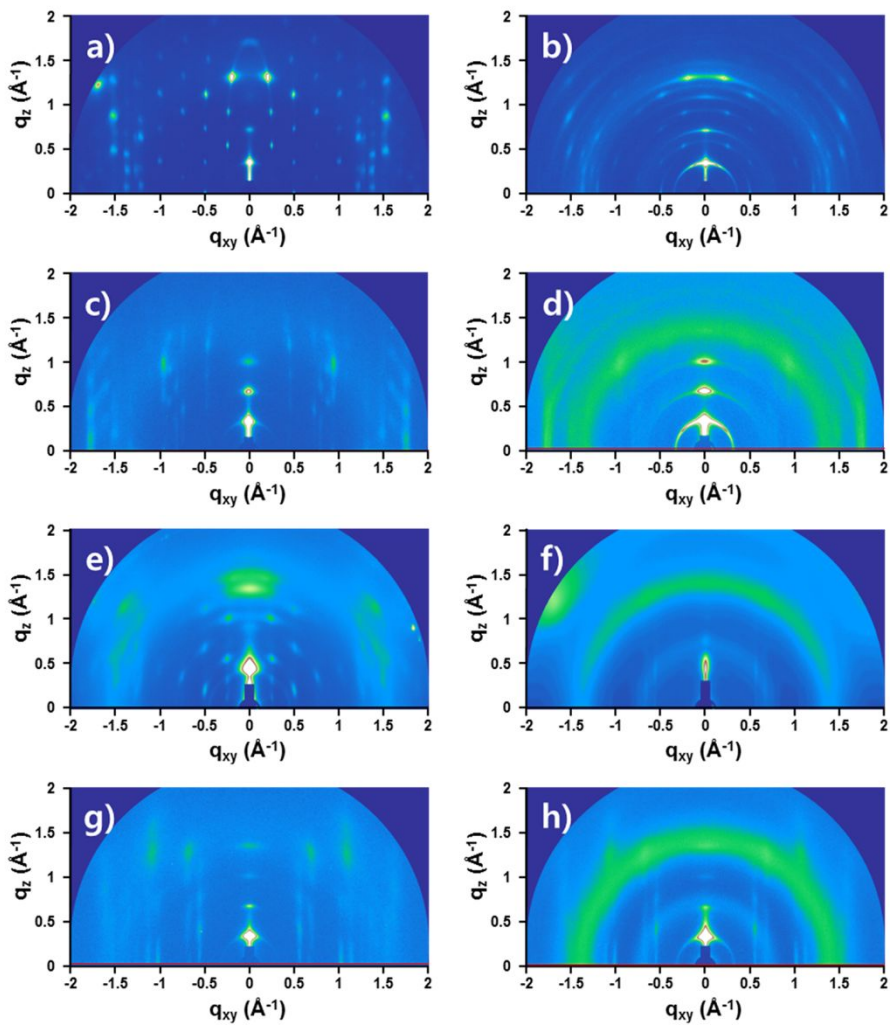


Figure 6-6. 2D-GIXD patterns of IDID-derivatives neat films and IDID-derivatives/PCBM blend films; (a) HD4TIDID-OCA neat, (b) HD4TIDID-OCA/PCBM blend, (c) HD4TIDIDF-OCA neat, (d) HD4TIDIDF-OCA/PCBM blend, (e) HD4TIDID-Rho neat, (f) HD4TIDID-Rho/PCBM blend, (g) OD4TIDIDF-Rho neat, (h) OD4TIDIDF-OCA/PCBM blend.

6.4. Conclusion

I have designed and synthesized a series of IDID-based ICT-type low bandgap small molecules by altering electron donors, IDID and fluorinated IDID, and electron acceptors, OCA and Rho, for the solution processed BHJ-OSCs application. It is noted that, fluorinated IDID derivatives exhibited efficiently stabilized HOMO energies than those of non-fluorinated counter molecules (ca. 0.1 eV, each), resulting in higher V_{oc} (0.08 eV, each). Moreover, strong intermolecular π - π interaction of fluorinated IDID derivatives gave rise to stable micro-structure and edge-on lamellar packing in their PC₆₁BM blended films. Consequently, the BHJ-OSC device using fluorinated IDID derivatives exhibited enhanced device performance than those of non-fluorinated IDID derivatives with a best PCE of 3.90% for OD4TIDIDF-Rho, and 3.07% for HD4TIDIDF-OCA.

6.5. Reference

- [1] S. Gunes, H. Neugebauer, N. S. Sariciftci, *Chem. Rev.* **2007**, *107*, 1324.
- [2] W. Cao, J. Xue, *Energy Environ. Sci.* **2014**, *7*, 2123.
- [3] Y. Huang, E. J. Kramer, A. J. Heeger, G. C. Bazan, *Chem. Rev.* **2014**, *114*, 7006.
- [4] Z. He, B. Xiao, F. Liu, G. Wu, Y. Yang, S. Xiao, C. Wang, T. P. Russell, Y. Cao, *Nature Photonics* **2015**, *9*, 174.
- [5] B. Kan, M. Li, Q. Zhang, F. Liu, X. Wan, Y. Wang, W. Ni, G. Long, X. Yang, H. Feng, Y. Zuo, M. Zhang, F. Huang, Y. Cao, Y. P. Russell, Y. Chen, *J. Am. Chem. Soc.* **2015**, *137*, 3886
- [6] H. J. Song, B. Carsten, I. H. Jung, L. Yu, *Energy Environ. Sci.* **2012**, *5*, 8158
- [7] Y. Liu, J. Zhao, Z. Li, C. Mu, W. Ma, H. Hu, K. Jiang, H. Lin, H. Ade, H. Yan, *Nature Commun.* **2014**, *5*, 5293.
- [8] T. Qin, W. Zajaczkowski, W. Pisula, M. Baumgarten, M. Chen, M. Gao, G. Wilson, C. D. Easton, K. Müllen, S. E. Watkins, *J. Am. Chem. Soc.* **2014**, *136*, 6049.
- [9] T. L. Nguyen, H. Chio, S.-J. Ko, M. A. Uddin, B. Walker, S. Yum, J.-E. Jeong, M. H. Yun, T. J. Shin, S. Hwang, J. Y. Kim, H. Y. Woo, *Energy Environ. Sci.* **2014**, *7*, 3040.
- [10] I. Osaka, T. Kakara, N. Takemura, T. Koganezawa, K. Takimiya, *J. Am. Che.*

Soc. **2011**, *135*, 8834.

- [11] Y. Lin, Y. Li, X. Zhan, *Chem. Soc. Rev.* **2012**, *41*, 4245.
- [12] Y. Chen, X. Wan, G. Long, *Acc. Chem. Res.* [10.1021/ar400088c](https://doi.org/10.1021/ar400088c).
- [13] H. Wang, F. Liu, L. Bu, J. Gao, C. Wang, W. W. T. P. Russell, *Adv. Mater.* **2013**, *25*, 6519.
- [14] A. Tang, C. Zhan, J. Yao, *Chem. Mater.* **2015**, *27*, 4719.
- [15] Y. Lin, J. Wang, Z.-G. Zhang, H. Bai, Y. Li, D. Zhu, X. Zhan, *Adv. Mater.* **2015**, *27*, 1170.
- [16] B. Kan, Q. Zhan, M. Li, X. Wan, W. Ni, G. Long, Y. Wang, X. Yang, H. Feng, Y. Chen, *J. Am. Chem. Soc.* **2014**, *136*, 15529.
- [17] Q. Zhang, B. Kan, F. Liu, G. Long, X. Wan, X. Chen, Y. Zuo, W. Ni, H. Zhang, M. Li, Z. Hu, F. Huang, Y. Cao, Z. Liang, M. Zhang, T. P. Russell, Y. Chen, *Nature Photonics* **2015**, *9*, 35.
- [18] S. R Cowan, C. H. Lee. A. J. Heeger et al. *Chem. Phys. Lett.* **1993**, *213*, 389.
- [19] X. Y. Zhu, *J. Phys. Chem. Lett.* **2014**, *5*, 2283.
- [20] Q. Peng, X. Liu, D. Su, G. Fu, J. Xu, L. Dai, *Adv. Mater.* **2011**, *23*, 4554.
- [21] N. Lim, N. Cho, S. Paek, C. Kim, J. K. Lee. J. Ko, *Chem. Mater.* **2014**, *26*, 2283.
- [22] H.-Y. Chen, J. Hou, A. E. Hayden, H. Yong, K. N. Houk, Y. Yang, *Adv. Mater.* **2010**, *22*, 371.
- [23] W. Li, K. H. Hendriks, A. Furlan, W. S. Christian Roelofs, M. M. Wienk, R. A.

- J. Janssen, *J. Am. Chem. Soc.* **2013**, *135*, 18942.
- [24] K. Narayanaswamy, A. Venkateswararao, V. Gupta, S. Chand, S. P. Singh, *Chem. Commun.* **2016**, *52*, 210.
- [25] Q. V. Hoang, C. E. Song, I.-N. Kang, S.-J. Moon, S. K. Lee, J.-C. Lee, W. S. Shin, *RSC Adv.* **2016**, *6*, 28658.
- [26] H. Wang, F. Liu, L. Bu, J. Gao, C. Wang, W. Wei, T. P. Russell, *Adv. Mater.* **2013**, *25*, 6519.
- [27] J.-L. Wang, F. Xiao, J. Yan, Z. Wu, K.-K. Liu, Z.-F. Chang, R.-B. Zhang, H. Chen, H.-B. Wu, Y. Cao, *Adv. Funct. Mater.* **2016**, DOI: 10.1002/adfm.201505020.
- [28] W. Zhong, J. Xiao, S. Sun, X.-F. Jiang, L. Lan, L. Ying, W. Yang, H.-L. Yip, F. Huang, Y. Cao, *J. Mater. Chem.* **2016**, DOI: 10.1039/c6tc00271d.
- [29] S. C. Price, A. C. Stuart, L. Yang, H. Zhou, W. You, *J. Am. Chem. Soc.* **2011**, *133*, 4625.
- [30] S. Albrecht, S. Janietz, W. Schindler, J. Frisch, J. Kurpiers, J. Kniepert, S. Inal, P. Pingel, K. Fostiropoulos, N. Koch, D. Neher, *J. Am. Chem. Soc.* **2012**, *134*, 14932.
- [31] W. Ni, X. Wan, M. Li, Y. Wang, Y. Chen, *Chem. Commun.* **2015**, *51*, 4936.
- [32] M. Li, W. Ni, H. Feng, X. Wan, Y. Liu, Y. Zuo, B. Kan, Q. Zhang, Y. Chen, *Organic Electronics* **2015**, *24*, 89.
- [33] S. H. Park, A. Roy, S. Beaupré, S. Cho, N. Coates, J. S. Moon, D. Moses, M. Leclerc, K. Lee, A. J. Heeger, *Nature Photonics* **2009**, *3*, 297.
- [34] J. Li, A. C. Grimsdale, *Chem. Soc. Rev.* **2010**, *39*, 2399.

- [35] I. Lim, H. T. Bui, N. K. Shrestha, J. K. Lee, S.-H. Han, *ACS Appl. Mater. Interfaces* **2016**, *8*, 8637.
- [36] X. Lin, Y. Tani, R. Kanda, K.-I. Nakayama, S. Yagai, *J. Mater. Chem. A* **2013**, *1*, 14686.
- [37] M. A. Reddy, C. P. Kumar, A. Ashok, A. Sharma, G. D. Sharma, M. Chandrasekharam, *RSC. Adv.* **2016**, *6*, 9023.
- [38] J.-H. Tsai, C.-C Chueh, M.-H. Lai, C.-F. Wang, W.-C. Chen, B.-T. Ko, C. Ting, *Macromolecules* **2009**, *42*, 1897.
- [39] Y.-Y. Lai, J.-M. Yeh, C.-E. Tsai, Y.-J Cheng, *Eur. J. Org. Chem.* **2013**, 5076.
- [40] Z. R. Owczarczyk, W. A. Braunecker, A. Garcia, R. Larsen, A. M. Nardes, N. Kopidakis, D. W. Ginley, D. C. Olson, *Macromolecules* **2013**, *46*, 1350.
- [41] J. Sim, H. Lee, K. Song, S. Biswas, A. Sharma, G. D. Sharma, J. Ko, *J. Mater. Chem. C* **2016**, *4*, 3508.
- [42] M. L. Tang, J. H. Oh, A. D. Rechardt, Z. Bao, *J. Am. Chem. Soc.* **2009**, *131*, 3733.
- [43] K. Reichembächer, H. I. Süss, J. Hulliger, *Chem. Soc. Rev.* **2005**, *34*, 22.

Abstract in Korean

유기 반도체는 화학적 다기능성, 우수한 물리적 특성, 대면적 저비용 제조, 및 유연성 등의 다양한 장점들로 인하여 일반적으로 사용되고 있는 실리콘기반 반도체의 잠재적 대체재로서 중요한 관심을 이끌었다. 이를 기반으로 현실성 있는 소자성능의 구현을 위하여 폭넓은 파이-공액 분자들이 연구 및 개발되었다. 특히, 이종원소를 포함하는 접합된 복소고리 방향족 화합물(heteroacene)은 자체가 갖는 이종원소에서 비롯되는 독특한 전자적 (electronic) 특성, 확장된 공액구조, 우수한 산화안정성, 및 견고한 분자 쌍임 등의 장점 등에 의해 구조적으로나 전자적으로 매력적인 기반 구조체로서 연구되어왔고, 이로 말미암아 전기적 성능과 이론적 기반의 측면에서 눈부신 발전을 이루었다. 다양한 접합된 복소고리 방향족 화합물 중, 피롤(pyrrole)을 포함하는 화합물들은 낮은 산화환원전위, 강한 전자주게 (electron donating) 특성, 및 분자구조 변형의 용이성 등으로 말미암아 집중적으로 연구되었다. 하지만, 피롤을 포함하는 복소고리 방향족 화합물 중 우수한 소자특성을 보장할 수 있는 구조체는 아직 몇몇의 구조체에 한정적인 상황이다. 다양한 피롤을 포함하는 복소고리 방향족 화합물 중, 본 저자는 안쪽에 두 개의 피롤 링과 바깥쪽에 두 개의 벤젠(benzene) 링이

접합된 구조의 인돌로[3,2-b]인돌 (indolo[3,2-b]indole, 이하 ‘IDID’) 구조체를 고성능 유기반도체 구현을 위한 파이-공액 기반 구조체로서 주목하였다. IDID 구조체는 (*N,N*-), (2,7-), 그리고 (3,8-) 위치에 대칭적으로 구조적 변환을 통한 유도체화가 가능하여 그 유도체의 파이-공액 구조 및 용해도 조절이 매우 용이할 뿐 아니라, 내부의 접합된 두 개의 피롤 링에 의해 매우 강한 전자 주제특성을 갖는다. 이러한 유망한 견지를 가짐에도 불구하고, IDID를 기반으로 하는 유기반도체로의 응용은 아직까지도 미비한 상태이다. 이를 바탕으로, 본 학위논문에서는 다음의 두 가지 주요 주제에 관련하여 서술하였다. ㄱ) IDID를 기반으로 하는 파이-공액 유기분자를 이용한 고효율 유기반도체 구현을 위한 합리적인 분자설계, ㄴ) IDID 구조체의 화학적 구조 개선을 통한 개선된 다기능성의 구조체 개발.

우선적으로, 유기반도체의 기반 구조체로서 IDID 구조체의 우수한 가능성을 확인하고, 더 나아가 그를 기반으로 하는 고성능 및 다양한 공정이 가능한 유기반도체 구현을 위한 분자설계 지침을 제시하고자, *N,N-dihexyl-IDID* 의 2- 그리고 7- 위치에 서로 다른 방향족 및 지방족 기능단이 치환된 IDID 유도체를 설계 및 합성하였다. 그 중 4H4TIDID 라 명명된 유기반도체에서 높은 용해도(> 20 중량 %, chloroform)를 확인하였고, 진공-

증착 (vacuum-deposited) 및 스판-코팅 (spin-coating) 유기 전계-효과 트랜지스터 (organic field-effect transistor) 소자에서 높은 이동도의 p-형 반도체 특성을 (각, $0.97 \text{ cm}^2 \text{ V}^{-1} \text{ s}^{-1}$, $0.18 \text{ cm}^2 \text{ V}^{-1} \text{ s}^{-1}$) 확인하였다. 또한, 앞서 기술한 서로 다른 두 가지 제작방법의 소자의 반도체 층에서 높은 트랜지스터 이동도 구현에 용이한 이차원(2-dimensional)의 분자배열을 동일하게 확인하였다.

IDID 구조체는 피롤을 포함하는 접합된 방향족 화합물들에서 일반적으로 관찰되는 용이한 구조 변형 및 용해도 조절 특성과 같은 장점과 더불어, 타 피롤 기반 접합된 복소고리 화합물 보다 강한 전자주제 특성을 갖는다. 이러한 특성을 기반으로 양극성 (ambipolar) 전하 주입 및 전하 이동을 구현해보고자, 분자 내 전자전이 (intramolecular charge transfer, ICT) 현상을 기반으로 하는 IDID 유도체를, IDID 를 전자주제(D)로 다이사이아노바이닐(dicyanovinyl, DCV)을 전자받게(A)로 하여 A- π -D- π -A 구조로 설계 및 합성하였다. 사이오펜(thiophene)을 파이-연결체(π -spacer)로 사용하는 2TIDID-DCV 유도체들의 경우 적절히 보상된 ICT 효과와 그들의 삼차원의 라멜라 (lamellar) 파이-쌓임 구조에서 발현되는 효과적인 전기적 상호작용에 의해 극적으로 작아진 밴드갭(bandgap)의 형성됨 뿐만 아니라 우수한 형태의 필름이 형성됨 또한 확인하였다. 그 결과, 2H2TIDID-DCV 라

명명된 유기 반도체를 이용한 진공-증착 유기 전계-효과 트랜지스터 소자에서 균형이 잘 맞는 양극성 반도체 특성(p-형 및 n-형 이동도, 각, 0.08 $\text{cm}^2 \text{ V}^{-1} \text{ s}^{-1}$, 0.09 $\text{cm}^2 \text{ V}^{-1} \text{ s}^{-1}$)을 확인 하였다. 또한, 2H2TIDID-DCV의 지방족 기능단(hexyl)을 2-octyldodecyle로 치환한 OD2TIDID-DCV를 이용한 스판-코팅 소자에서도 역시 양극성 반도체 특성(p-형 및 n-형 이동도, 각, $9.96 \times 10^{-2} \text{ cm}^2 \text{ V}^{-1} \text{ s}^{-1}$, $3.34 \times 10^{-2} \text{ cm}^2 \text{ V}^{-1} \text{ s}^{-1}$)을 확인 하였다.

한편, IDID 구조체에 대한 연구를 진행하던 중, 피롤 기반의 접합된 복소고리 화합물에서 일반적으로 관찰되는 어긋난 파이-공액 구조에 기반을 둔 비낀 헤링본 (herringbone) 쌓임 구조가 IDID 유도체에서도 확인 되었다. 이러한 특성은 고성능의 유기반도체 구현을 위해 극복해야 할 요소 임으로, 단점의 극복 및 효과적인 결정 구조 설계 방법을 제시하고자, IDID 구조체 내 플로린 (fluorine, F) 원자를 도입을 통하여 IDID 유도체 분자간 상호작용의 조절을 시도하였다. IDID 구조체의 3- 그리고 8-위치에 F 를 도입할 경우 그것의 유도체 들에 파이-공액 구조의 평면화와 연장, 분자간 파이-쌓임을 야기하는 강한 쿨롱 (Coulombic) 힘, 및 이를 통한 밀도 높은 일차원의 결정성장이 유도됨을 확인 하였다. 그 결과, 4H4TIDID의 IDID 구조체를 F 가 치환된 IDID로 바꾼 4H4TIDIDF를 이용한 단결정 유기 전계-효과 트랜지스터 소자에서 우수한 이동도의 p-형 반도체 특성 ($1.88 \text{ cm}^2 \text{ V}^{-1} \text{ s}^{-1}$

¹⁾ 및 빗겨진 파이-겹침의 분자쌓임 구조를 확인하였다.

또한, 4H4TIDIDF를 페로브스카이트 (perovskite) 태양전지의 결정형 정공 수송 물질 층으로 사용하여 고성능의 특성을 확인하였다. 4H4TIDIDF 의 평평한 파이-공액구조와 유연한 알킬 (alkyl) 그룹이 강한 분자간 파이-상호작용을 야기하여 견고한 분자 쌓임을 가능하게 하고, 이로 말미암아 샌드위치 구조(sandwich-type)의 소자에서 상용의 비정형 정공 수송 물질인 p,p-Spiro-OMeTAD 보다 우수한 정공 이동도를 나타냄을 확인하였다. 뿐만 아니라, 페로브스카이트 층과 정공 수송 물질 층 사이의 계면에서 발생하는 광 발광 (photoluminescence) 소광 (quenching) 현상 또한 페로브스카이트/4H4TIDIDF 계면에서 보다 효과적으로 나타남을 확인하였다. 결과적으로, 4H4TIDIDF 를 정공 수송 물질로 사용한 페로브스카이트 태양전지 소자에서 19% 의 광 에너지 전환 효율 (power conversion efficiency, PCE) 를 보임으로서, 페로브스카이트 태양전지용 정공 수송 물질로서 p,p-Spiro-OMeTAD 보다 우수한 결과를 확인하였다. 이 결과를 통하여 F 가 치환된 IDID 기반의 물질이 새로운 고효율의 페로브스카이트 태양 전지용 정공 수송 물질로의 사용 가능성을 확인할 수 있었다.

마지막으로, F가 치환된 IDID 구조체를 ICT-형 분자의 전자 주계 구조체로 사용하였을 때 나타나는 특성을 확인하고 상술하기 위하여, IDID 및 F 가

치환된 IDID를 전자주계로, 그리고 옥틸 사이아노 아세테이트 (octylcyanoacetate, 이하 ‘OCA’) 및 3-에틸 로다닌 (3-ethylrhodanine, 이하 ‘Rho’)을 전자받계로 하는 ICT-형의 좁은 벤드갭 (bandgap) 단분자를 설계 및 합성하여 용액 공정의 벌크 이종접합(bulk heterojunction)형 유기 태양전지 소자에 적용 하였다. 주목할만한 점으로, F가 치환된 유도체들에서 그렇지 않은 유도체에서 보다 안정화된 최고준위 점유 분자궤도 (highest occupied molecular orbital, HOMO) 에너지 준위(energy level, 각, 약 0.1 전자 볼트 (eV))를 확인하였고, 이로 인하여 벌크 이종접합형 유기태양전지 소자에서 향상된 개로 전압(open circuit voltage 각, 약 0.1볼트 (V))을 보임을 확인하였다. 뿐만 아니라, F가 치환됨으로써 그 유도체들은 강한 분자간 파이-겹침을 보이고, 단독 필름뿐만 아니라 [6,6]-phenyl-C₆₁-butyric acid methyl ester (PC₆₁BM) 혼합 필름에서도 안정한 형태의 엣지-온(edge-on) 기반의 라멜라 분자 쌓임이 형성됨을 확인하였다. 이러한 특성들로 인하여, 벌크 이종접합형 유기태양전지 소자에 적용 시, F가 치환된 IDID 유도체들에서 일반 IDID 유도체들에 비하여 향상된 PCE(OD4TIDIDF-Rho 에서 3.9%, 그리고 HD4TIDIDF-OCA 에서 3.07%)를 확인하였다.

주요어: 인돌로[3,2-b]인돌, 이종원소를 포함하는 복소고리 방향족 화합물, 전하 수송, 정공 수송, 양극성, 유기 전자, 유기 반도체, 유기 전계-효과 트랜지스터, 유기 태양전지, 페로브스카이트 정공 수송 물질.

Student Number: 2008-20687

List of Publications

1. Se Hun Kim, **Illhun Cho**, Mun Ki Sim, Sanghyuk Park, and Soo Young Park, “*Highly Efficient Deep-Blue Emitting Organic Light Emitting Diode Based on the Multifunctional Fluorescent Molecule Comprising Covalently Bonded Carbazole and Anthracene Moieties*”, J. Mater. Chem. **2011**, *21*(25), 9139-9148.
2. **Illhun Cho**, Se Hun Kim, Jong H. Kim, Sanghyuk Park, and Soo Young Park, “*Highly Efficient and Stable Deep-Blue Emitting Anthracene-Derived Molecular Glass for Versatile Types of Non-Doped OLED Applications*”, J. Mater. Chem. **2012**, *22*(1), 123-129.
3. Jangwon Seo, Jong Won Chung, **Illhun Cho** and Soo Young Park, “*Concurrent supramolecular gelation and fluorescence turn-on triggered by coordination of silver ion*”, Soft Matter, **2012**, *8* (29), 7617-7622.
4. Jeong-Wook Mun, **Illhun Cho**, Donggu Lee, Won Sik Yoon, Oh Kyu Kwon, Changhee Lee, Soo Young Park, “*Acetylene-bridged D-A-D Type Small Molecule Comprising Pyrene and Diketopyrrolopyrrole for High Efficiency Organic Solar Cells*”, Organic Electronics, **2013**, *14*(9), 2341–2347.

5. Won Sik Yoon, Sang Kyu Park, **Illhun Cho**, Jeong-A Oh, Jong H. Kim, and Soo Young Park, “*High-Mobility n-Type Organic Transistors Based on a Crystallized Diketopyrrolopyrrole Derivative*”, *Adv. Funct. Mater.* **2013**, *23*(28), 3519-3524.
6. Michael Wykes, Sang Kyu Park, Santanu Bhattacharyya, Shinto Varghese, Ji Eon Kwon, Dong Ryeol Whang, **Illhun Cho**, Reinholt Wannemacher, Larry Lüer, Soo Young Park, Johannes Gierschner, “*Excited State Feature and Dynamics in a Distyrylbenzene Based Mixed Stack Donor-Acceptor Co-Crystal with Luminescent Charge Transfer Characteristics*”, *J. Phys. Chem. Lett.* **2015**, *6*, 3682-3687, (2015)
7. Sang Kyu Park, **Illhun Cho**, Johannes Gierschner, Jinhong Kim, Jong H. Kim, Ji Eon Kwon, Oh Kyu Kwon, Dong Ryeol Whang, Jung-Hwa Park, Byeong-Kwan An, and Soo Young Park, “*Stimuli-Responsive Reversible Fluorescence Switching in the Crystalline Donor-Acceptor Mixture Film: Mixed Stack Charge-Transfer Emission vs. Segregated Stack Monomer Emission*”, *Angew. Chem. Int. Ed.* **2016**, *55*(1), 203-207.
8. **Illhun Cho**, Sang Kyu Park , Boseok Kang , Jong Won Chung , Jin Hong Kim, Kilwon Cho , and Soo Young Park, “*Design, Synthesis, and Versatile Processing of Indolo[3,2-*b*]indole-based π-Conjugated Molecules for High-Performance Organic Field-Effect Transistor*”, *Adv. Funct. Mater.*, DOI: 10.1002/adfm.201505023.

9. Sangyoon Oh, Sang Kyu Park, Jin Hong Kim, **Illhun Cho**, Hyeong-Ju Kim, Soo Young Park, “*Patterned Taping: A High-Efficiency Soft Lithographic Method for Universal Thin Film Patterning*”, ACS Nano, **2016**, *10*, 3478-3485.

List of Presentations

International

1. (Poster) Won Sik Yoon, **Illhun Cho**, and Soo Young Park, “*Synthesis and Emission Color Tuning of Hyghly Luminescent π-Conjugated Hyperbranched Polymer*”, KJF2010 (Korea Japan Joint Forum 2010), Japan, 2010-08-22.
2. (Poster) **Illhun Cho**, Se hun Kim, and Soo Young Park, “*Novel deep-blue emtting molecules for highly efficient non-doped OLED*”, 2015 International Chemical Congress of Pacific Basin Societies (2015 PacificChem), US, 2010-12-15.
3. (Poster) **Illhun Cho**, Sang kyu Park, and Soo Young Park, “*Synthesis and Characterization of Indolo[3,2-b]indole-based p-Type Organic Semiconductor*”, 2012 MRS Spring Meeting & Exhibit, US, 2012-04-09.
4. (Poster) Won Sik Yoon, **Illhun Cho**, and Soo Young Park, “*Synthesis and Characterization of Benzothiadiazole-containing Hyperbranched Polymers for Photovoltaic Application: Comparing the 1,2,4-vs. 1,3,5-Linking Schemes*”, 2012 MRS Spring Meeting & Exhibit, US, 2012-04-09.

5. (Poster) Hae Yeon Chung, **Illhun Cho**, and Soo Young Park, “*Charge transfer complexes of novel electron donating indolo[3,2-b]indoles and various electron accepting molecules*” Korea-France Symposium, Korea, 2013-01-28.
6. (Poster) **Illhun Cho**, Sang Kyu Park, Soo Young Park “*Study of Heteroaromatic Fused-Ring System for Organic Electronics: Synthesis and Characterization of Indolo[3,2-b]indole-based Organic Semiconductors*”, The International Symposium on Carbon Electronics 2013, Korea, 2013-05-06.
7. (Poster) Hae Yeon Chung, **Illhun Cho**, Sang Kyu Park, and Soo Young Park “*Charge transfer complexes of novel electron donating indolo[3,2-b]indole derivatives with various electron accepting molecules and it's organic electronics application*”, 2013 Korea-Japan Symposium on Frontier Photoscience (KJFP 2013), Korea, 2013-11-24.
8. (Poster) Won Sik Yoon, Sang Kyu Park, **Illhun Cho**, and Soo Young Park, “*Energy Level Tailoring of Diketopyrrolopyrrole-based Small Molecules for Organic Field-Effect Transistor and Solar Cell Applications*”, 2013 MRS Fall Meeting & Exhibit, US, 2013-12-01.

9. (Poster) **Illhun Cho**, Oh Kyu Kwon, and Soo Young Park, “*Solution Processable Indolo[3,2-b]indole-based Two Bandgap Small Molecules for High Performance Bulk Heterojunction Organic Solar Cell*”, 2013 MRS Fall Meeting & Exhibit, US, 2013-12-01.

10. (Poster) Sang Kyu Park, **Illhun Cho**, Jin Hong Kim, Oh Kyu Kwon, Ji Eon Kwon, and Soo Young Park “*Highly Luminescent and Ambipolar Transporting Organic Charge-Transfer Cocrystals: Isometric Cocrystals Comprising Distyrylbenzene and Dicyanodistyrylbenzene Derivatives*” 2014 MRS Fall Meeting & Exhibit, US, 2014-04-21.

11. (Poster) SangYoon Oh, Sang Kyu Park, **Illhun Cho**, and Soo Young Park “*Stimuli-Responsive Photoluminescent Properties of Diaryl Substituted Fumaronitrile Derivatives*” KJF-ICOMEPE 2014, Japan, 2014-09-21.

12. (Poster) Hae Yeon Chung, Jung-Hwa Park, **Illhun Cho**, Won Sik Yoon, Dawoon Kim, Sang Kyu Park, and Soo Young Park, “*Solution Processable Indolo[3,2-b]indole and Diketopyrrolopyrrole based A-D-A and D-A-D Triads for Bulk Heterojunction Small Molecule Organic Solar Cells (SMOSCs)*”, 2015 MRS Fall Meeting & Exhibit, US, 2015-11-29

13. (Poster) SangYoon Oh, Sang Kyu Park, Jin Hong Kim, **Illhun Cho**, and Soo Young Park “*Patterned taping: A novel and high-efficiency soft lithographic method for organic thin films*”, 2015 International Chemical Congress of Pacific Basin Societies (2015 PacificChem), US, 2015-12-15.

Domestic

1. (Poster) **Illhun Cho**, Se hun Kim, Soo Young Park, “Highly Efficient and Stable Deep-Blue Emitting Anthracene-Derived Molecular Glass for Versatile Types of Non-Doped OLED Applications” 대한화학회 제 108 회 총회 및 학술발표회, 대한민국, 2011, 2011-09-28.

2. (Poster) Jeong-Wook Mun, **Illhun Cho**, Soo Young Park, “1,3,6,8 - Tetrafunctionalized Pyrenes for Applications in Small Molecule Solution-Processed Bulk-Heterojunction Solar Cells” 대한화학회 제 108 회 총회 및 학술발표회, 대한민국, 2011, 2011-09-28.

List of Patents

1. 김세훈, 이지윤, 김미경, 이관희, 박수영, **조일훈** “유기전기 발광소자 및 그 제조 방법”출원번호 “KR2012-0083509”
2. Se-Hun Kim, Ji-Youn Lee, Mi-Kyung Kim, Kwan-Hee Lee, Soo-Young Park, **Illhun Cho**, “ORGANIC LIGHT EMITTING DEVICE INCLUDING COMPOUNDS”
출원번호 “13/736404”
3. 박수영, **조일훈**, “유기 반도체 물질 및 이를 포함하는 유기 반도체 소자”,
출원번호 “10-2015-0090566”